Universitat Autònoma de Barcelona

Self-assembly of functional chromophores into chiral nanomaterials

Cristina Oliveras González

Tesi doctoral

Doctorat de Ciència dels Materials

Director/a	Co-director/a	Tutor/a
David B. Amabilino	Núria Aliaga Alcalde	Jordi Hernando Campos

Departament de Química

Facultat de Ciències

2015

Chapter 2

Self-assembly of chiral porphyrins and metalloporphyrins through coordination and hydrogen bonds

2. Self-assembly of chiral porphyrins and metalloporphyrins through coordination and hydrogen bonds.

2.1. Introduction.

Porphyrins and their derivatives are present in nature[1] and are essential for the photosynthetic pathway,[2] especially in electron transport and light harvesting processes.[3] This is the case of chlorophyll a[4,5] or the chlorosomes of green-sulfur bacteria which mainly comprises aggregated bacteriochlorophyll (Figure 1).[6,7]

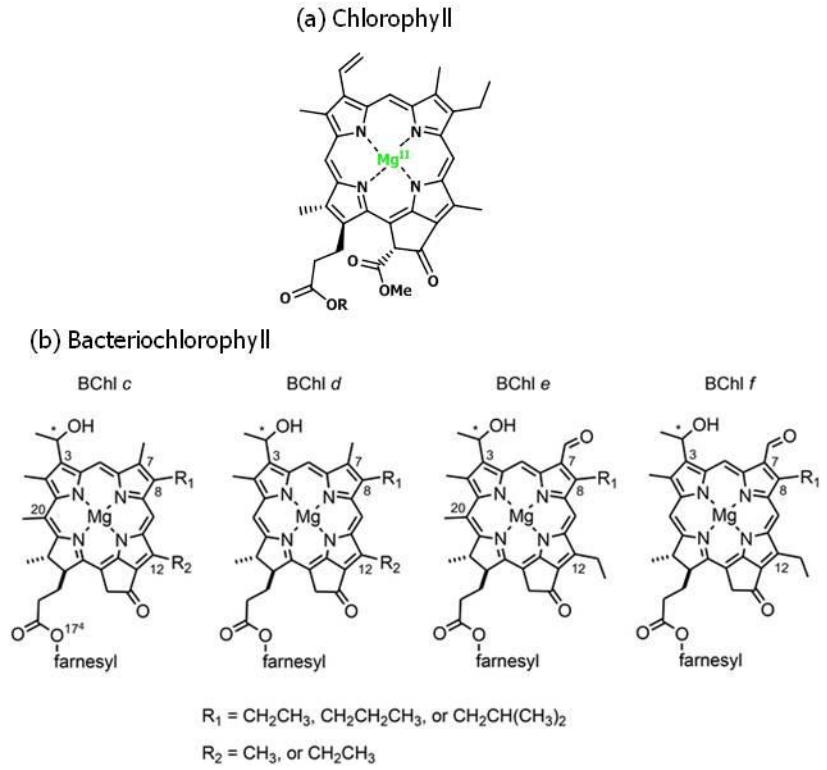

Figure 1. Structure molecule of chlorophyll (a) and strucuture molecules of bacteriochlorophyll (b).

(1) Drain, C. M.; Varotto, A.; Radivojevic, I. *Chem. Rev.* **2009**, *109*, 1630-1658.
(2) Renger, T.; Schlordder, E. *Chem. Phys. Chem.* **2010**, *11*, 1141-1153.
(3) Koepke, J.; Hu, X.; Muenke, C.; Schulten, K.; Michel, H. *Structure* **1996**, *4*, 581-597.
(4) Lo, P.-C.; Leng, X.; Ng, D. K. P. *Coord. Chem. Rev.* **2007**, *251*, 2334-2353.
(5) Hu, J.-S.; Guo, Y.-G.; Liang, H.-P.; Wan, L.-J-; Jiang, L. *J. Am. Chem. Soc.* **2005**, *127*, 17090-17095.
(6) Staehelin, L. A.; Golecki, J. R.; Fuller, R. C.; Drews, G. *Biophys. J.* **1978**, *85*, 3173-3186.
(7) Van Rossum, V.-J.; Steensgaard, D. B.; Mulder, F. M.; Boender, G. J.; Schaffner, K.; Holzwarth, A. R.; de Groot, H. J. M. *Biochemistry* **2001**, *40*, 1587-1595.

These macrocycles have chiral environments arising from self-organization through non-covalent interactions. In all of those systems, a metal ion is coordinated in the core of the chromophore and this feature plays an important role in their self-assembly and function. To understand the role of metal ions and self-organization of porphyrins, enzymes and light-harvesting systems mimicking the natural pigments have been synthesized and studied, confirming the importance of the supramolecular structure on the light harvesting ability.[8,9,10,11,12]

The ability of metalloporphyrins to coordinate with axial ligands containing nitrogen, oxygen or sulfur atoms (the last two, with much weaker binding) gives a great variety of self-assembled superstructures, with facility to tune their optical and electronic properties. This is also the case for many zinc (II) metalloporphyrins in non-polar media, where the coordination with axial ligands through the metal center is weak (due to the d^{10} system formed) but still, they self-assemble in stable supramolecules.[13] The coordination of zinc porphyrins with axial nitrogen derivative ligands, such as imidazolyl or pyridyl groups affords the formation of a well organized macromolecules in the form of cyclic structures,[14,15,16,17] or linear polymers[18,19] and oligomers.[20,21,22] Also the coordination between zinc (II) ions and pyridyl ligands has a relatively large association constant ($\sim 10^3\ M^{-1}$)[23,24] and usually does not disturb the photo-excited state of the porphyrins.[25,26]

(8) Melin, F.; Choua, S.; Bernard, M.; Turek, P.; Weiss, J. *Inorg. Chem.* **2006**, *45*, 10750-10757.
(9) Balaban, T. S.; Linke-Schaetzel, M; Bhise, A. D.; Vanthuyne, N.; Roussel, C.; Anson, C. E.; Buth, G.; Eichöfer, A.; Foster, K.; Garab, G.; Gliemann, H.; Goddard, R.; Javorfi, T.; Powell, A. K.; Rösner, H.; Schimmel, T. *Chem. Eur. J.* **2005**, *11*, 2267-2275.
(10) Balaban, T. S.; Bhise, A. D.; Bringmann, G.; Bürck, J.; Chappaz-Gillot, C.; Eichhöfer, A.; Fenske, D.; Götz, D. C. G.; Knauer, M.; Mizoguchi, T.; Mössinger, D.; Rösner, H.; Roussel, C.; Schraut, M.; Tamiaki, H.; Vanthuyne, N. *J. Am. Chem. Soc.* **2009**, *131*, 14480-14492.
(11) Cantonetti, V.; Monti, D.; Venanzi, M.; Bombelli, C.; Ceccacci, F.; Mancini, G. *Tetrahedron: Asymmetry* **2004**, *15*, 1969-1977.
(12) Haycock, R. A.; Hunter, C. A.; James, D. A.; Michelsen, U.; Sutton, L. R. *Org. Lett.* **2000**, *2*, 2435-2438.
(13) Beltskaya, I.; Tyurin, V. S.; Tsivadze, A. Y.; Guilard, R.; Stern, C. *Chem. Rev.* **2009**, *109*, 1659-1713.
(14) Sguerra, F.; Bulach, V.; Hosseini, M. W. *Dalton Trans.* **2012**, *41*, 14683-14689.
(15) Lipstam, S.; Goldberg, I. *Cryst. Eng. Comm.* **2010**, *12*, 52-54.
(16) Chi, X.; Guerin, A. J.; Haycock, R. A.; Hunter, C. A.; Sarson, L. D. *J. Chem. Soc. Chem. Commun.* **1995**, *24*, 2567-2569.
(17) Maeda, C.; Kamada, T.; Aratani, N.; Osuka, A. *Coord. Chem. Rev.* **2007**, *251*, 2743-2752.
(18) Fleischer, E. B.; Shachter, A. M. *Inorg. Chem.* **1991**, *30*, 3763-3769.
(19) Wojaczynski, J.; Latos-Grazynski, L. *Coord. Chem. Rev.* **2000**, *204*, 113-171.
(20) Wilson, G. S.; Anderson, H. L. *Chem. Commun.* **1999**, 1539–1540.
(21) Anderson, H. L. *Chem. Commun.* **1999**, 2323-2330.
(22) Imamura, T.; Fukushima, K. *Coord. Chem. Rev.* **2000**, *198*, 133-156.
(23) Morisue, M.; Morita, T.; Kuroda, Y. *Org. Biomol. Chem.* **2010**, *8*, 3457-3463.
(24) Ercolani, G.; Ioele, M.; Monti, D. *New J. Chem.* **2001**, *25*, 783-789.
(25) Hwang, I.-W.; Kamada, T.; Ahn, T. K.; Ko, D. M.; Nakamura, T.; Tsuda, A.; Osuka, A.; Kim, D. *J. Am. Chem. Soc.* **2004**, *126*, 16187-16198.
(26) Bernad Jr, P. L.; Guerin, A. J.; Haycock, R. A.; Heath, S. L.; Hunter, C. A.; Raposo, C.; Rotger, C.; Sarson, L. D.; Sutton, L. M. *New J. Chem.* **2008**, *32*, 525-532.

Zinc (II) porphyrins tend to form pentacoordinated aggregates with square pyramidal geometries, but the hexacoordination of this class of metalloporphyrins or the presence of extra-coordinating sites for infinite architecture constructions has also been reported.[27,28,29] The control of the fifth coordination site of metalloporphyrins with nitrogen ligands is an important parameter in order to study the kinetic and thermodynamic effects in the self-assembly process of these compounds.[30,31]

2.2. Objectives

The objective of this project is:

The preparation of molecular materials with potential applications in light harvesting via hierarchical self-assembly.

To achieve this main goal, compounds Zn-(*R,R,R*)-**1**, Zn-(*R,R*)-**2**, Zn-(*R,R*)-**3** and Zn-(*R*)-**4** have been designed and synthesized to probe hierarchical assembly using different non-covalent interactions at each stage (Figure 2).

Each compound differs from the other in the number and position of the stereogenic centers and therefore, the associated hydrogen bond-forming units and pyridyl groups. Alkyl chains where introducted in the systems to improve solubility of the final species, adhesion toward each other as well as to non-polar surfaces through van der Waals interactions.[32] The role of the pyridyl groups is allowing self-assembly through coordination with the zinc (II) ion in the core of porphyrinic rings.

(27) Deiters, E.; Bulach, V.; Hosseini, M. W. *Chem. Commun.* **2005**, 3906-3908.
(28) Deiters, E.; Bulach, V.; Hosseini, M. W. *New J. Chem.* **2006**, *30*, 1289-1294.
(29) El Garah, M.; Ciesielski, A.; Marets, N.; Bulach, V.; Hosseini, M. W.; Samori, P. *Chem. Commun.* **2014**, *50*, 12250-12253.
(30) Brandel, J.; Trabolsi, A.; Melin, F.; Elhabiri, M.; Weiss, J.; Albrecht-Gary, A-M. *Inorg. Chem.* **2007**, *46*, 9534-9536.
(31) Brandel, J.; Trabolsi, A.; Trabolsi, H.; Melin, F.; Koepf, M.; Wytko, J. A.; Elhabiri, M.; Weiss, J.; Albrecht-Gary, A-M. *Inorg. Chem.* **2009**, *48*, 3743-3754.
(32) Linares, M.; Iavicoli, P.; Psychogyiopoulou, K.; Beljonne, D.; De Feyter, S.; Amabilino, D. B.; Lazzaroni, R. *Langmuir* **2008**, *24*, 9566-9574.

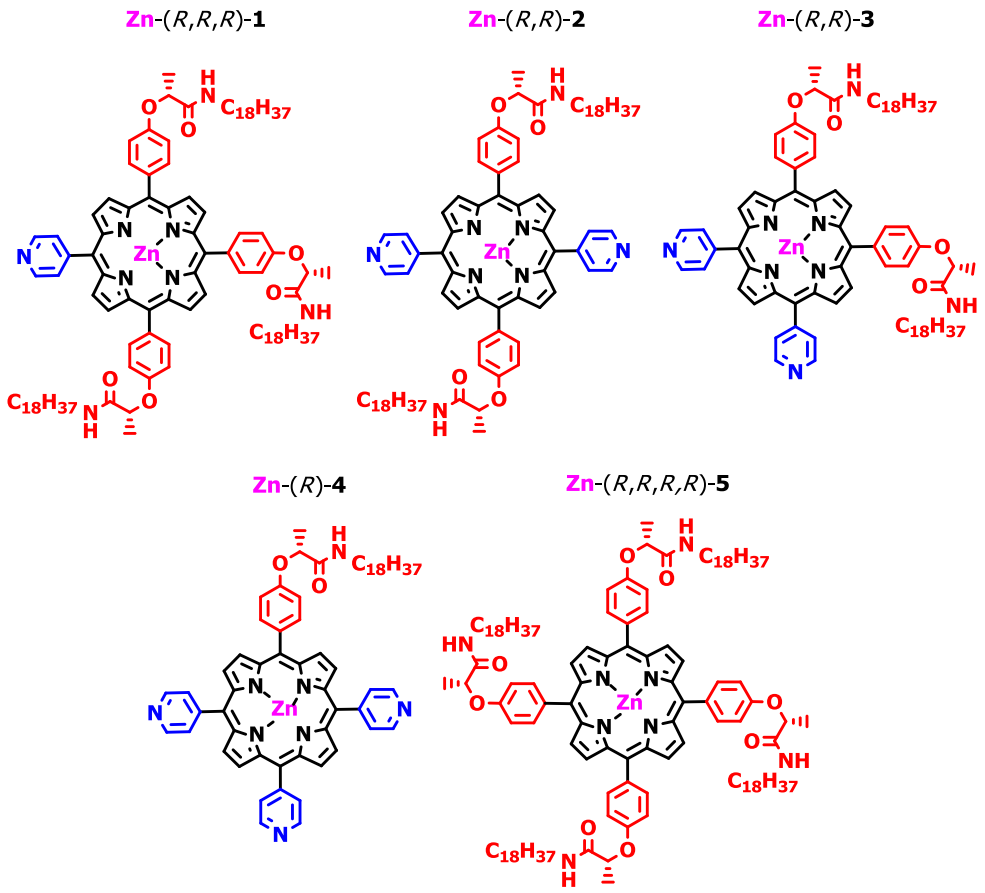

Figure 2. Target functionalized metalloporphyrins.

In principle, for these compounds, two different coordinating atoms can bind the metal ion: the pyridyl nitrogen atom or the carbonyl oxygen atom. Furthermore hydrogen-bonding between amide groups can be the main non-covalent interactions to form aggregates. However, more than one interaction can be participating in the self-assembly of these chromophores. Figure 3 shows the stronger potential interactions that need to be considered.

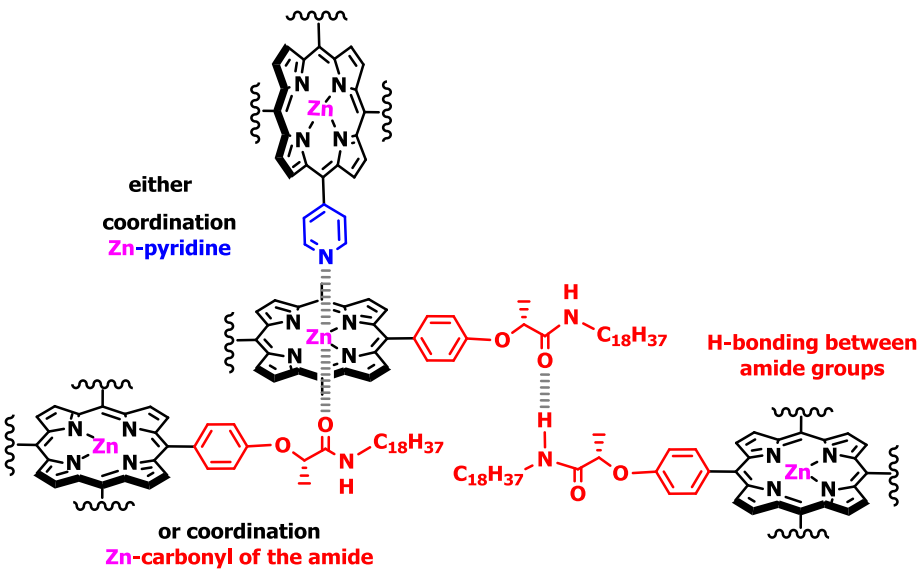

Figure 3. Non-covalent interactions that can in principle drive the self-assembly of the porphyrins presented here.

The influence of the proportion and position of the 4-pyridyl and 4-phenyl rings bearing the stereogenic centers (in the lactamide moieties) on the aggregation of the molecules in solution, and upon precipitation, will be studied. In solution, absorption spectroscopy and circular dichroism spectroscopy (CD), a chiroptical tool that allows precise monitoring of aggregation, will be used to obtain information about the complex architecture and relative orientations of molecules in aggregates.[33,34,35] The morphology of the aggregates will be investigated by atomic force microscopy (AFM) after being transferred from solution to surface and by scanning electron microscopy (SEM) to analyze their morphology in the solid state when precipitate far from the equilibrium conditions.

2.3. Synthesis of chiral porphyrins bearing coordinating ligands.

Porphyrins and metalloporphyrins studied in this work that contained in their *meso* position chiral amide groups and pyridyl groups were synthetized following a short synthetic route (Scheme 1).

(33) Nieto-Ortega, B.; Ramírez, F. J.; Amabilino, D. B.; Linares, M.; Beljonne, D.; López Navarrete, J. T.; Casado, J. *Chem. Commun.* **2012**, *48*, 9147-9149.
(34) Huang, X.; Nakanishi, K.; Berova, N. *Chirality* **2000**, *12*, 237-255.
(35) Smulders, M. M. J.; Buffeteau, T.; Cavagnat, D.; Wolffs, M.; Schenning, A. P. H. J.; Meijer, E. W. *Chirality* **2008**, *20*, 1016-1022.

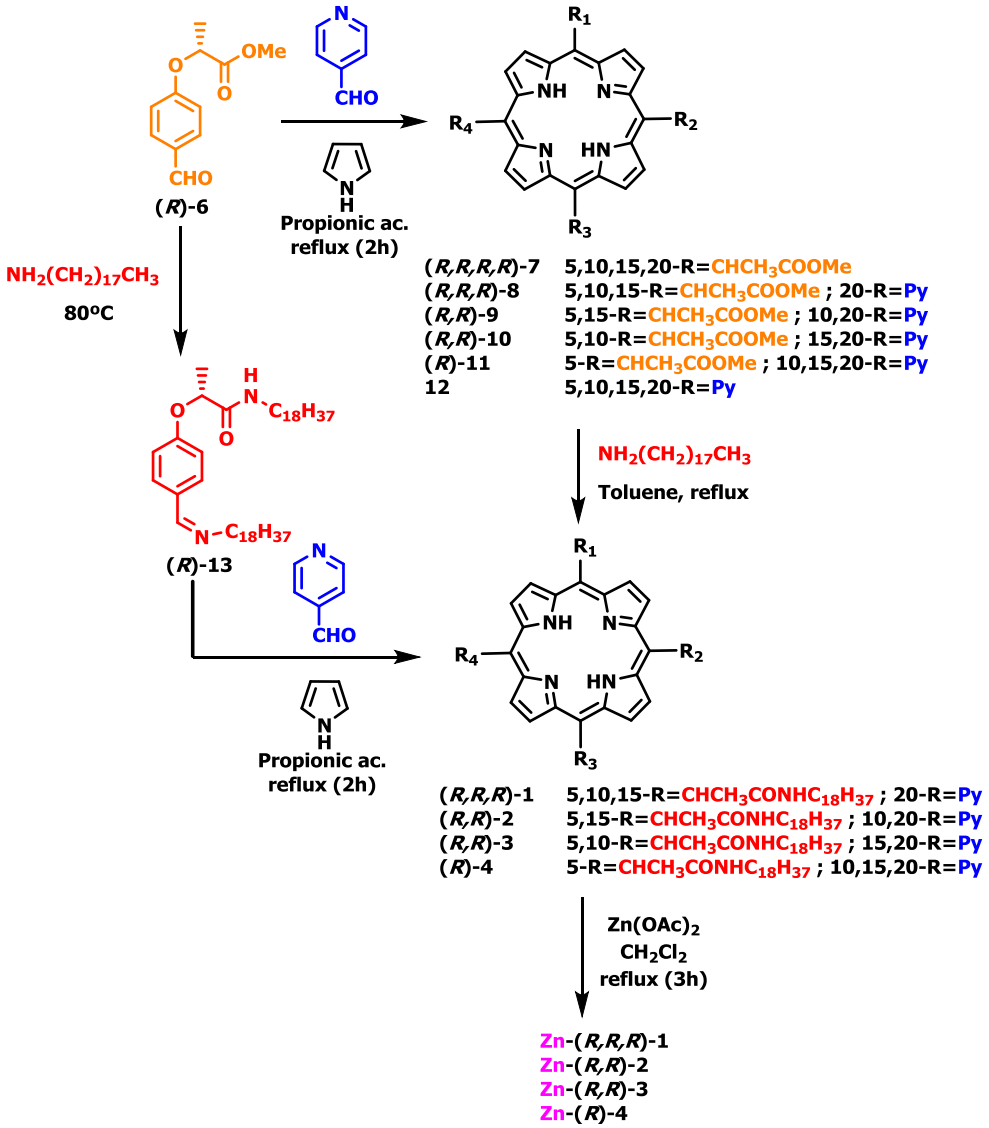

Scheme 1. Synthesis of metalloporphyrin Zn-(*R,R,R*)-**1**, Zn-(*R,R*)-**2**, Zn-(*R,R*)-**3**, Zn-(*R*)-**4**.

2.3.1. Synthesis of the chiral aldehyde (*R*)-6 by Mitsunobu reaction.

The first step before the synthesis of the microcycle is the preparation of the chiral aldehyde derivative, that by a Mitsunobu reaction was prepared (Scheme 2).[36]

(36) Minguet, M.; Amabilino, D. B.; Vidal-Gancedo, J.; Wurst, K.; Veciana, J. *J. Mater. Chem.* **2002**, *12*, 570-578.

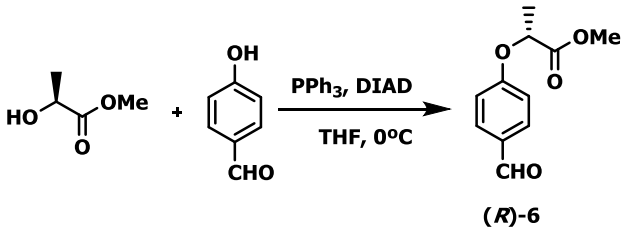

Scheme 2. Synthesis of lactate aldehyde (*R*)-**6** by Mitsunobu reaction.

The lactate benzaldehyde (*R*)-**6** was achived by the reaction between the commercially available compounds 4-hydroxy-benzaldehyde and (*S*)-(-)-Methyl lactate in dry conditions, using triphenylphosphine and diisopropyl-azodicarboxylate as reagents.

It has to notice that in this process, an inversion of stereochemistry of the methyl lactate take place and this is thanks to the difference in acidity of both alcohols, being pka ~13 for methyl lactate and pka ~7 for hydroxybenzaldehyde. During the reaction two different intermediates can be formed, and the ratio between them depends on the acidity of the two alcohol groups and the polarity of the solvent (Scheme 3).[37]

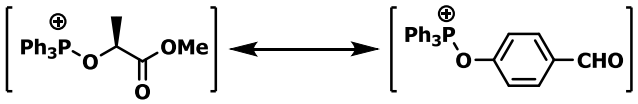

Scheme 3. Equilibrium between oxyphosphonium salts.

The equilibrium was favored by the formation of the lactate oxyphosphonium derivative due to the low acidity of this group, and consequently the nucleophilic attack of the hydroxybenzaldehyde makes possible the inversion of the stereochemistry of the lactate group as it can appreciated in Scheme 4.

(37) Camp, D.; Jenkins, I. D. *J. Org. Chem.* **1989**, *54*, 3045-3049.

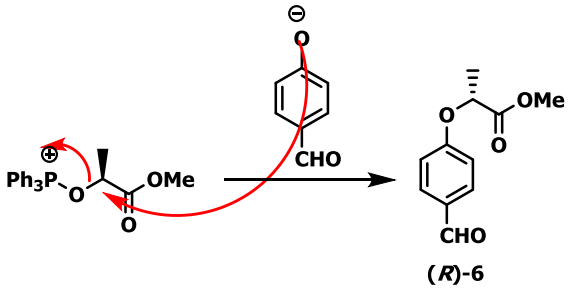

Scheme 4. Mechanism of inversion of stereochemistry of methyl lactate group.

In order to determine the chirality of the lactate aldehyde derivative, optical rotation analyses were performed and compared with the data previously described in our group. A solution 0.19 M in CH_2Cl_2 was analyzed obtaining an optical rotation of $[\alpha]_{546observed}$ = +43 deg·cm^2/mg. This value was in agreement with values found in literature ($[\alpha]_{546literature}$ = +46 deg·cm^2/mg), indicating that the inversion of stereochemistry during the Mitsunobu reaction took place.

2.3.2. Formation of the porphyrin ring.

The synthesis of *meso*-subsituted porphyrins can be performed by following two different methods of preparation as it was explained in the general introduction.[38]

The reaction between two different aldehydes provides a combinatorial chemistry affording a mixture of six different porphyrins that required chromatography by the isolation of each of the porphyrins form in the reaction.

The purpose of this work is the synthesis of a family of porphyrins that contain in their structure the chiral group resulting from the lactate benzaldehyde derivative (*R*)-**6**, and a pyridyl group (Scheme 5).

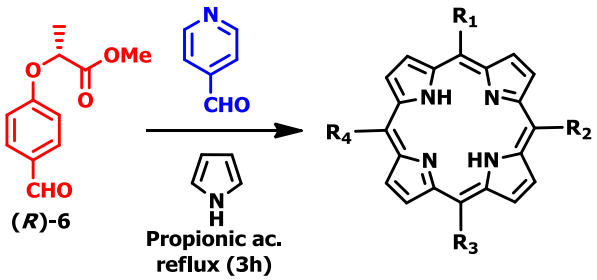

Scheme 5. Synthesis of the free-base porphyrins **7**-**12**.

(38) The different methods for the synthesis of porphyrins are explained in detail in the general introduction, ***Chapter 1***.

The condensation of these two aldehydes with pyrrole in a 1:1:1 ratio in refluxing propionic acid and in air conditions afforded 6 different porphyrins with variations in their constitutions. After removed propionic acid from the crude mixture and several silica gel chromatographies, each porphyrin was obtained as a pure purple solid, having an overall yield of 10% due to the formation of polipyrrolic byproducts during the reaction process.

In order to enhance the yield of the reaction using Adler and Longo method, the two-step reaction was carry-out in dichloromethane at room temperature (Scheme 6).

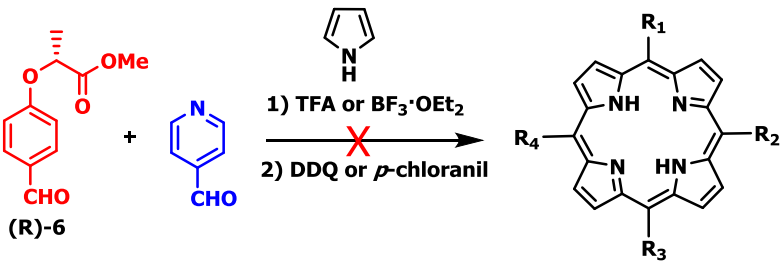

Scheme 6. Synthesis of free-base porphyrins **7**-**12**.

However, the Lindsey method did not afforded the desired porphyrins in better yields. Different tests using TFA or $BF_3{\cdot}OEt_2$, as well DDQ or p-chloranil as oxidative agents were performed but the final yields were always, comparable with the one obtained by the initial one pot reaction; the formation of a number of byproducts during the reaction process coming from the oxidative reagents, which were difficult to remove by chromatography, may be the responsible for the low yield.

Bearing these results in mind, the porphyrin ring was synthetized following the Adler and Longo method obtaining after distillation of propionic acid under vacuum and several chromatographic steps in CH_2Cl_2/1.5% MeOH (*R,R,R*)-**8** (1.4%), (*R,R*)-**9** (0.5%), (*R,R*)-**10** (1.5%), (*R*)-**11** (2.7%) and **12** (2.0%).

Porphyrin (*R,R,R,R*)-**7** was not isolated after purification.

2.3.2.1. Porphyrin identification by ^{1}H-NMR analysis.

From the order of elution in the silica gel chromatography one can identify each porphyrin, supported by ^{1}H-NMR analysis in *d*-chloroform (Figure 4).

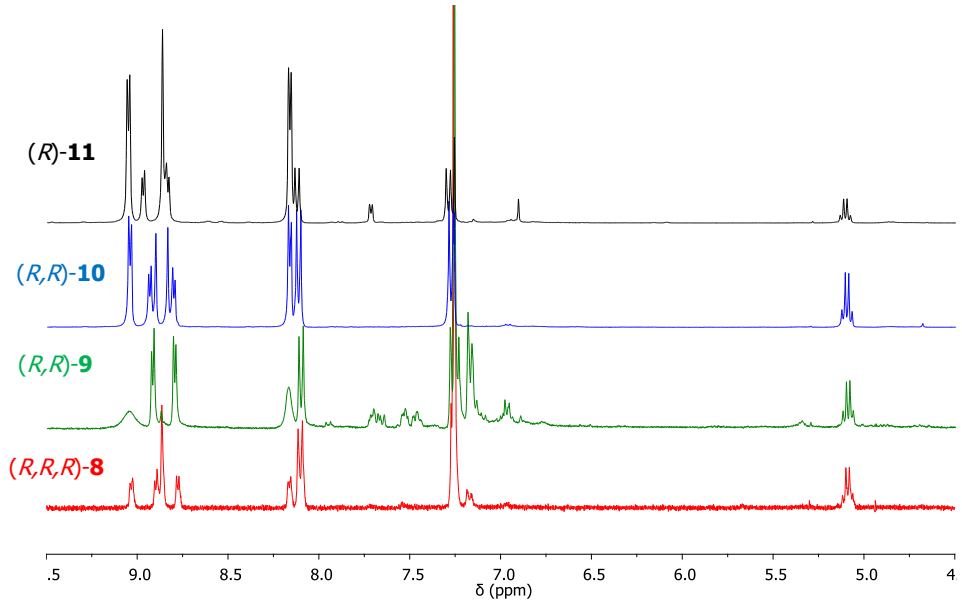

Figure 4. ^{1}H-NMR spectra of free-base porphyrins (*R,R,R*)-**8**, (*R,R*)-**9**, (*R,R*)-**10** and (*R*)-**11** in *d*-chloroform.

The intensity of the chiral proton at 5.10 ppm vary with the number of the lactate group in the porphyrin ring, helping to the good identification of the porphyrin, even though was challenging to distinguish between the two constitutional isomers (*R,R*)-**9** and (*R,R*)-**10**.

The multiplicity of hydrogen atoms of the pyrrole group were the key to identify correctly the both isomers (*R,R*)-**9** and (*R,R*)-**10**. While in the case of 5,15-porphyrin derivative (*R,R*)-**9** a double doublet resonance (AB system) was observed, on the other hand the ^{1}H-NMR of the other isomer (5,10) showed the same AB system with two singlets in the inner part of the doublets (Figure 5).

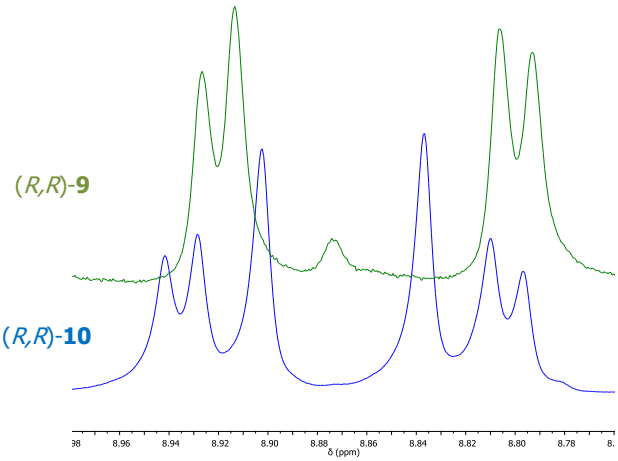

Figure 5. Pyrrole protons of (*R,R*)-**9** and (*R,R*)-**10** in ^{1}H-NMR in *d*-chloroform.

The different multiplicity observed is due to the different symmetry of the molecule. In one hand C_{2v} symmetry group for porphyrin (*R,R*)-**9** present two symmetry planes in the x' and y' axes fact that two distinct signals are observed for pyrrole protons whereas (*R,R*)-**10** with only one plane of symmetry in the y axes belongs to the C_{1h} symmetry group. Due to this symmetry, the molecule present four different pyrrole protons in the porphyrin ring (Figure 6).

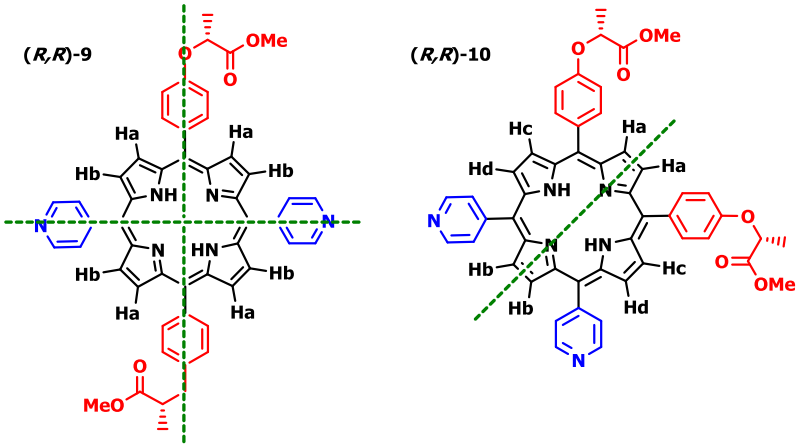

Figure 6. Symmetry of porphyrins (*R,R*)-**9** and (*R,R*)-**10**.

2.3.3. Synthesis of the desired free-base porphyrins.

2.3.3.1. Amidation of the ester groups.

The following step before to achieve the desired metalloporphyrins was the amidation of the ester group next to the stereogenic center. The reaction was previously described using

octadecylamine as a solvent due to the low melting point (~50ºC).[39] When the reactions were carried out in these conditions, it was possible to observe that the solubility of porphyrins decrease with the number of pyridyl groups in the structure fact that there was not a homogenous mixture between porphyrin and the excess of melting octadecylamine. In order to solve the solubility problem, porphyrins were dissolved in small amounts of non protic solvent, in this case toluene, and octadecylamine was added in excess to ensure the complete amidation of the ester groups (Scheme 7).

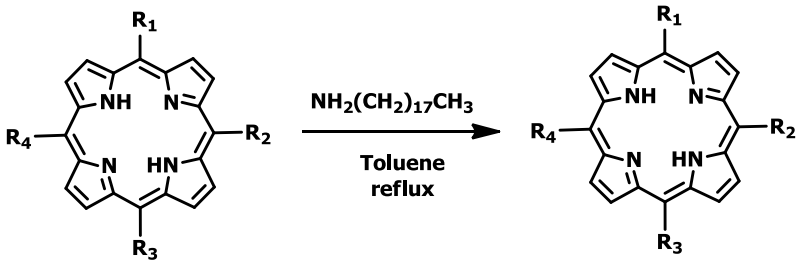

Scheme 7. Synthesis of free-base porphyrins (*R*,*R*,*R*)-**1**, (*R*,*R*)-**2**, (*R*,*R*)-**3** and (*R*)-**4**.

The crude compound of each porphyrin was subjected to a column chromatography and exclusion size chromatography for the complete removal of octadecylamine obtaining free-base porphyrins in 60-70% yield.

2.3.3.2. Amidation of the lactate aldehyde (*R*)-6.

Another synthetic route was proposed and tried in order to increase and optimized the yield of free-base porphyrins (*R*,*R*,*R*)-**1**, (*R*,*R*)-**2**, (*R*,*R*)-**3** and (*R*)-**4**. Furthermore, the new route reduce the time scale in the over synthesis due to the ester group adjacent to the chiral group was amidated before to prepare the porphyrin ring, reducing the number of amidation reaction in the whole process.

(*R*)-Methyl 2-(4-formylphenoxy)propanoate ((*R*)-**6**) was mixed with octadecylamine at 80ºC using the latter as solvent. This procedure afforded the chiral compound (*R*)-**13** in a quite good yield (66.2%) after dissolving in CH_2CH_2/CH_3CN and filtration (Scheme 8).

(39) Iavicoli, P.; Xu, H.; Feldborg, L. N.; Linares, M.; Paradinas, M.; Stafström, S.; Ocal, C.; Nieto-Ortega, B.; Casado, J.; López Navarrete, J. T.; Lazzaroni, R.; De Feyter, S.; Amabilino, D. B. *J. Am. Chem. Soc.* **2010**, *132*, 9350-9362.

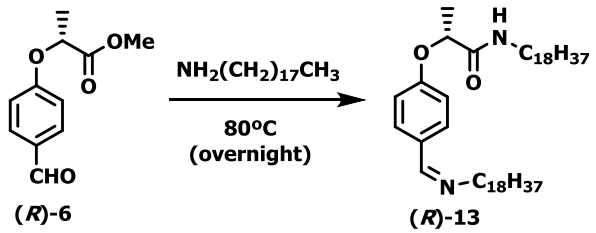

Scheme 8. Synthesis of imine (*R*)-**13**.

Scheme 9 shows the mechanism of the formation of the imine chiral amide (*R*)-**13** that at the same time was not surprising their formation because the starting compound had two reactive carbonyl groups, and the formation of the imine was favoured due the conjugation of the double bond with the aromatic ring.[40]

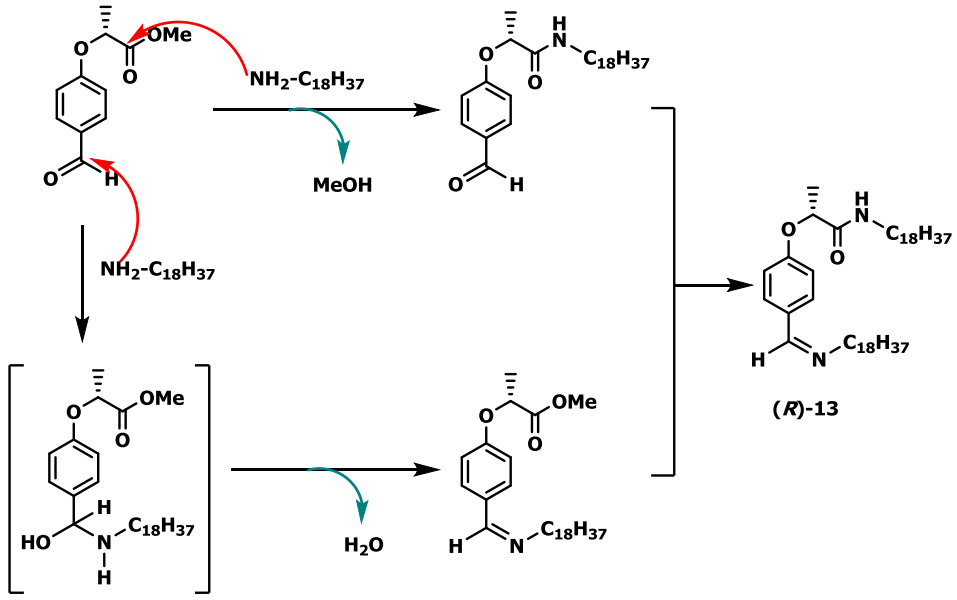

Scheme 9. Mechanism of (*R*)-**13** formation.

2.3.3.2.1. Analysis of compound (*R*)-13 by ^{1}H-NMR.

When compound (*R*)-**13** was characterize by ^{1}H-NMR we observed that amine group not only attacked the ester group to form the desired amide but also the aldehyde group was attacked by the octadecylamine affording the imine specie (Figure 7).

(40) Radulović, N. S.; Miltojević, A. B.; Vukićević, R. D. *C. R. Chimie* **2013**, *16*, 257-270.

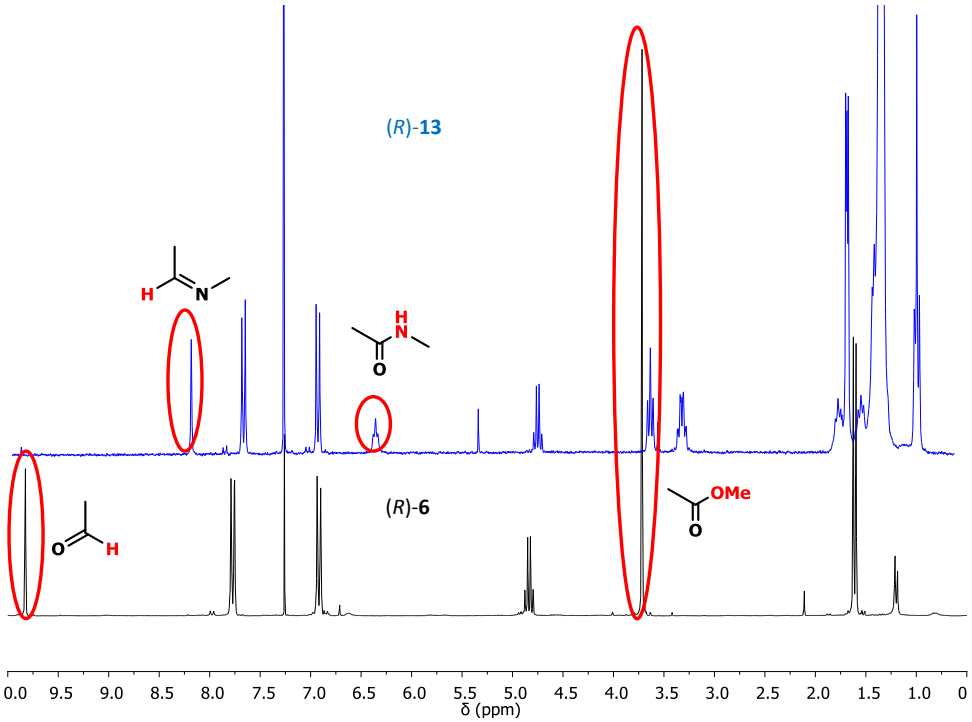

Figure 7. ^{1}H-NMR in *d*-chloroform of compounds (*R*)-**6** and (*R*)-**13**.

As it could observe in the ^{1}H-NMR spectrum, the imine proton appears at around 8.25 ppm that clearly shift to high field compare with the aldehyde proton that appears around 9.75 ppm, apart from that the amidation took place as the triplet at 6.33 ppm corresponding to the amide proton suggested. Moreover, other peaks can corroborate the formation of the amide and imine groups. First of all, the disappearance of the singlet at around 3.70 ppm corresponding to the protons of methoxy group is a clear indicative of the formation of the amide group. Furthermore two different signals corresponding to -CH_2 next to these groups in the region 3.00 to 4.00 ppm in the spectrum of (*R*)-**13** suggest the formation both the amide and the imine. At 3.56 ppm a triplet signal was observed by the -CH_2 next to the imine group, while at 3.25 a double-triplet for the -CH_2 directly link to the amide group was noted. The multiplicity of this -CH_2 of the amide was explained by the proximity of the chiral group, fact that the two protons were not equivalent to each other.

2.3.3.3. Synthesis of the desired free-base porphyrins from (*R*)-13.

The synthesis of the porphyrin rings was achieved following the same procedure as before, dissolving (*R*)-**13** and pyridine-4-aldehyde in propionic acid in air conditions. Freshly pyrrole was added to the reaction mixture, and after 3 hours of reaction under reflux at 150ºC crude

compounds were obtained. Free-base porphyrins (*R*,*R*,*R*)-**1**, (*R*,*R*)-**2**, (*R*,*R*)-**3** and (*R*)-**4** were obtained after be purified by elution and exclusion chromatography in around 1% yield for each one (Scheme 10).

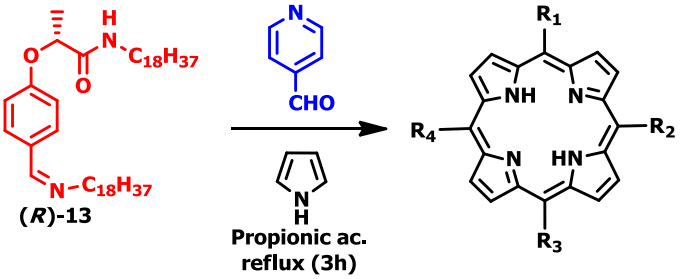

Scheme 10. Synthesis of free-base porphyrins (*R*,*R*,*R*)-**1**, (*R*,*R*)-**2**, (*R*,*R*)-**3** and (*R*)-**4**.

The low yield obtained for each porphyrin, even being a bit smaller compare with the other route suggest that there is no significant difference in reactivity of the imine group compare with the aldehyde in the condensation with pyrrole, perhaps due to in acidic conditions imine is hydrolyse back to the aldehyde and primary amine.

2.3.3.4. Analysis of the desired free-base porphyrins by ^{1}H-NMR.

The ^{1}H-NMR spectra was registered for each porphyrin in *d*-chloroform (~30mM) and as it was happen with porphyrins (*R*,*R*,*R*)-**8**, (*R*,*R*)-**9**, (*R*,*R*)-**10** and (*R*)-**11**, each porphyrin was distinguish to the others by the change in intensity of the proton at the stereogenic center at around 5.00 ppm as well as by the multiplicity of the pyrrole protons located at around 8.75 ppm. Furthermore, the intensity of the peak related to the amide group at 6.60 ppm change with the substitution of the porphyrinic ring (Figure 8).

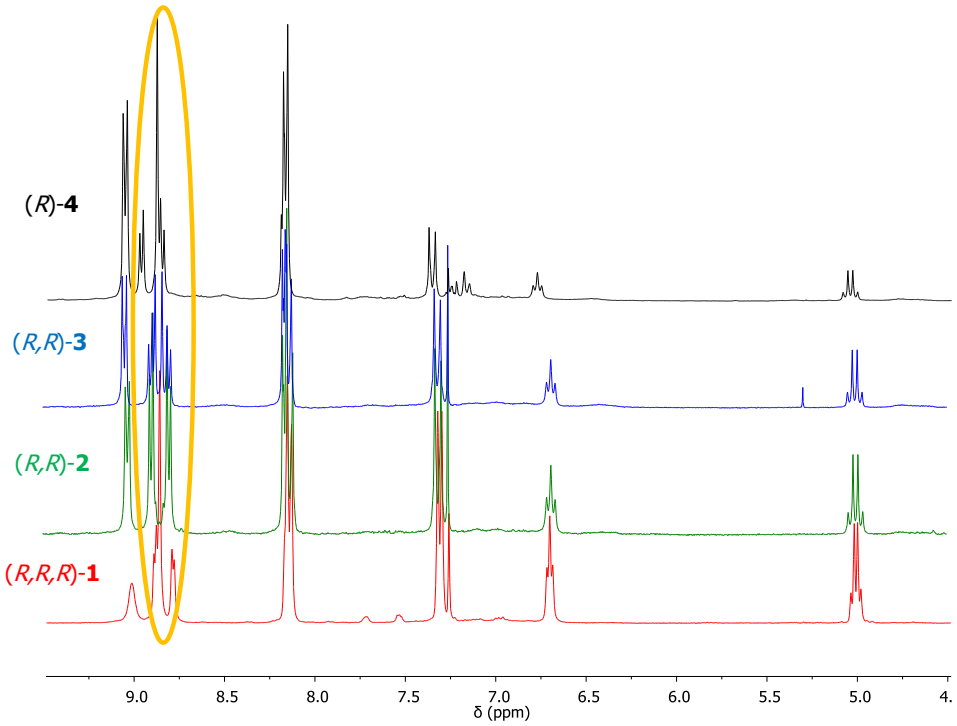

Figure 8. ^{1}H-NMR spectra of free-base porphyrins (*R,R,R*)-**1**, (*R,R*)-**2**, (*R,R*)-**3** and (*R*)-**4** in *d*-chloroform.

The decrease in intensity of the doublet located at around 7.30 ppm is evident as the number of amide groups decrease in the structure due to that this peak is associated to the H_α of the phenyl ring. In the other hand, the H_β of the phenyl ring also decrease in intensity but this variation is not so clear in the spectra because they have almost the same chemical shift as the H_β of pyridyl group at around 8.15 ppm. The variation in intensity depending on the side groups is also appreciable in the H_α of pyridyls that appear at 9.10 ppm as a doublet multiplicity.

As it mentioned before, the multiplicity of pyrrole protons changes upon changing the substitution of the chromophore ring even their integral is set at eight protons. While for porphyrins (*R,R,R*)-**1** and (*R*)-**4** the pyrrole protons are observed as a two doublets and a singlet that integrate four protons each because both porphyrins, although their substitution is different, the ratio of the number of groups is the same, being 3:1 (amide/pyridyl) or 1:3 (amide/pyridyl), ratio respectively (Figure 9).

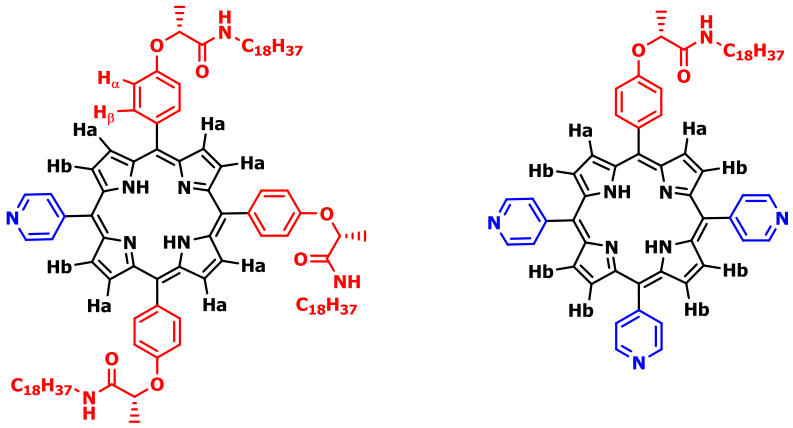

Figure 9. Pyrrole protons assignments for molecules (*R,R,R*)-**1** and (*R*)-**4**.

On the contrary, for porphyrins (*R,R*)-**2** and (*R,R*)-**3**, which both contain two chiral amide and two pyridyl groups as a substituent at the *meso* position, the variation on the position of the group in the porphyrin ring influences the multiplicity of the pyrrole protons as the same was observed in porphyrins (*R,R*)-**9** and (*R,R*)-**10** (Figure 10).

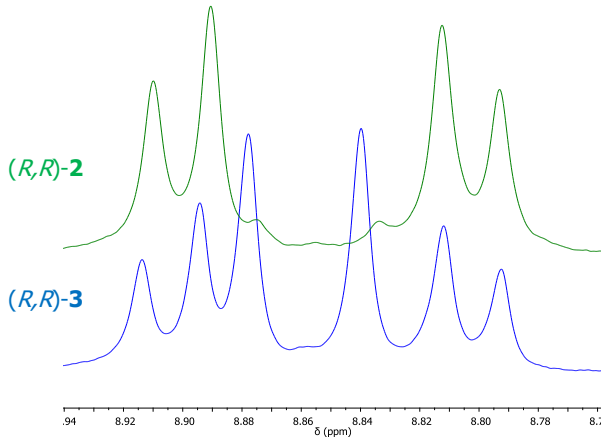

Figure 10. Pyrrole protons multiplicity in ^{1}H-NMR spectra of free-base porphyrins (*R,R*)-**2** and (*R,R*)-**3** in *d*-chloroform.

In the case of (*R,R*)-**2** the pyrrole protons appear as a double-doublet due to the symmetry of the molecule (C_{2v}) at 8.90 ppm (4H) and 8.80 ppm (4H), but in the case of porphyrin (*R,R*)-**3**, which has the amide groups in a "*cis*"-type at the 5,10 position their multiplicity change to two doublets at 8.90 and 8.80 ppm, integrating 2H each one and in the inner part of each doblet a singlet at 8.88 ppm (2H) and 8.84 ppm (2H), presenting a symmetry C_{1h} like in the case of porphyrin (*R,R*)-**10**.

2.3.4. Metallation of the desired free-base porphyrins with zinc (II) ion.

The last step of the synthesis was the metallation of the free-base porphyrins using zinc (II) acetate as a metal salt.[41] Free-base porphyrins were dissolved in CH_2Cl_2 under argon atmosphere and a solution 1:1 (CH_2Cl_2:MeOH) of zinc (II) salt was added dropwise over the reaction flask. After 3 hours of reaction, the crude was treated with an aqueous base solution in order to neutralize the acetic acid form in the process and purified by a short silica gel column chromatography affording around 75% yield as a purple metallic powder of each metalloporphyrin (Scheme 11).

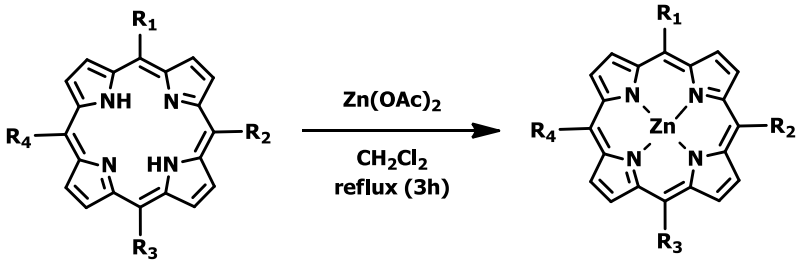

Scheme 11. Synthesis of metalloporphyrins Zn-(*R*,*R*,*R*)-**1**, Zn-(*R*,*R*)-**2**, Zn-(*R*,*R*)-**3** and Zn-(*R*)-**4**.

2.3.4.1. Analysis of the desired metalloporphyrins by ^{1}H-NMR.

When metalloporphyrins were characterized by ^{1}H-NMR an increase in the complexity of the spectra for metallocompounds were observed and was not expected. However the formation of the aggregate in the appropriate conditions for NMR studies showed complex spectra at room temperature (Figure 11).

(41) Feldborg, L. N.; Saletra, W. J.; Iavicoli, P.; Amabilino, D. B. *J. Porphyr. Phthalocya.* **2011**, *15*, 995-1003.

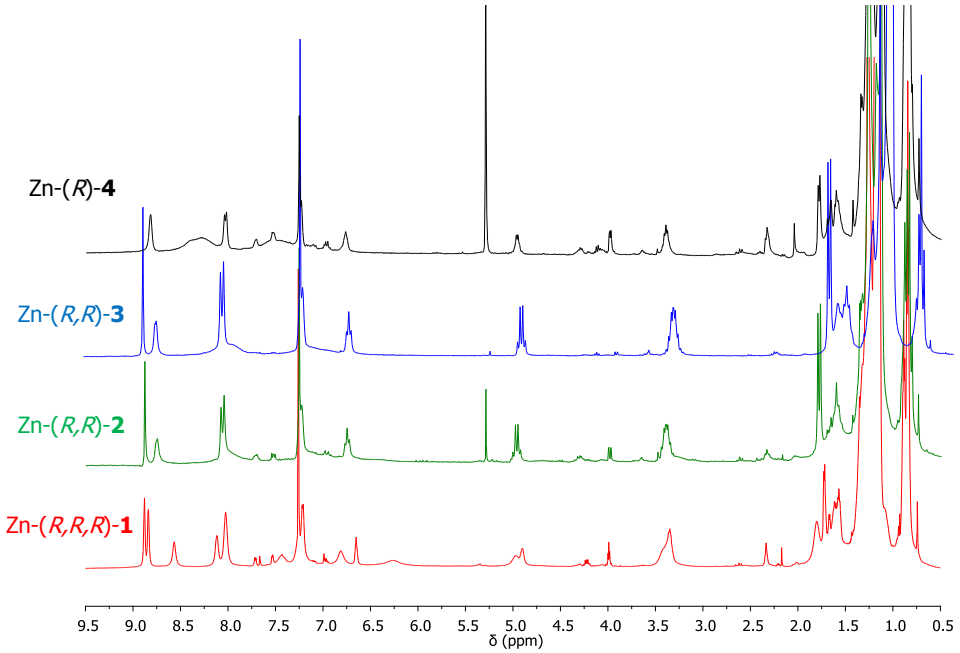

Figure 11. ^{1}H-NMR spectra metalloporphyrins Zn-(*R,R,R*)-**1**, Zn-(*R,R*)-**2**, Zn-(*R,R*)-**3** and Zn-(*R*)-**4** in *d*-chloroform.

As it could observed in the ^{1}H-NMR spectra of metalloporphyrins, the aromatic region did not show all the signals corresponding to the phenyl and pyridyl rings and neither a good assignment for pyrrole protons could be done. This behavior suggested that metalloporphyrins aggregated in chloroform at high concentrations (~20mM) increasing the complexity of the spectra.

2.4. Study of the aggregates by NMR techniques.

Metalloporphyrin Zn-(*R,R,R*)-**1** and Zn-(*R,R*)-**3** were chosen for different NMR studies in order to elucidate the aggregate structure form in solution due to they only have one pyridyl group capable to be involved in the self-assembly of the metalloporphyrin. Although Zn-(*R,R*)-**3** contain two pyridyl groups in its structure, only one of the pyridyl groups coordinated with the metal ion because steric hindrance reasons. It has been studied the ability of axial coordinating ligands as pyridyl groups to coordinate with zinc ion. In the 1990s Fleisher *et al.* reported an infinite polymeric structure from 5-pyridyl-10,15,20-triphenylporphyrinato zinc (II) either in solution or solid state whereas Hunter *et al.* reported a tetrameric structure from a zinc porphyrin when metallocompounds were studied in dilute solutions, but at higher concentrations close to the solid state behavior, linear polymers were the major supramolecular organization.

Temperature studies in the ^{1}H-NMR of Zn-(*R,R,R*)-**1** and Zn-(*R,R*)-**3** were performed in order to find the best conditions to identify all peaks of the molecule.

2.4.1. Structure elucidation of the metalloporphyrin Zn-(*R,R,R*)-1.

The working temperatures in the ^{1}H-NMR of Zn-(*R,R,R*)-**1** were 298 K, 263 K and 228 K in order to decrease the exchange rate of the protons and move the equilibrium to the aggregate form (Figure 12).

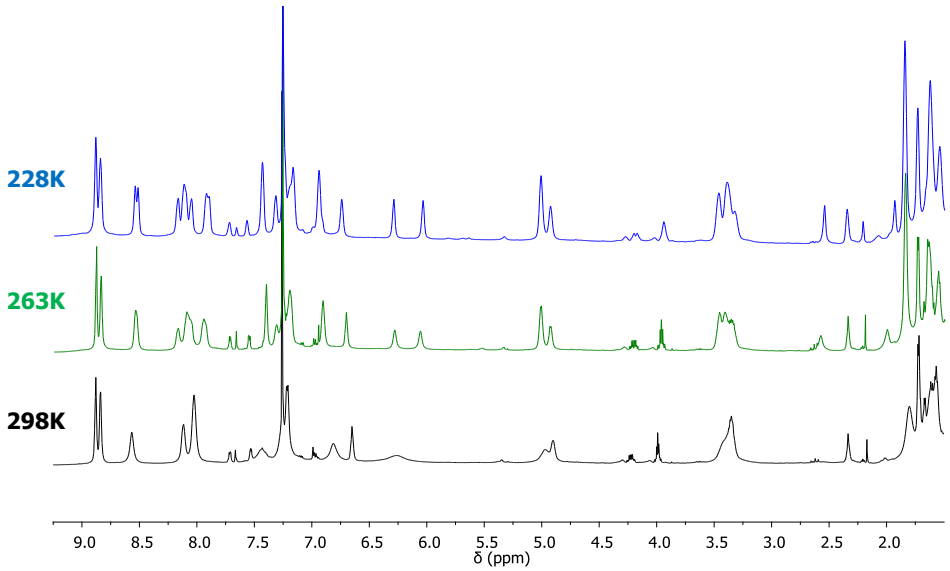

Figure 12. ^{1}H-NMR of Zn-(*R,R,R*)-**1** at 298K, 263K and 228K.

When the ^{1}H-NMR was run at room temperature only some peaks could be observe clearly in the spectra compared with the spectra at 263 and 228 K, like the doublet at 8.86 ppm, that remained unchanged at all the temperatures and it could be attributed to pyrrole protons and a second peak at 8.57 that appeared like a singlet corresponding again to pyrrole protons. If we focused in the aromatic region, some of the peaks were apparently missing related to protons of the pyridyl or even the phenyl ring connected to the amide groups because of an intermediate exchange rate on the NMR timescale between coordinated and uncoordinated forms.

When we move to the upfield region, broad peaks in the room temperature ^{1}H-NMR were observed at 4.90-4.97 and 3.36 ppm corresponding to the H_α of the stereogenic center and the -CH_2 close to the amide group, respectively. As the temperature was decreased a clear splitting of the H_α in two separate signals was observed, identifying correctly the H_α to the group in the 10 *meso* position and the one in the 5,15 positions.

When the spectra at 263 and 228 K were compared, small differences could be appreciated, but the ^{1}H-NMR at 228 K showed clear multiplicity for some of the peaks in the aromatic region.

When the ^{1}H-NMR spectrum at 228 K of metalloporphyrin Zn-(*R,R,R*)-**1** was compared with the spectrum of the free-base porphyrin (*R,R,R*)-**1** in *d*-chloroform a splitting and shift was observed,

mostly for phenyl a pyridyl protons close to the porphyrin ring because the two faces of porphyrin are not equivalent due to the coordination of the pyridyl group to the zinc (II) ion (Figure 13).[42,43,44,45]

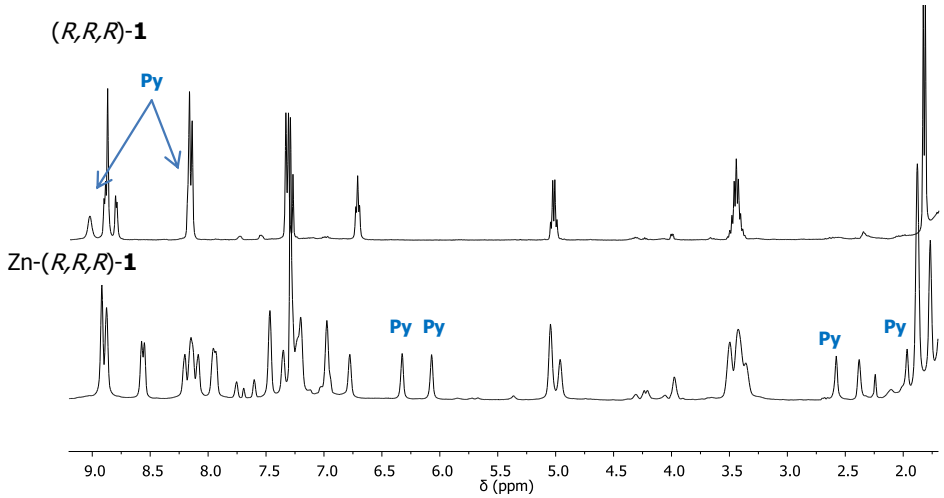

Figure 13. ^{1}H-NMR in *d*-chloroform of metalloporphyrin Zn-(*R,R,R*)-**1** and free-base (*R,R,R*)-**1.**

It was clearly evidenced the tremendous shift suffered by the pyridyl protons take into account that for free-base porphyrins appeared as a doblets at 8.88 ppm and 8.17 ppm hidden by pyrrole peak and phenyl peak respectively while for metalloporphyrin Zn-(*R,R,R*)-**1** H_{β}-pyridyl protons shift and split up to 6.32 and 6.07 ppm and for H_{α}-pyridyl protons, they shift to upper fields appearing as singlets at 2.58 and 1.97 ppm. However, the complexity of the ^{1}H-NMR spectrum of metalloporphyrin Zn-(*R,R,R*)-**1** required 2D ^{1}H-NMR studies in order to identify correctly all the protons of the molecule. For this purpose, a ROESY (Rotating Frame Overhauser effect spectroscopy) experiment was used to fully assign the spectrum considering that this technique allows the determination of which protons are close to each other even if they are not connected by covalent bonds, since the technique measures both, through bond and through space interactions, each with different phase in the 2D spectrum (Figure 14).[46]

(42) Koepf, M.; Conradt, J.; Szmytkowski, J.; Wytko, J. A.; Allouche, L.; Kalt, H.; Balaban, T. S.; Weiss, J. *Inorg. Chem.* **2011**, *50*, 6073-6082.
(43) Tsuda, A.; Nakamura, T.; Sakamoto S.; Yamaguchi, K.; Osuka, A. *Angew. Chem. Int. Ed.* **2002**, *41*, 2817-2821.
(44) Khan, T. K.; Ravikanth, M. *Tetrahedron* **2012**, *68*, 830-840.
(45) Gardner, M.; Guerin, A. J.; Hunter, C. A.; Michelsen, U.; Rotger, C. *New J. Chem.* **1999**, 309-316.
(46) Lang, T.; Graf, E.; Kyritsakas, N.; Hosseini, M. W. *Chem. Eur. J.* **2012**, *18*, 10419-10426.

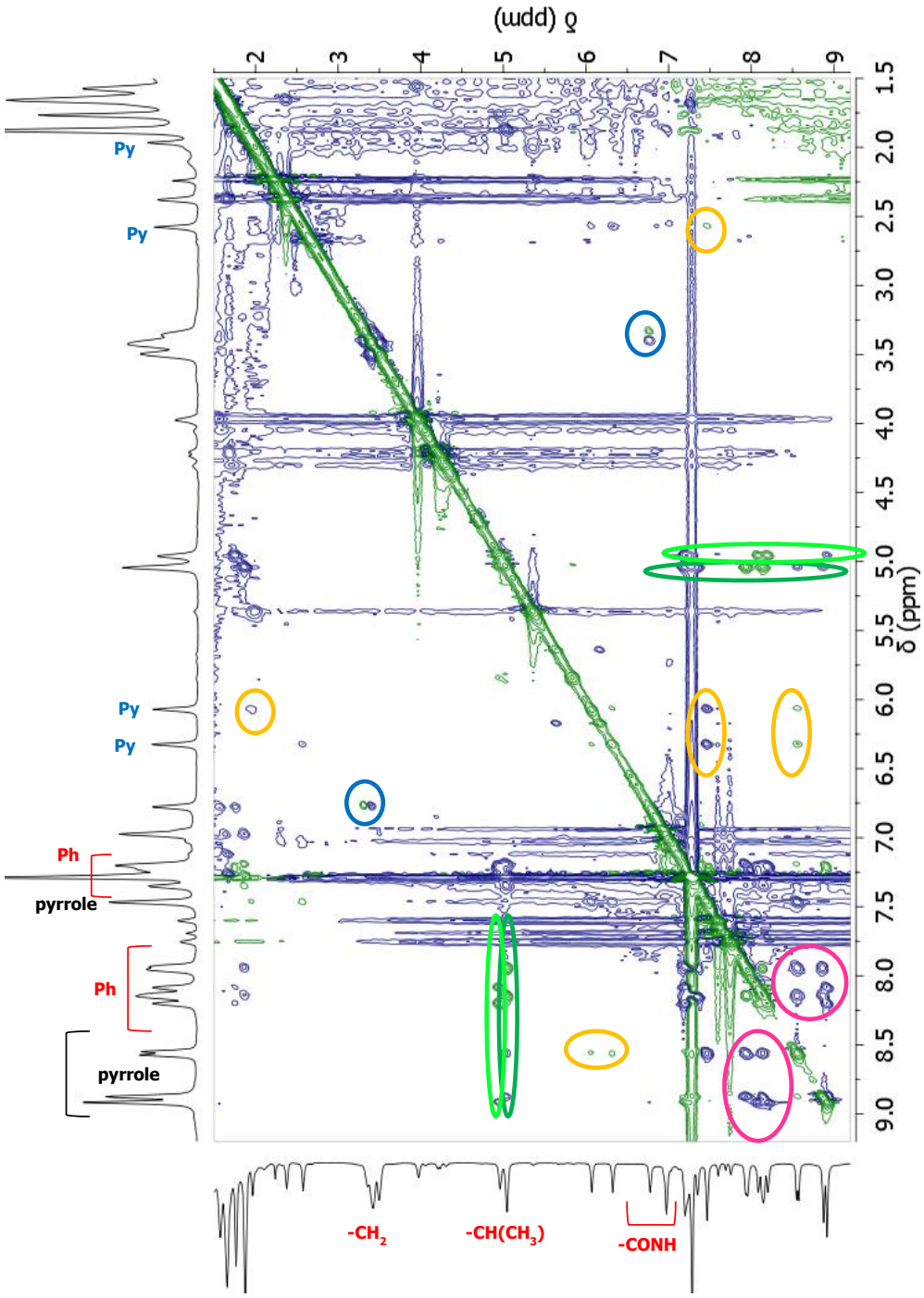

Figure 14. ROESY spectrum of compound Zn-(*R*,*R*,*R*)-**1** at 228K in *d*-chloroform.

Taking as a reference the peaks of the protons at the chiral center at the 5,15 and 10 *meso* positions at 5.04 and 4.96 ppm respectively, we could distinguish the peaks corresponding to the

phenyl ring in the *meso* position 10 and the ones attributed to the aromatic protons at the 5,15 *meso* positions. Moreover the pyridyl protons assigned previously when the ^{1}H-NMR spectrum of metalloporphyrin Zn-(*R,R,R*)-**1** was compared with the free-base porphyrin help us to the assignation for the pyrrole protons, distinguishing between the AB system protons (8.56 and 7.47 ppm) and the corresponding to an A system (8.90 ppm). The position for the pyrrole protons make sense because the ones corresponding to A systems do not modify too much their position, due to the fact that they are farther from the ring current effect. As could observe in the ROESY spectrum, the amide protons (6.97 and 6.78 ppm) did not show further correlations except with the $-CH_2$ next to them, but is important to note that only amide proton in the 10 position showed correlation. Therefore, the lack of correlation for these protons could be an indication of hydrogen-bonding between amide groups of the neighbour porphyrin.

Figure 15 shows the proposed tetramer structure for the metallo-derivate Zn-(*R,R,R*)-**1** assuming this kind of aggregate as more plausible structure due to the results observed in the ^{1}H-NMR spectrum and the literature precedent for zinc (II) pyridyl porphyrins in solution and in the solid state.[17] The arrows indicate the correlation between protons extract from ROESY studies. The arrows between hydrogens with covalent bonded correlations are not indicated for greater clarity of the drawing.

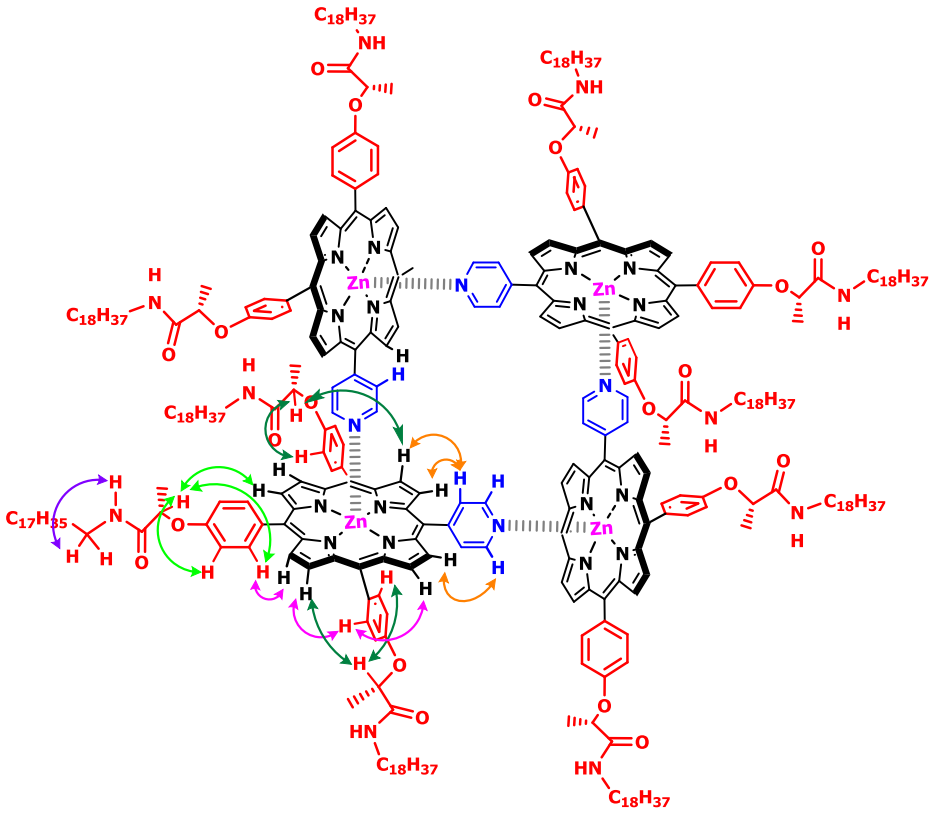

Figure 15. Tetramer structure of compound Zn-(*R*,*R*,*R*)-**1** which through space ^{1}H-^{1}H coupling undirected.

In order to corroborate that for metalloporphyrins a discrete tetramer structure is formed at high concentrations in a *d*-chloroform solution, a diffusion NMR spectroscopy study was perform. This technique allow to determine de diffusion coefficient of a certain molecule, giving information about the molecular weight of the molecule or the supramolecular form in this solvent, as well as important information about the shape and size of the architecture under study. The specific diffusion technique used was the Pulsed gradient spin echo (PGSE).[47]

The diffusion coefficient (D) can be described by the following equation 1.

$$\ln\frac{I}{I_0} = -\gamma^2 G^2 \delta^2 \left(\frac{\Delta - \delta}{3}\right) D = -bD$$

Equation 1. Diffusion equation for a PGSE experiment.

The diffusion coefficient can be deduced by the relation I/I_0 where I_0 is the intensity of a certain signal and I is the intensity of the echo signal after applying a pulsed gradient. γ is the

(47) Cohen, Y.; Avram, L.; Frish, L. *Angew. Chem. Int. Ed.* **2005**, *44*, 520-554.

gyromagnetic radio, G is the pulsed gradient strength applied in the experiment, Δ is the time separation between the pulsed gradient and δ is the duration time of the pulsed. All parameters kept constant during the experiment except the pulse gradient strength (G) that is increasing each time that the pulsed is applied.

PGSE study were performed with metalloporphyrin Zn-(*R,R,R*)-**1** in *d*-chloroform at 263 K. Moreover, the experiment was also run with the same metalloporphyrin but adding MeOH in the NMR tube in order to disaggregate the structure and analyse the monomer specie. Figure 16 shows the PGSE spectra of metalloporphyrin Zn-(*R,R,R*)-**1**.

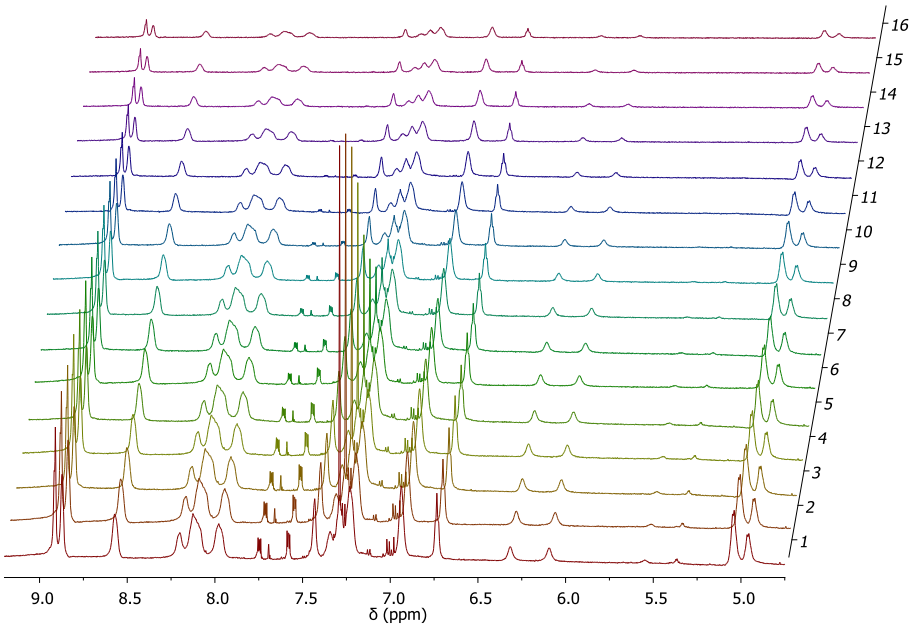

Figure 16. PGSE in *d*-chloroform of metalloporphyrin Zn-(*R,R,R*)-**1** at 263K.

As it could observe in the spectra, the intensity of the peaks decrease as the pulsed gradient strength increase. As mentioned before the experiment was run with metalloporphyrin Zn-(*R,R,R*)-**1** with a drop of MeOH in order to registered the spectra of the monomer compound (Figure 17).

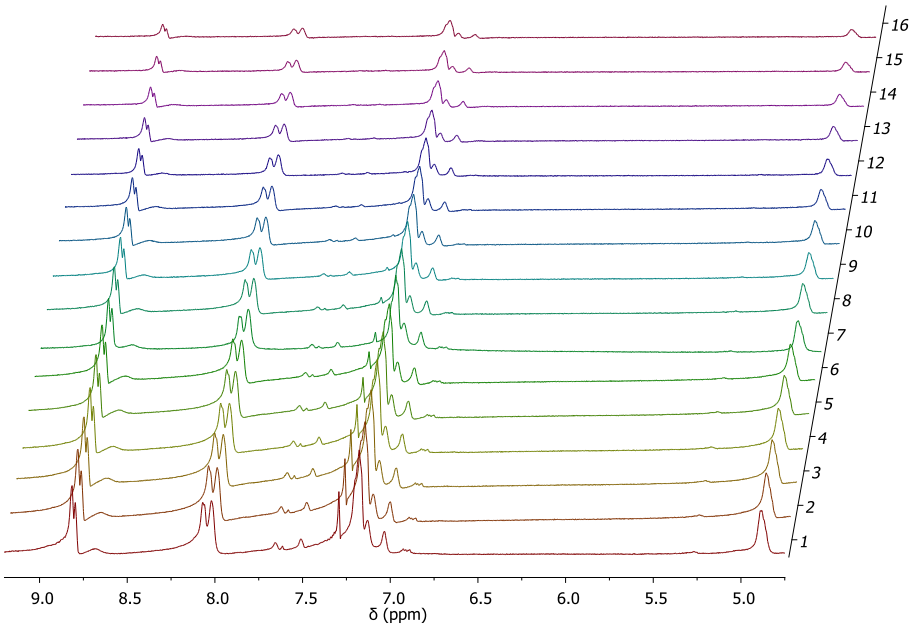

Figure 17. PGSE in *d*-chloroform of metalloporphyrin Zn-(*R,R,R*)-**1** + MeOH at room temperature.

In order to calculate the diffusion coefficient, one of the peaks was chosen to follow its evolution intensity in function of the b factor. The pyrrole proton at 8.61 ppm was chosen for metalloporphyrin Zn-(*R,R,R*)-**1** while the proton in the chiral position at 4.88 ppm was chosen when the MeOH was added in the *d*-chloroform solution of the metalloporphyrin (Figure 18).

G= 53.3 G/m
δ= 7.75 μs
Δ= 100 ms

Figure 18. Graphic analysis data for Zn-(*R,R,R*)-**1** and Zn-(*R,R,R*)-**1** + MeOH.

Figure 18 shows the evolution of the intensity of the peaks versus the b value that as the equation shows $b = -\gamma^2 G^2 \delta^2 \left(\frac{\Delta-\delta}{3}\right)$. Extracting from the sloop of each curve, the diffusion coefficient (D) value for Zn-(*R,R,R*)-**1** and Zn-(*R,R,R*)-**1** + MeOH respectively was $1.51 \cdot 10^{-5}$ cm^2/s

and $1.43 \cdot 10^{-5}$ cm^2/s. As it was shown in the graphic, monomeric specie and aggregate compound present a similar diffusion coefficient value, suggesting that the relative molecular weight for each one is similar and a tetrameric structure is plausible with the results observed.

2.4.2. Structure elucidation of the metalloporphyrin Zn-(*R,R*)-3.

When temperatures studies were performed for metalloporphyrin Zn-(*R,R*)-**3** in the range of temperatures from 298 K to 228 K the spectra did not show a clear signals as in the case of metalloporphyrin Zn-(*R,R,R*)-**1**. Nevertheless the peaks observed in the ^{1}H-NMR spectrum of Zn-(*R,R*)-**3** at 233 K even they did not show a precise multiplicity, allowed us the assignment of some of the protons (Figure 19).

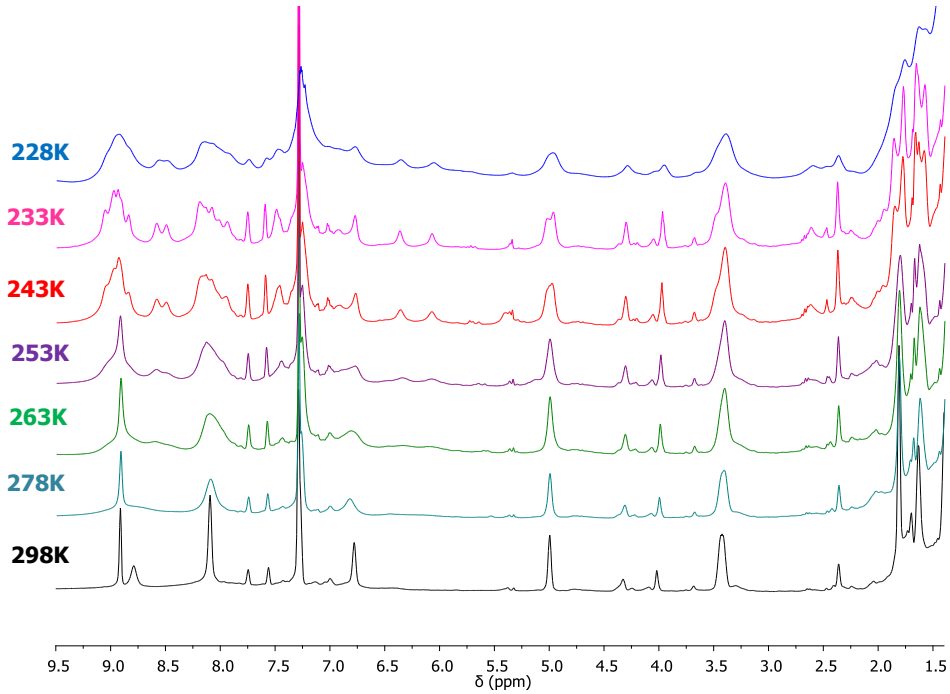

Figure 19. ^{1}H-NMR of Zn-(*R,R*)-**2** at 298K, 278K, 263K, 253K, 243K, 233K and 228K.

The spectrum at 233 K shows at 5.00 and 4.94 ppm the peak corresponding for the protons in the stereogenic center being not identical due to the coordination between a pyridyl group and zinc (II) metal ion of an adjacent porphyrin, moreover we clearly could affirm that the signal located at 3.37 ppm correspond to the $-CH_2$ next to the amide groups, however the assignment in the aromatic region become more complicated due to the number of peaks.

The ^{1}H-NMR spectrum of Zn-(*R,R*)-**3** at 233 K was compared with the ^{1}H-NMR spectrum of (*R,R*)-**3** in order to assign the peaks in the aromatic region, even though the complexity of this area made difficult the assignment of all the peaks (Figure 20).

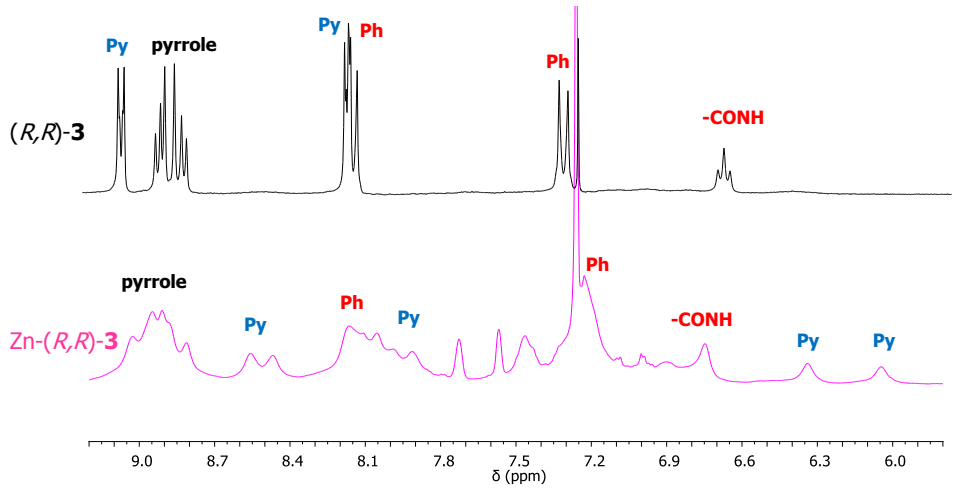

Figure 20. ^{1}H-NMR in *d*-chloroform of metalloporphyrin Zn-(*R,R*)-**3** and free-base porphyrin (*R,R*)-**3.**

As it could observed in the spectra, pyrrole protons in the metalloporphyrin kept practically invariable compared with the pyrrole protons of the free-base porphyrin, despite phenyl and pyridyl protons become more difficult to assign due to the dissymmetry of the molecule when pyridyl is coordinated with the metal ion.

It has to be noted that metalloporphyrin Zn-(*R,R*)-**3** has two pyridyl groups as a substituent in the periphery of the ring, but only one of these groups is involve in the self-assembly of the metalloporphyrin because the steric hindrance in the surrounding of the second pyridyl group. For that reason in the ^{1}H-NMR spectrum of Zn-(*R,R*)-**3** several peaks were assigned to the pyridyl group.

Two singlets are observed at 6.34 and 6.06 ppm corresponding to H_{β}-pyridyl protons of the pyridyl group involve in the aggregation, as it was observed in the spectrum of metalloporphyrin Zn-(*R,R,R*)-**1**. On the other hand the pyridyl protons of the non-coordinated pyridyl group suffer a slightly shift up to 8.52 ppm and a non-splitting is observed for this protons.

2.5. Study of the self-assembly of free-base porphyrins and metalloporphyrins in solution.

The porphyrins and metalloporphyrins synthesized here were prepared to be able to self-assemble in solution by different non-covalent interactions such as hydrogen bonding and π-π stacking interactions directly related with the π-conjugated skeleton or by coordination with the metal ion in the core of porphyrin.[48]

(48) Takeuchi, M.; Tanaka, S.; Shinkai, S. *Chem. Commun.* **2005**, 5539-5541.

2.5.1. General aspects of UV-Visible absorption spectroscopy and circular dichroism.

UV-Visible absorption spectroscopy is a good technique to study the aggregation of the chromophores because the electronic π-π* transitions typical for these compounds are extremely sensitive to the aggregation state. As explained in the main introduction, free-base porphyrins and metalloporphyrins present an intense band at around 420 nm (Soret band) and four Q-bands with weak intensity in the case of free-base porphyrins, while metalloporphyrins due to their higher symmetry only present two or less in the visible region (500 nm to 700 nm).

For some metalloporphyrins this Soret band can be shifted to lower wavelength because the influence of the metal on the relative energy transitions of the chromophores ring.[15] In case of closed-shell ions (d^0-d^{10}) like zinc (II) a weak effect is shown on the π-π* gap, meaning that Soret band does not move significantly with respect to the free-base porphyrin.[49,50,51] This band provides us with useful information for the study of aggregation of our compounds because give the type of aggregate that is formed can give rise to very different changes in the absorption spectra. *H*-aggregate or *J*-aggregates are the main types that porphyrins can form, presenting hypsochromic shift of the Soret band for *H*-aggregates while a red shift is observed for *J*-aggregates.

Apart from that, for chiral systems circular dichroism (CD) is an excellent complementary technique to study the self-assembly of porphyrins because it is very sensitive to supramolecular structure, absolute configuration, and futures that are difficult detected in other spectroscopic techniques. CD has been used to study secondary structures for many biochemical systems such as proteins,[52] amino acids,[53] DNA[54] or sugars,[55] but from this pretext, this chiroptical technique has become an important tool to study and follow the evolution in the bottom-up approach to chiral nanomaterials.[56]

CD principals are based in the absorption difference of left and right elliptical polarized light, being a racemic mixture giving a flat line CD signals. The CD band position is correlated with the

(49) Gouterman, M. *J. Mol. Spectros.* **1961**, *6*, 138-163.
(50) Prushan, M. "Absorption and Fluorescence Spectroscopy of Tetraphenylporphyrin and Metallo-Tetraphenylporphyrin," **2005**.
(51) Hashimoto, T.; Choe, Y-T.; Nakano, H.; Hirao, K. *J. Phys. Chem. A* **1999**, *3*, 1894-1904.
(52) Nakagawa, K.; Yamada, Y.; Matsumura, Y.; Tsukamoto, S.; Yamamoto-Ohtomo, M.; Ohtomo, H.; Okabe, T.; Fujiwara, K.; Ikeguchi, M. *Biopolymers* **2013**, *101*, 651-658.
(53) Bredehöft, J. H.; Jones, N. C.; Meinert, C.; Evans, A. C.; Hoffmann, S. V.; Meierhenrich, U. J. *Chirality* **2014**, *26*, 373-378.
(54) Chauca-Díaz, A. M.; Choi, Y. J.; Resendiz, M. J. E. *Biopolymers* **2014**, *103*, 167-174.
(55) Quesada-Moreno, M. M.; Azofra, L. M.; Avilés-Moreno, J. R.; Alkorta, I.; Elguero, J.; López-González, J. J. *J. Phys. Chem. B* **2013**, *117*, 14599-14614.
(56) Gottarelli, G.; Lena, S.; Masiero, S.; Pieraccini, S.; Spada, G. P. *Chirality* **2008**, *20*, 471-485.

absorption band of the molecule becomes a positive or negative dichroic signal (or Cotton effect) depending on the difference in left or right handed light absorption.

Theoretically, a dichroic signal is described by an electronic transition where the electric dipole moment and the magnetic dipole moment interact due to the helical path of light and are not orthogonal between them.

The intensity and position of these bands might be affected by the perturbation in the surrounding of the chromophore in the molecule, but in most of the cases, in the self-assembly process, the most important factor in the rotational strength (CD intensity) comes from the chromophore-chromophore transition interactions that when close in space and properly oriented is called exciton coupling. In that case is a splitting of the excited state occurs, the energy difference between them being called the Davydov splitting. So, in the case of porphyrins, highly π-conjugated systems with a maximum absorption band at around 420nm, the coupling between two or more of these chromophores gives rise to an intense CD signal with large amplitude.[57]

As mentioned before, CD spectropolarimetry allows the determination of the supramolecular structure of the aggregates formed in solution, although this assignment is not straightforward the transfer of chirality from the monomer to the aggregate structure is non-trivial. One can associate Cotton effect to different orientations of the electronic transitions between chromophores and then derive the final configuration of the superstructure.[58]

2.5.2. Study of the self-assembly of free-base porphyrins.

2.5.2.1. Study of the self-assembly by UV-Visible absorption spectroscopy.

Solutions in methylcyclohexane of free-base porphyrins (*R,R,R*)-**1**, (*R,R*)-**2**, (*R,R*)-**3** and (*R*)-**4** at the concentration of 5 μM were used to study their self-assembly. Methylcyclohexane was convenient to study the optical properties of the aggregates because it is transparent in the visible and near ultraviolet region, where porphyrins absorb. This solvent is apolar and should favor the formation of hydrogen-bonds between molecules where they are possible.[59] Figure 21 shows the UV-Visible absorption spectra of the free-base porphyrins. None of these porphyrins present any sign of aggregation considering that there was no evidence of splitting of the Soret band located around 420 nm to lower or higher wavelength, suggesting that the isolated porphyrin is the only specie present in solution.

(57) Berova, N.; Di Bari, L.; Pescitelli, G. *Chem. Soc. Rev.* **2007**, *36*, 914–931.
(58) Pescitelli, G.; Di Bari, L.; Berova, N. *Chem. Soc. Rev.* **2011**, *40*, 4603–4625.
(59) Balaban, T. S. *Acc. Chem. Res.* **2005**, *38*, 612-623.

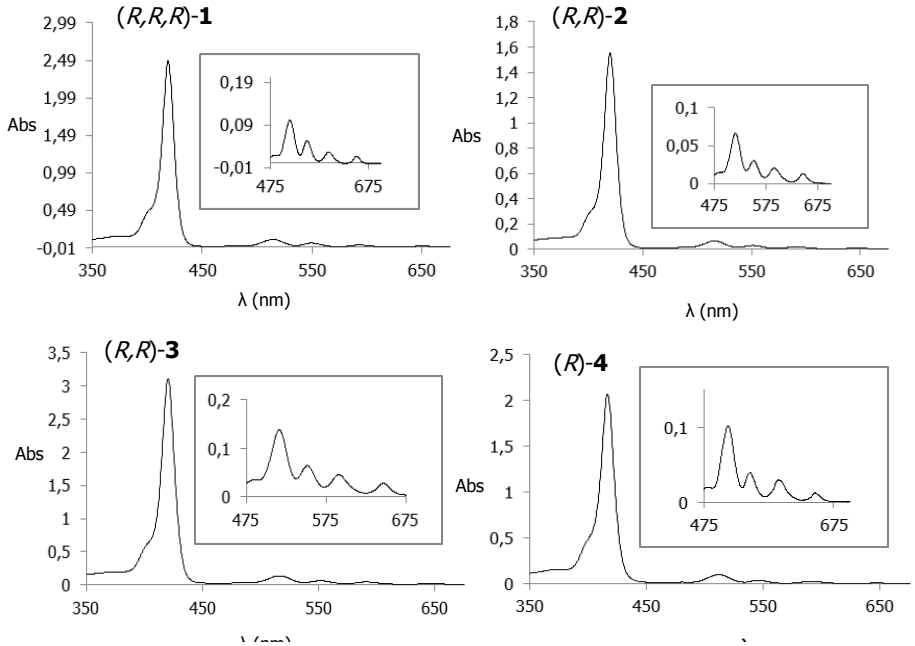

Figure 21. UV-Visible absorption spectra of free-base porphyrins (*R,R,R*)-**1**, (*R,R*)-**2**, *(R,R*)-**3** and (*R*)-**4** at room temperature in methylcyclohexane (5 μM).

One would expect these compounds to self-aggregate in the appropriate solvent taking into account that they have amide groups as substituent in the *meso* positions that could drive the aggregation by hydrogen-bonding between them. Nevertheless as shown in the spectra it can be affirmed that the non-covalent interactions were not strong enough to drive the organization in supramolecular stacks of the free-base porphyrins. This lack of interaction is not wholly surprising, because the compound bearing four chiral chains does not aggregate appreciably either.[39] It is believed that the methyl group attached to the stereogenic center interferes sterically with the hydrogen-bonding interaction. The presence of the pyridyl groups in the side position could also influence (one way or another) their formation, even in the case of porphyrin (*R,R,R*)-**1** that were construct by three chiral amide groups and only one pyridyl in the periphery of the chromophore ring. Yet not significant effect could be observed.

2.5.2.2. Study of the self-assembly by Circular dichroism (CD).

CD measurements were run with solutions of free-base porphyrins (*R,R,R*)-**1** and (*R,R*)-**3** in methylcylcohexane (5 μM) at 263 K in order to see if temperature had some effect in the formation of the aggregates (Figure 22).

The first thing to highlight is that the compounds do not show significant optical activity in their molecularly dissolved state at room temperature (spectra non shown) because the stereogenic

centers are located far from the porphyrin chromophore. Therefore the compounds can be regarded as being cryptochiral.[60]

Figure 22. CD spectra at 263 K of free-base porphyrins (*R,R,R*)-**1** and *(R,R*)-**3** in methylcyclohexane (5 μM).

As observed in the CD spectra, even at low temperature, porphyrins (*R,R,R*)-**1** and (*R,R*)-**3** did not self-assemble significantly in this solvent and at this concentration conditions, corroborating the results observed in the UV-Visible absorption spectra registered at room temperature. Compound (*R,R*)-**3** does show a small Cotton effect, but this weak signal could arise either from molecular chirality or from noise from the spectropolarimeter around the absorption maximum of the Soret Band.

2.5.3. Study of the self-assembly of metalloporphyrins.

When zinc (II) metal ion is introduced into the core of the porphyrin ring, a center of coordination is generated because of the ability of the metal to coordinate with axial atoms such as nitrogen and oxygen. Zinc (II) porphyrins readily accept one axial ligand[61] and an occasion

(60) Gibson, S. E.; Rendell, J. T. *Chem. Commun.* **2008**, 922-941.
(61) Diskin-Posner, Y.; Patra, G. K.; Goldberg, I. *J. Chem. Soc., Dalton Trans.* **2001**, 2775-2782.

two.[62,63] Metalloporphyrins Zn-(*R,R,R*)-**1**, Zn-(*R,R*)-**2**, Zn-(*R,R*)-**3** and Zn-(*R*)-**4** contain pyridyl groups as axial ligands that could provide aggregates by the coordination of this group with the metal ion. Alternatively the self-assembly could be through the coordination of the zinc (II) ion with the carbonyl group of the amide, or even both groups could be involved in the aggregation forming a hexacoordinate supramolecular stack. Moreover, hydrogen-bonding between the amide groups could participate in the self-assembly of molecules, however, the study of the free-base porphyrins indicates that this non-covalent interaction are not strong enough to form aggregates in solution. Therefore, one might expect that hydrogen-bonding will not be involved in the formation of the supramolecular arrangement of metalloporphyrins either.

2.5.3.1. Study of the self-assembly by UV-Visible absorption.

Variable temperature studies were performed in UV-Visible absorption in $CHCl_3$ and methylcyclohexane/3% $CHCl_3$ (the small percentage of $CHCl_3$ used was helpful to solubilize the metallocompounds in methylcyclohexane solution, due to the lower solubility of these porphyrins in this solvent compare with the free-base compounds. The zinc (II) porphyrins became more insoluble as the number of amide groups bonded to the long alkyl chain increase in the structure. Solutions of zinc (II) porphyrins Zn-(*R,R,R*)-**1**, Zn-(*R,R*)-**2**, Zn-(*R,R*)-**3** and Zn-(*R*)-**4** at 5μM were used to follow the evolution of the aggregate formation for both solvents. In $CHCl_3$ the porphyrins are completely soluble and non-aggregated, while methylcyclohexane reveals aggregate formation.

Figure 23 shows the evolution of the Soret band and Q-bands of Zn-(*R,R,R*)-**1** in a $CHCl_3$ solution when UV-Visible absorption was performed at different temperatures.

Figure 23. UV-Visible absorption spectra of Zn-(*R,R,R*)-**1** in $CHCl_3$ (5 μM) at different temperatures.

(62) Teo, T.-L.; Vetrichelvan, M.; Lai, Y.-H. *Org. Lett.* **2003**, *5*, 4207-4210.
(63) Suijkerbuijk, B. M. J. M.; Tooke, D. M.; Spek, A. L.; van Koten, G.; Gebbink, R. J. M. K. *Chem. Asian J.* **2007**, *2*, 889-903.

No clear change in the band position with temperature was observed, indicating that as could be expected by the nature of the solvent a self-aggregation of metalloporphyrin did not take place. However, when UV-Visible spectra was recorded from a Zn-(*R,R,R*)-**1** solution in methylcyclohexane/3% $CHCl_3$, the behavior was completely different (Figure 24).

Figure 24. UV-Visible absorption spectra of Zn-(R,R,R)-1 in methylcyclohexane/3% $CHCl_3$ (5 μM) at different temperatures.

As seen in the spectra, at 55ºC mainly monomeric specie is present in solution with one Soret Band at 419 nm (although a slight shoulder can be perceived at high wavelength) and one (Q_α) with a maximum at 548 nm while the second Q-band was almost inappreciable at around 589 nm. As the temperature was decreased a new band appeared at 431 nm with a maximum in relative intensity at 20ºC while the Soret band at 419 nm decreased. Below this temperature the Soret band of the aggregate decreased and a new band appeared at 451 nm when 8ºC was reached. At higher wavelength changes also were appreciated in the position and intensity of the Q-bands. While the Q_α band suffered a red shift up to 563.5 nm, the Q_β band was increased in intensity and shifted to 607 nm. The red shift of the bands and the splitting of the Soret band clearly indicated the formation of an aggregate.[18] The two isosbestic points at 525.5 and 556 nm seem to corroborate that equilibria exist between two species. The evolution of the Q-bands and the new band at 431 nm indicate that the aggregate is driven by coordination of the pyridyl group to the zinc (II) ion of a neighboring porphyrin.[64,65,66] The fact that the presence of a new band at 450 nm at lower temperatures indicated that the aggregate could evolve to another *J*-aggregate where different non-covalent interaction could play a role in the formation of the supramolecular architecture. Indeed, up to 20ºC an isosbestic point appears to be present at 425 nm, but then evolves further away from this point around 440 nm.

(64) Miller, J. R.; Dorough, G. D. *J. Am. Chem. Soc.* **1952**, *74*, 3977-3981.
(65) Kirksey, C. H.; Hambright, P.; Storm, C. B. *Inorg. Chem.* **1969**, *8*, 2141-2144.
(66) Marets, N.; Bulach, V.; Hosseini, M. W. *New J. Chem.* **2013**, *37*, 3549-3558.

When the absorption spectra of metalloporphyrin Zn-(*R,R,R*)-**1** in $CHCl_3$ and in methylcyclohexane/3% $CHCl_3$ at 8ºC and 55ºC were compared, clearly one can observed that the spectra in $CHCl_3$ and the spectrum at 55ºC in methylcyclohexane/3% $CHCl_3$ presented the same future with absorption maxima more or less in the same wavelength position, even though, as mentioned before Zn-(*R,R,R*)-**1** in methylcyclohexane/3% $CHCl_3$ aggregates showing a red-shift of the Q-bands and a new band related to the *J*-aggregate at around 435 nm (Figure 25).

Figure 25. UV-Visible absorption spectra of Zn-(*R,R,R*)-**1** in methylcyclohexane/3% $CHCl_3$ and in $CHCl_3$ at 8ºC and 55ºC.

The UV-Visible absorption spectra at different temperatures of metalloporphyrin Zn-(*R,R*)-**2** that contain the chiral amide groups in the 5, 15 *meso* positions of the porphyrin ring in $CHCl_3$ did not show any evidence of self-assembly because there was no splitting of the Soret band located at 420.5 nm, non were the Q-bands were shifted to higher wavelength when temperature decreased indicating aggregation, although a very slight broadening was observed at 10ºC both in the Soret band and in the Q_β band specially (Figure 26).

Figure 26. UV-Visible absorption spectra of Zn-(*R,R*)-**2** in $CHCl_3$ (5 μM) at different temperatures.

A solution of the same metalloporphyrin Zn-(*R,R*)-**2** (5 μM) in methylcyclohexane was studied by UV-Visible absorption spectroscopy at different temperatures (Figure 27).

Figure 27. UV-Visible absorption spectra of Zn-(*R,R*)-**2** in methylcyclohexane/3% $CHCl_3$ (5 μM) at different temperatures.

The UV-Visible absorption spectra of Zn-(*R,R*)-**2** in the less polar solvent clearly shows the presence of aggregates in solution due to the new red shifted band at 452.5 nm and the shifted and high relative intensity of the Q_β band. The behavior in the self-assembly of this metalloporphyrin seemed completely different compared with porphyrin Zn-(*R,R,R*)-**1** because in the latter an intermediate state of aggregation appeared to be present. Monomeric metalloporphyrin Zn-(*R,R*)-**2** was in equilibria with an apparent *J*-aggregate in the whole range of temperatures studied as can be observed in the appearance of the spectra and by the presence of an isosbestic point at around 435 nm.

Comparing the absorption spectra of metalloporphyrins Zn-(*R,R,R*)-**1** and Zn-(*R,R*)-**2** in methylcyclohexane/3% $CHCl_3$, at lower temperature Zn-(*R,R,R*)-**1** started to evolve to another aggregate which presented a band at 451.0 nm, suggesting that the same kind of aggregate was formed that for metalloporphyrin Zn-(*R,R*)-**2** in the whole range of temperatures (although, there are difference at lower wavelength) (Figure 28).

Figure 28. UV-Visible absorption spectra of Zn-(R,R,R)-1 and Zn-(R,R)-2 in methylcyclohexane/3% CHCl3 at 8ºC and 10ºC respectively.

Metalloporphyrin Zn-(*R,R*)-**3** showed in the UV-Visible absorption spectra in $CHCl_3$ a slight differences compare with the other two metalloporphyrins observed before (Figure 29). A red shifted shoulder in the Soret band position was clearly appreciated, being more evident as the temperature decreased. Moreover, the aggregation process was easy to recognize in the Q-bands region, where the Q_α band became broader while the Q_β band clearly shifted to higher wavelength and increased in intensity.

Figure 29. UV-Visible absorption spectra of Zn-(*R,R*)-**3** in $CHCl_3$ (5 μM) at different temperatures.

These observation suggested that Zn-(*R,R*)-**3** forms an aggregate through pyridyl-Zn (II) coordination, corroborated by the presence of an isosbestic point at 425 nm, but the Q-bands really indicate the coordination of the zinc (II) ion in the axial position by a pyridyl group of a consecutive metalloporphyrin.

The UV-Visible absorption spectra of this porphyrin in methylcyclohexane/3% $CHCl_3$ is shown that the tendency of aggregation of that compound was the formation of an aggregate by the coordination of the zinc (II) metal ion of one porphyrin with a pyridyl group of the consecutive porphyrin as happened for the others metalloporphyrins as well as for this metalloporphyrin in $CHCl_3$ (Figure 30).

As can be observed the absorption spectra of metalloporphyrin Zn-(*R,R*)-**3** do not present huge differences upon variation of the temperature, meaning that in all this range of temperatures isolated porphyrin and aggregated porphyrin coexisted in solution as suggested by the overlapping of the Soret band of the monomer with maximum at 419.5 nm and the band associated to the aggregate formed by coordination pyridyl-Zinc (II) ion at 435.0 nm. However, it is not possible from these spectra to rule over the formation of an aggregate where the porphyrin absorbs at the same position as the free-base porphyrin. Furthermore, a higher wavelength the position and intensity of Q-bands confirmed the self-assembly of metalloporphyrin Zn-(*R,R*)-**3**.

Figure 30. UV-Visible absorption spectra of Zn-(*R,R*)-**3** in methylcyclohexane/3% $CHCl_3$ (5 μM) at different temperatures.

Figure 31 shows a comparison spectra of metalloporphyrin Zn-(*R,R*)-**3** at low and high temperatures in the two solvents used for the measurements. As mentioned before Zn-(*R,R*)-**3** aggregated in methylcyclohexane/3% $CHCl_3$ and even in $CHCl_3$ at low temperatures the spectrum suggested an aggregation tendency for the metalloporphyrin, corroborated by the same red-shift for the Q-bands, specially Q_β band.

Figure 31. UV-Visible absorption spectra of Zn-(*R,R*)-**3** in methylcyclohexane/3% $CHCl_3$ and in $CHCl_3$ at 8ºC and 45ºC.

As can observed in the Soret band region, when the spectra were registered in methylcyclohexane/3% $CHCl_3$ broadening of the bands were appreciated compare with the spectra registered in $CHCl_3$ might be due to the coexistence of the two species in solution, the fact that the relative intensity of the Soret band of the monomer as well as the Soret band related to the tetrameric aggregate decrease.

The UV-Visible spectra for metalloporphyrin Zn-(*R*)-**4** in $CHCl_3$ solution suggest that this metalloporphyrin aggregate in this solvent in a clear way whereas metalloporphyrins Zn-(*R,R,R*)-**1** and Zn-(*R,R*)-**2** did not present any evidence of aggregation (Figure 32).

Figure 32. UV-Visible absorption spectra of Zn-(*R*)-**4** in $CHCl_3$ (5 μM) at different temperatures.

A perfect shoulder formation was observed at 430 nm as the temperature was decreased, indicating a self-assembly process took place. The position of the new band suggested coordination of the metal ion with a pyridyl group of another porphyrin, corroborated by the evolution of the Q-bands. While Q_α band was red shifted with a clear isosbestic point at 554 nm, indicative of equilibria between two different species in solution, the Q_β band increased its relative intensity as the temperature decreased.

When the UV-Visible absorption spectra were recorded for a solution of metalloporphyrin Zn-(*R*)-**4** in methylcyclohexane/3% $CHCl_3$, the process of the self-assembly was completely different (Figure 33).

Figure 33. UV-Visible absorption spectra of Zn-(*R*)-**4** in methylcyclohexane/3% $CHCl_3$ (5 μM) at different temperatures.

The spectrum shows a very strong tendency for metalloporphyrin Zn-(*R*)-**4** to aggregate in methylcyclohexane/3% $CHCl_3$ due to the presence of two different Soret bands in the whole range of temperatures even at 65ºC. While some of the absorption associated with the band at 416.5 nm corresponds to the monomer porphyrin, which decreases in intensity with increasing temperature,

an absorption band at approximately 423 nm persist and a band associated with a larger *J*-aggregates at 451 nm increases at lower temperatures.

Nevertheless, regarding the spectra of this metalloporphyrin in $CHCl_3$ clearly presented a different behavior in their self-assembly as was observed by the different position for the Soret band of the aggregate when the spectra in the two different solvents were compared (Figure 34).

Figure 34. UV-Visible absorption spectra of Zn-(*R,R*)-**3** in methylcyclohexane/3% $CHCl_3$ and in $CHCl_3$ at 8ºC and 45ºC.

Is important to note the different behavior in the self-assembly of each metalloporphyrin, either in $CHCl_3$ or in methylcyclohexane/3% $CHCl_3$, considering the important role of the solvent in the self-assembly process of porphyrins.[67] Whereas Zn-(*R,R,R*)-**1** and Zn-(*R,R*)-**2** did not present any evidence of self-aggregation in $CHCl_3$ solution and the porphyrins behave as isolated chromophores surrounded by solvent,[68,69,70] metallocompounds Zn-(*R,R*)-**3** and Zn-(*R*)-**4** really showed a tendency to form an aggregate drive by the coordination of Zinc (II) ion by the pyridyl group (Figure 35).

(67) van Hameren, R.; van Buul, A. M.; Castriciano, M. A.; Villari, V.; Micali, N.; Schon, P.; Speller, S.; Scolaro, L. M.; Rowan, A. E.; Elemans, J. A. A. W.; Nolte, R. J. M. *Nano Lett.* **2008**, *8*, 253-259.
(68) Abbel, R.; Van Der Weegen, R.; Meijer, E. W.; Schenning, A. P. H. J. *Chem. Commun.* **2009**, 1697-1699.
(69) Zhang, L.; Che, Y.; Moore, J. S. *Acc. Chem. Res.* **2008**, *41*, 1596-1608.
(70) Cui, H.; Chen, Z.; Zhong, S.; Wooley, K. L.; Pochan, D. J. *Science* **2007**, *317*, 647-650.

Figure 35. UV-Visible absorption spectra of Zn-(*R,R,R*)-**1**, Zn-(*R,R*)-**2**, Zn-(*R,R*)-**3**, Zn-(*R*)-**4** in $CHCl_3$ (5 μM) at 10ºC.

This distinct behavior could be related with the different position of the side groups in the porphyrin ring as well as the different number of coordinating ligands as a substituent in the periphery of the chromophore. Moreover, the solubility of each metalloporphyrin is an important factor to bearing in mind, because as the number of pyridyl groups increase in the structure, the solubility of the compound decrease, favoring also the self-assembly in a non-coordinating solvent as the $CHCl_3$ is. It seems easy to understand the distinct behavior of metalloporphyrins Zn-(*R,R,R*)-**1** and Zn-(*R*)-**4** due to the different polarity and solubility of both compounds, Zn-(*R,R,R*)-**1** being more soluble because the long alkyl chains in the side positions as we could observe in the synthesis of these porphyrins. However, the two conformational isomers behave in a different manner in $CHCl_3$ solution, as their spectra showed, suggesting the importance of the position for the amide and pyridyl groups in the structure at the moment of self-assembly. While Zn-(*R,R*)-**2** behaved like Zn-(*R,R,R*)-**1** in terms of aggregate formation, Zn-(*R,R*)-**3** with the two pyridyl groups in 5, 10 *meso* position tended to aggregate at lower temperature as Zn-(*R*)-**4**.

When we compare the UV-Visible absorption spectra of metalloporphyrins in methylcyclohexane/3% $CHCl_3$ at 10ºC, even though all porphyrins formed an aggregate the spectra patterns were different indicating a distinct self-assembly took place leading to unique structures (Figure 36).

Figure 36. UV-Visible absorption spectra of Zn-(*R,R,R*)-**1**, Zn-(*R,R*)-**2**, Zn-(*R,R*)-**3**, Zn-(*R*)-**4** in methylcyclohexane/3% $CHCl_3$ (5 μM) at 10ºC.

While metalloporphyrins Zn-(*R,R,R*)-**1** and Zn-(*R,R*)-**3** presented a Soret band for the aggregate at around 435.0 nm assigned previously to the coordination of pyridyl groups with the zinc (II) ion of the neighbouring metalloporphyrin. The other two metalloporphyrins Zn-(*R,R*)-**2** and Zn-(*R*)-**4** showed more red shifted bands with a maxima at 450 nm, suggesting a higher number of electronic transitions due to a formation of larger aggregate or even another kind of *J*-aggregate because of the different position of the peripherical groups. Moreover, the metalloporphyrin Zn-(*R,R,R*)-**1** presented an evolution of the aggregate from monomer to discrete aggregate and a second evolution of the aggregate started to distinguished when temperature decrease below 10ºC a new band appearing at 450 nm.

We have observed the distinct behaviour between metalloporphyrins when they were studied in $CHCl_3$ or methylcyclohexane but also, the different behaviour of one particular porphyrin in the two different solvents due to the character of the solvent. While Zn-(*R,R*)-**3** apparently tended to aggregates in both solvents in the same way, metallocompound Zn-(*R*)-**4** self-assemble in a different manner depending of the solvent. On the one hand, when Zn-(*R*)-**4** was studied in $CHCl_3$ solution it behaves as an isolated porphyrin while Zn-(*R,R*)-**3** presents a shoulder at around 435 nm. On the other hand when UV-Visible absorption spectra were recorded from a methylcyclohexane/3% $CHCl_3$ solution the self-assembly was more favorable to form a larger aggregates like Zn-(*R,R*)-**2**, suggesting that some kind of linear *J*-aggregate takes place through the 5,15 *meso* position of the pyridyl groups.

2.5.3.2. Study of the self-assembly by Circular dichroism (CD).

Circular dichroism studies were performed in order to better determine the conformation of the aggregates because this spectroscopic technique gives us more information about the orientation that the chromophores adopt with respect to one another and the intensity of CD signal is directly

proportional to the interactions between electronic transitions.[71] It is also a qualitative measure of the degree of chirality in the aggregates.

Solutions of compounds Zn-(*R,R,R*)-**1**, Zn-(*R,R*)-**2**, Zn-(*R,R*)-**3** and Zn-(*R*)-**4** in methylcyclohexane/3% $CHCl_3$ were prepared (at a concentration 5 μM), and CD spectra were recorded in the range of temperatures 338 K to 263 k after a heating and cooling cycle to probe the assembly under equilibrium conditions. All of the experiments were performed in heating cooling cycles, and usefully reversible.

The temperature dependent studies in CD of compound Zn-(*R,R,R*)-**1** showed two clearly distinct states of self-assembly. A weak Cotton effect was observed at the position of the band associated with the coordination through the pyridyl-Zn (II) porphyrin bond, suggesting that a perpendicular disposition of two metalloporphyrins took place giving as a more thermodynamically stable aggregate in the range of temperatures 300.5 K to 338 K (Figure 37, red line). The isodichroic points at 415.5 nm and 443.5 nm in the CD spectra suggest equilibria between two species, either monomer specie and cyclic tetramer or equilibrium between monomer and linear aggregate, although the cyclic tetramer is predicted to be more thermodynamically stable because all coordination sites are occupied. Furthermore in this range of temperature, a clear isosbestic point at 425.5 nm could be appreciated in the relative absorption spectra, indicating a clear co-existence of monomer metalloporphyrin with maxima band at 419.5 nm and the most stable in dilute solutions cyclic tetramer.[72] The evolution of the aggregate to a larger superstructure was observed when temperature was decreased.[73,74] A high intense positive Cotton effect with maxima at 419.5 nm and a huge negative CD signal at 450 nm were indicative of the extension of the inter-chromophore interactions (Figure 37, black line). In the corresponding absorption spectra a new isosbestic point at 441 nm was observed in the evolution of the aggregate suggesting equilibrium between the discrete aggregate and the larger superstructure architecture.

(71) Pescitelli, G.; Gabriel, S.; Wang, Y.; Fleisschhauer, J.; Woody, R. W.; Berova, N. *J. Am. Chem. Soc.* **2003**, *125*, 7613-7628.
(72) Funatsu, K.; Imamura, T.; Ichimura, A.; Sasaki, Y. *Inorg. Chem.* **1998**, *37*, 1798-1804.
(73) Korevaar, P. A.; George, S. J.; Markvoort, A. J.; Smulders, M. M. J.; Hilbers, P. A. J.; Schenning, A. P. H. J.; de Greef, T. F. A.; Meijer, E. W. *Nature* **2012**, *481*, 492-496.
(74) Mes, T.; Smulders, M. M. J.; Palmans, A. R. A.; Meijer, E. W. *Macromolecules* **2010**, *43*, 1981-1991.

Figure 37. Variable temperature CD spectra and corresponding absorption signals from CD spectrometer for compound Zn-(*R,R,R*)-**1** in methylcyclohexane/3% $CHCl_3$ (5 μM).

The evolution of the cyclic tetramer structure to a larger aggregate with decreasing temperature was clearly evidenced in the plots of band evolution versus temperature (Figure 38). The band at 438 nm in the CD spectra and 431.5 nm in the corresponding absorption spectra that are assigned to the cyclic tetramer reach a maximum at around 300.5 K and then an abrupt decay of these bands was appreciated, while 451 nm a band starts to increase below this critical temperature, suggesting that the cyclic tetramer evolves to a larger superstructure at lower temperatures, as was corroborated by the presence of an isosbestic point at 441 nm.[75]

(75) Korevaar, P. A.; Schaefer, C.; de Greef, T. F. A.; Meijer, E. W. *J. Am. Chem. Soc.* **2012**, *134*, 13482-13491.

Figure 38. Evolution of the aggregate versus temperature in CD and UV-Visible absorption bands for Zn-(*R,R,R*)-**1** in methylcyclohexane/3% $CHCl_3$.

For compound Zn-(*R,R*)-**2** the evolution from monomer specie to an aggregate did not pass through for a tetramer intermediate or at least the formation of the discrete structure was not evident when the aggregation was followed by CD or UV-Visible absorption spectroscopy (Figure 39).[58] Two very intense non-symmetrical positive bisignate CD signals were observed, one with positive maxima at 421 nm and the other one corresponding to a supramolecular arrangement at higher wavelength with negative maxima at 448.5 nm. The CD spectra and corresponding UV-Visible absorption spectra of Zn-(*R,R*)-**2** were simpler than for metalloporphyrin Zn-(*R,R,R*)-**1** due to the higher symmetry for this compound. The presence of two pyridyl groups in the 5, 15 *trans*-like positions of the porphyrinic ring could be an important factor for a regular and linear growth.

As observed in the CD spectra, three isodichoric points are present at 414.5 nm, 435 nm and 452.5 nm, meaning that two different species are in equilibrium in the working temperature and the lack of a 435 nm band in the UV-Visible absorption spectra could indicate that the both species involved in the equilibrium were the monomer metallocompound and a larger aggregate. An isosbestic point at 437 nm was appreciated in the UV-Visible absorption spectra, corroborating the assumption of the equilibrium between monomer and aggregate. The remarkable point of this spectrum is the presence of two bands at 447.5 and 452.5 nm, clearly observable at temperatures above room temperature, and as the temperature was decreased the bands started to coalesce into one. The two bands observed can be attributed to the two components in the Soret band for the aggregate, parallel transition dipoles (B_x) and perpendicular transition dipoles (B_y),[76,77] take into account that there is a perpendicular orientation between pairs of porphyrins due to the coordination by the pyridyl group to a Zinc (II) ion of the neighbour porphyrin.

(76) Aratani, N.; Kim, D.; Osuka, A. *Acc. Chem. Res.* **2009**, *42*, 1922-1934.
(77) Kasha, M.; Rawls, H. R.; El-Bayoumi, M. A. *Pure Appl. Chem.* **1965**, *11*, 371-392.

Figure 39. Variable temperature CD spectra and corresponding absorption signal from CD spectrometer of compound Zn-(*R,R*)-**2** in methylcyclohexane/3% $CHCl_3$ (5 μM).

One can observe that, even at high temperatures, a supramolecular aggregate is one of the species present in solution as noted by the high intensity in the CD spectra. This feature shows that metalloporphyrin Zn-(*R,R*)-**2** presents a greater tendency to aggregate than Zn-(*R,R,R*)-**1** and that higher temperatures are needed to have only isolated monomer species in solution.

When the evolution of the self-assembly was plotted as a function of the temperature, it was observed that bands in the CD spectra decrease gradually while temperature is increased up to 310K. Above this temperature an abrupt decay in intensity was appreciated, even though (as shown before), the aggregate still remained in solution (Figure 40).

Figure 40. Evolution of the aggregate versus temperature in CD and UV-Visible absorption bands for Zn-(*R,R*)-**2** in methylcyclohexane/3% $CHCl_3$.

The band evolution versus temperature in the corresponding UV-Visible absorption spectra clearly show the tendency of the aggregation process because it was easily comparable how the Soret band from the monomer with maxima at 417.5 nm follows the inverse tendency to the bands associated with the aggregate. While the Soret band of the isolated monomer suffered an abrupt increase in intensity when the temperature was increased above 310 K, the two bands at around 450 nm decrease (as observed in the plot of the CD band evolution versus temperature).

The results observed for metalloporphyrin Zn-(*R,R*)-**2** were comparable with the results at lower temperature for metalloporphyrin Zn-(*R,R,R*)-**1** suggesting that both metalloporphyrins follow similar self-assembly processes under those conditions.

The two metalloporphyrins presented almost identical positive Cotton effects with maxima at around 420 nm with two clear isodichoric points at 415 nm and 435.5 nm meaning that two species were involved in equilibria. The position of the band at around 450 nm indicates a multiple electronic interaction between porphyrins took place due to the formation of a larger aggregate driven and this factor explains the very considerable intensity for the dichroic signal (Figure 41). Even though, the formation of a larger aggregate for the metalloporphyrins Zn-(*R,R,R*)-**1** and Zn-(*R,R*)-**2** the CD signal at around 450 nm looks different. These different in shape and position could be related to the different environment of the whole aggregate if we take into account that this band can be associated to a secondary structure driven by hydrogen-bonding between amide groups of neighbour cyclic tetramer structures.

Figure 41. CD spectra and corresponding absorption signals from the CD spectrometer for compounds Zn-(*R,R,R*)-**1** and Zn-(*R,R*)-**2** in methylcyclohexane/3% $CHCl_3$ (5 μM) in the range of temperature 263 to 298 K.

The behavior in solution of compound Zn-(*R,R*)-**3** was completely different to either compound Zn-(*R,R,R*)-**1** or Zn-(*R,R*)-**2**. The difference with compound Zn-(*R,R*)-**2** is particularly striking, because both of them with two chiral amide groups and two pyridyl substituents in the periphery of metalloporphyrins. This contrasting behavior indicates the importance of the position of the groups on the porphyrin ring.

The CD spectra of compound Zn-(*R,R*)-**3** (Figure 42) showed two bisignate signals of relatively low intensity (compared with highly aggregated state), that were similar to those of compound Zn-(*R,R,R*)-**1** when measured at a temperature above 300.5 K. This feature could be an indication that for this compound the main aggregate form in all range of temperatures is the cyclic tetramer and there is no subsequent aggregation through secondary interactions between tetramers.

In the corresponding UV-Visible absorption spectra only a broad band at 434.5 nm was observed, attributing this band to a discrete aggregate, moreover, the broadness of the band helps to corroborate the formation of a cyclic aggregate seem also in the case of Zn-(*R,R,R*)-**1**.[72]

Figure 42. Variable temperature CD spectra and corresponding absorption signal from CD spectrometer of compound Zn-(*R,R*)-**3** in methylcyclohexane/3% $CHCl_3$ (5 μM).

Figure 43 shows the evolution of the bands either in CD spectra (left) or the corresponding absorption signal from the CD spectrometer (right) for metalloporphyrin Zn-(*R,R*)-**3**. The bands in the CD spectra decrease as temperature is increased, but did not show a clear trend, possibly because of the low intensity of the signal. Otherwise, the evolution of the absorption bands really showed the stability of the aggregate over a large range of temperatures. Up to 310 K the aggregate was very present, but above that the aggregate rapidly disappeared giving way to the increasing of monomeric specie in solution.

Figure 43. Evolution of the aggregate versus temperature in CD and UV-Visible absorption bands for Zn-(*R,R*)-**3** in methylcyclohexane/3% $CHCl_3$.

As mentioned before, observing the UV-Visible absorption spectra and CD spectra of metalloporphyrin Zn-(*R,R,R*)-**1**, it is apparent show two different self-assembly process occur depending of the range of temperature. A lower temperatures Zn-(*R,R,R*)-**1** behaves in a similar way to the 5, 15 porphyrin Zn-(*R,R*)-**2**, showing a really intense CD signal and the presence of a band at around 450.0 nm suggested the formation of a larger aggregate involving *J*-type stacking. On the other hand, as the temperature increased the dichroic signal decreased significantly and a band at 435.5 nm was observed in the absorption spectra instead of the band at 450 nm corresponding to the larger aggregate.

When the CD spectra at temperatures from 300.5 K to 338 K of metalloporphyrin Zn-(*R,R,R*)-**1** were compared with the spectra at low temperatures of Zn-(*R,R*)-**3**, clearly the two compounds self-assemble following a similar aggregating process because the positions of the Cotton effects are at almost coincident positions (Figure 44).

Surprisingly, even the both metalloporphyrins Zn-(*R,R,R*)-**1** and Zn-(*R,R*)-**3** possess the same point chirality in the monomeric structure, the superstructures that are formed show opposite orientation of the chromophores (different helicity) as appreciated in the sense of the CD signals. While Zn-(*R,R,R*)-**1** showed two clear negative bisignate signals, Zn-(*R,R*)-**3** presented two positive Cotton effect. Whereas porphyrin Zn-(*R,R,R*)-**1** has in it structure only one axial ligand that force an unidirectional coupling in the self-assembly, metallocompound Zn-(*R,R*)-**3** has two pyridyl groups that potentially can drive the aggregation.

Figure 44. CD spectra and corresponding absorption signal from CD spectrometer of compound Zn-(*R,R,R*)-**1** at temperatures between 300.5 and 338 K and Zn-(*R,R*)-**3** at temperatures from 263 and 298 K in methylcyclohexane (5 μM).

The fact that metallocompound Zn-(*R,R*)-**3** contain in its structure two amide and two pyridyl groups in *cis*-like position might be possible that the cyclic aggregate was construct by the coordination of pyridyl group in 15 or even by the one at 20 *meso* position giving in both cases the same tetramer aggregate but with slightly different orientation (Figure 45). As a result of the coexistence in solution of the two possible tetramers, the resultant optical activity present an inverse signal compare with metalloporphyrin Zn-(*R,R,R*)-**1**.

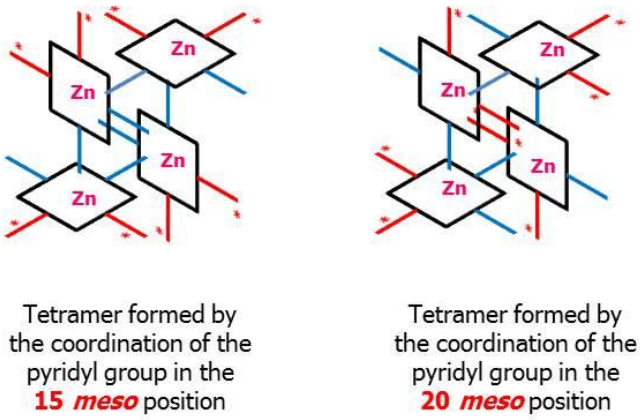

Figure 45. Schematic representation of the tetramer structure of metalloporphyrin Zn-(*R,R*)-**3** formed by the coordination of the pyridyl group in the 15 *meso* position and 20 *meso* position.

CD spectroscopy is based on the difference between the absorption of right and left circularly polarized light because of relative orientation of chromophores. The CD spectra for metalloporphyrin Zn-(*R,R*)-**3** therefore suggest an approximately opposite twisted of the porphyrin moieties in the tetramer aggregate when compared with Zn-(*R,R,R*)-**1**. This theory also explains why the intensity of the signal is so low compared with porphyrin Zn-(*R,R*)-**2**, that even though they form a different aggregate both chromophores contain two chiral groups in their structure. In Zn-(*R,R*)-**2** the tetramer structure does not allow or does arrangement of the porphyrins, while in Zn-(*R,R*)-**3** the aggregate does.

In spite of the similar UV-Visible absorption spectra compared with compound Zn-(*R,R*)-**2** where a Soret band related to a *J*-aggregate at around 450 nm was observed, the temperature dependent CD spectra of metalloporphyrin Zn-(*R*)-**4** in methylcyclohexane/3% $CHCl_3$ showed completely different optical activity compared with metalloporphyrins derivatives of this family (Figure 46).

Figure 46. Variable temperature CD spectra and corresponding absorption signal from CD spectrometer of compound Zn-(*R*)-**4** in methylcyclohexane/3% $CHCl_3$ (5 μM).

The CD spectra are totally different, but we have to keep in mind that this technique is sensitive to the conformation of chromophores and the appearance of the CD reflects the environment of the molecules.[57] Thus, although aggregation obviously takes place, there is no significant transfer of chirality from the stereogenic center to the porphyrin arrangement, presumably because of the lack of an important role of the amide in the assembly.

After all, Zn-(*R*)-**4** presented in the CD spectra and two isodichroic points at 432 nm and 452 nm indicating equilibria between monomer and aggregate species in the range of working temperatures. Furthermore, a negative broad band at around 475.0 nm was appreciated in the spectra.

From the corresponding absorption spectra could not extracted any relevant information due to the low intensity of the signal that become surrounded by the noisy of the equipment. This low intensity in the HT spectra as well as the distinct spectra observed in the CD spectra might be

caused by the precipitation of the metalloporphyrin during the measurements because the low solubility of that compound.

The plot of the evolution of the bands in the CD spectra and UV-Visible absorption spectra versus temperature for metalloporphyrin Zn-(*R*)-**4** show a progressive decay in intensity in the bands associated to an aggregate in the absorption spectra and the enhancement of the intensity of the Soret band of the monomer metalloporphyrin while temperatures increase (Figure 47).

Figure 47. Evolution of the aggregate versus temperature in CD and UV-Visible absorption bands for Zn-(*R*)-**4**.

The results observed in the temperature-dependent studies of metalloporphyrins clearly demonstrate the importance of the position and number of pyridyl groups and chiral amide moieties in the periphery of the macrocycle, even though the exact hierarchy of the self-assembly is enigmatic for some of the samples. In the case of metalloporphyrin Zn-(*R,R,R*)-**1** two different regimes could be distinguished. At temperatures above room temperature a tetramer structure is formed and an elongation process took place at low temperatures.[78,79,80] Even though for the rest of zinc (II) porphyrins the evolution and process of the aggregation was not as clear as for metalloporphyrin Zn-(*R,R,R*)-**1**, we could suggest a linear growth for metalloporphyrins Zn-(*R,R*)-**2** and Zn-(*R*)-**4** according to the CD and UV-Visible absorption spectra. On the other hand, the results for Zn-(*R,R*)-**3** lead us to think the cyclization of the aggregate to give an isolated tetramer due to the conformation of the Zn (II) porphyrin.

(78) Smulders, M. M. J.; Schenning, A. P. H. J.; Meijer, E. W. *J. Am. Chem. Soc.* **2008**, *130*, 606-611.
(79) Zhao, D.; Moore, J. S. *Org. Biomol. Chem.* **2003**, *1*, 3471-3491.
(80) Jonkheijm, P.; Van der Schoot, P.; Schenning, A. P. H. J.; Meijer, E. W. *Science*, **2006**, *313*, 80-83.

2.6. Self-assembly mechanism for metalloporphyrins.

2.6.1. Comparison of isodesmic and cooperative self-assembly models.

Mathematical models for the CD curves versus temperature for these metalloporphyrins were applied in order to determine the self-assembly process that took place in each Zn (II) porphyrin. Two different models have to be kept in mind to associate the self-assembly process with a certain mechanism. Cooperative process can be distinguished by two different regimes. The formation of a nuclei with critical size which acts as an activation step followed by a favorable elongation process. On the other hand, the isodesmic model is governed by a gradual increase in the number of aggregate species where each energy of attachment is the same as the prior and posterior one (Figure 48).[81,82,83]

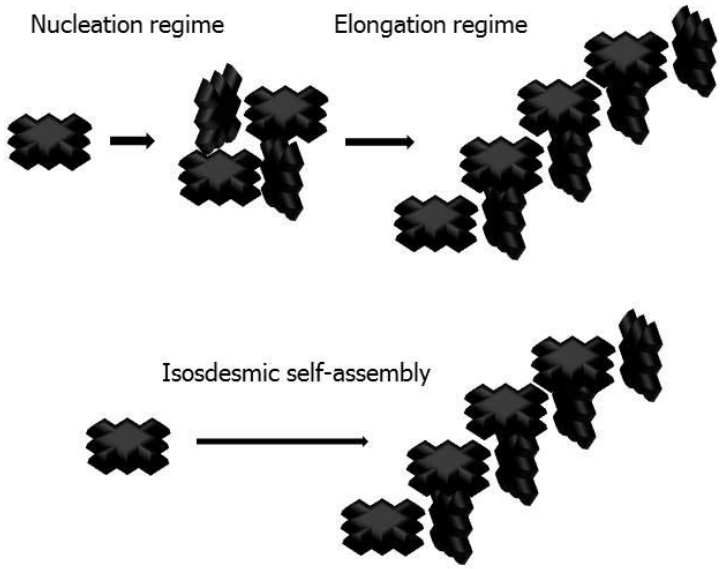

Figure 48. Schematic representation of the two disparate self-assembly mechanisms.

Isodesmic self-assembly was described by the formation of linear polymers where each step was governed by an equilibrium constant that was equal in all the self-assemble process following a sigmoidal growth. On the contrary, cooperative process or growth model self-assembly that in fact is slightly different compare with the non-cooperative self-assembly process was governed by an initial equilibrium constant in the so called nucleation regime, follow by the elongation regime

(81) Smulders, M. M. J.; Nieuwenhuizen, M. M. L.; de Greef, T. F. A.; Van der Schoot, P.; Schenning, A. P. H. J.; Meijer, E. W. *Chem Eur. J.* **2010**, *16*, 362-367.
(82) Oosawa, F.; Kasai, M. *J. Mol. Biol.* **1962**, *4*, 10-21.
(83) Martin, R. B. *Chem. Rev.* **1996**, *96*, 3043-3064.

with an exponential enhancement of the aggregation degree governed by a unique equilibrium constant as it was in the isodesmic process.

The evolution in the observed CD spectra versus temperature for the different metalloporphyrins, show that different self-assembly processes take place depending of the constitution of the aromatic ring that was directly related with the kind of aggregate formed.

2.6.2. Mathematical representation of isodesmic and cooperative mechanism.

The fitting of the curves with one or other assembly model help us to understand the mechanism in the aggregation of the metallocompounds studied here as well as provide thermodynamic parameters such as the molar enthalpy release in the formation of non-covalent interaction and the temperature-dependent association constant that describes the self-assembly process.

Equation 1 describes how the fraction of aggregated molecules (Φ) varies with temperature in an isodesmic mechanism. Parameters Φ_0 and Φ_{sat} are introduced in the equation to ensure that the relation $\Phi/\ \Phi_{sat}$ does not exceed unity, ΔH_m is the enthalpy release in the aggregation process by non-covalent interactions, T_m is the temperature which Φ is equal to 0.5 and R is the gas constant.

$$\Phi = \Phi_0 + \left[\frac{\Phi_{sat}}{1 + exp[-0.908\Delta H_m(T - T_m/RT_m^2)]}\right]$$

Equation 1. Isodesmic self-assembly model.

When the fraction of aggregated molecules (Φ) is introduced in equation 2, the equilibrium constant K_e and the number of stacked molecules (DP_N) can be calculated for the whole range of temperatures. Whereas ΔH_m has a unique value in all the process, the equilibrium constant K_e is dependent to the changing temperatures and where C_0 is the initial concentration of the monomer in solution.

$$DP_N = \frac{1}{\sqrt{1 - \Phi(T)}} = \frac{1}{2} + \frac{1}{2}\sqrt{4K_e(T)C_0 + 1}$$

Equation 2. Number of stacked molecules.

Therefore, the entropy (ΔS) can be calculated from ΔH_m and K_e applying the Van't Hoff equation (Equation 3).

$$\ln K_e = \frac{\Delta S}{R} - \frac{\Delta H_m}{RT}$$

Equation 3. Van't Hoff equation.

As for the isodesmic model, from the data points in the CD spectra of each metalloporphyrin the degree of aggregation in the cooperative self-assembly process can be desribed by equation 4.

$$\Phi = \Phi_{sat}\left[1 - exp\left[\frac{h_e}{RT_e^2}(T - T_e)\right]\right]$$

Equation 4. Cooperative self-assembly model in the elongation regime.

Slightly changes are introduced in the cooperative mathematical model compared with the isodesmic equation taking into account that nucleation-elongation model is a modification of the isodesmic model. In order to not exceed unity value of $\Phi/\ \Phi_{sat}$, Φ_{sat} is introduced in the equation. T_e is the temperature that the aggregate starts to elongate, h_e the enthalpy release in the formation of non-covalent interactions in the elongation process and R is the gas constant.

Moreover, the active state of the self-assembly process is governed by the equilibrium constant in the elongation regime (K_e) that can be described through equation 5.

$$K_e = exp\left[\frac{-h_e}{RT_e^2}(T - T_e)\right]$$

Equation 5. Dimensionless equilibrium constant in the elongation regime.

Up to the elongation temperature, the self-assembly process is in the nucleation regime, where a small aggregate acts as a nuclei initiator with an association constant (K_a) that can be described by the following equation 6.

$$\Phi = \sqrt[3]{K_a}exp\left[\left(\frac{2}{3\sqrt[3]{K_a}} - 1\right)\frac{h_e}{RT_m^2}(T - T_e)\right]$$

Equation 6. Cooperative self-assembly model in the nucleation regime.

2.6.3. Assignment of the self-assembly mechanism for the metalloporphyrins.

According to the evolution in UV-Visible absorption spectra and CD measurements, only metalloporphyrin Zn-(*R,R,R*)-**1** followed two distinct states of aggregation that could be attributed to a nucleation process at higher temperatures and then evolve to an elongation process of the aggregate.

When the CD spectra of Zn-(*R,R,R*)-**1** at temperatures above 300.5 K were compared with the spectra of Zn-(*R,R*)-**3** clear similarities were observed in their self-assembly, suggesting a discrete tetramer like aggregate, while at lower temperatures, in the elongation regime, metalloporphyrin Zn-(*R,R,R*)-**1** matched perfectly with Zn-(*R,R*)-**2** behavior self-assembly.

Before applying any of the mathematical models, the CD data has to be normalized in order to obtain the degree of aggregation, that is the highest intensity is defined as $\Phi=1$ (at the lowest temperature) and $\Phi=0$ at the highest working temperature.

Analyzing the data points of Zn-(*R,R,R*)-**1** from the band at 451.0 nm in the CD spectra, it was clearly observed that at temperatures above 300.5 K the formation of a tetramer aggregate followed a sigmoidal shape as a function of temperature which is an indication of isodesmic self-assembly. This tetramer acts as nucleation structure for the following elongation regime. When the temperature is below 300.5 K the tetramer aggregate evolves to a larger superstructure following a cooperative process as the non-sigmoidal feature for the curve indicates, with a rapid increase in CD intensity from 300 to 280 K (Figure 49).

At higher temperatures metalloporphyrin Zn-(*R,R,R*)-**1** followed an isodesmic mechanism instead of the cooperative model that is showed at lower temperatures as suggested the abrupt decay in the degree of aggregation above 285 K.

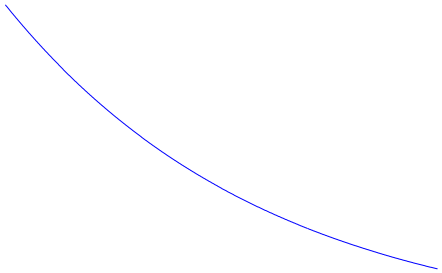

Figure 49. Degree of aggregation for Zn-(*R,R,R*)-**1** versus temperature. Isodesmic model (red line) and cooperative model (blue line).

This behavior suggested that the cyclic tetramer structure formed at higher temperatures evolves to a larger aggregate as the temperature decreases, these aggregates were not formed in the unfavorable regime as the nucleation-elongation model happened. The results also were corroborated by the thermodynamics parameters found in the formation of this discrete supramolecular stack (Table 1).

Isodesmic model				
λ (nm)	Φ_{sat}	$\pm\Phi_0$	T_m (K)	$-\Delta H_m$ (kJ/mol)
451.0	1.08	0.04	311.7	9.3

Table 1. Thermodynamic parameters for the isodesmic self-assembly model at high temperature where the tetramer is form for metalloporphyrin Zn-(*R,R,R*)-**1**.

The value of the enthalpy released during the isodesmic self-assembly process ΔH_m=-9.3 kJ/mol is in agreement with values found in literature by cyclic tetramer metalloporphyrins driven by coordination of pyridyl unit with the zinc (II) ion.[24] This value can be explained by the energy release in the cyclization of the structure. Nevertheless, the rather small value for the ΔH_m could suggest that this process is dominated by entropic effects.

Table 2 shows the equilibrium constant ($K_e \sim 10^5$ M^{-1}) dependence with temperature during the self-assembly process, obtaining values consistent with an isodesmic process that also are in accordance with an association constant between pyridyl ligand to a zinc (II) porphyrin.[84]

Isodesmic model			
T (K)	K_e (10^5 M^{-1})	DP_N	ΔS (J/K·mol)
303.0	36.6	4.3	95.0
305.5	13.0	2.7	86.7
308.0	7.2	2.0	82.0
313.0	2.4	1.3	73.3
318.0	1.3	1.1	68.4
323.0	1.0	1.0	67.0
328.0	0.9	1.0	66.9
333.0	0.9	1.0	67.2
338.0	0.9	1.0	67.7

Table 2. Thermodynamic parameters calculated for the isodesmic self-assembly model at high temperature where the tetramer is form for metalloporphyrin Zn-(*R,R,R*)-**1**.

It is important to stand out the values obtained for the number of stacked molecules, which were clearly in agreement with the formation of a tetrameric structure, having four monomeric

(84) Vogel, G. C.; Stahlbush, J. R. *Inorg. Chem.* **1977**, *16*, 950-953.

porphyrins involved in the formation of the aggregate when temperature was close to the transition temperature.

Table 3 shows the thermodynamic parameters obtained when the normalized CD data points were fit in the elongation regime for metalloporphyrin Zn-(*R,R,R*)-**1**.

Cooperative model			
λ (nm)	Φ_{sat}	T_e (K)	- h_e (kJ/mol)
451.0	1.03	299.2	87.5

Table 3. Thermodynamic parameters for cooperative self-assembly model for the elongation of the chains in the low temperature regime for metalloporphyrin Zn-(*R,R,R*)-**1**.

Comparing the thermodynamic parameters of the two self-assembly mechanisms, we can observe that the enthalpy release in the elongation process is much higher than in the isodesmic process. This value is similar to that in other systems, indicating a high degree of cooperativity.[85]

When the normalized CD data points for compound Zn-(*R,R*)-**2** were analyzed, a perfect fit with an elongation process was obtained. As explained previously, even at high temperatures a *J*-aggregate was present in solution, as witnessed by the high intense value for CD signal, indicating the great tendency to aggregate of this metallocompound with the two amides and two pyridyl groups in 5,15 position (

Figure ***50***).

(85) Helmich, F.; Lee, C. C.; Nieuwenhuizen, M. M. L.; Gielen, J. C.; Christianen, P. C. M.; Larsen, A.; Fytas, G.; Leclère, P. E. L. G.; Schenning, A. P. H. J.; Meijer, E. W. *Angew. Chem. Int. Ed.* **2010**, *49*, 3939-3942.

Figure 50. Degree of aggregation for Zn-(*R,R*)-**2** versus temperature (filledsquares). The line is a fit to a cooperative self-assembly mechanism.

Table 4 shows the thermodynamic parameters obtained when the normalized CD data points at 448.5 nm were fitted in the elongation regime.

Cooperative model			
λ (nm)	Φ_{sat}	T_e (K)	- h_e (kJ/mol)
448.5	0.95	338.6	57.7

Table 4. Thermodynamic parameters for cooperative self-assembly model of metalloporphyrin Zn-(*R,R*)-**2**.

The enthalpy release h_e=-57.7 kJ/mol in the self-assembly process by non-covalent interactions in the growth of the aggregate was in the range of values reported to the literature. However, the value is considerably smaller compared with the value obtained for metalloporphyrin Zn-(*R,R,R*)-**1**. The smaller value of the enthalpy release in the self-assembly process for metalloporphyrin Zn-(*R,R*)-**2** can be explained by the larger value of the elongation temperature (T_e) as well as by the less amide groups in the porphyrin ring, the fact that decrease the number of hydrogen-bonds in the whole structure.

The temperature dependent studies in CD and UV-Vis absorption spectroscopy for Zn-(*R,R*)-**3** showed a unique process of self-assembly. Whereas Zn-(*R,R*)-**2** evolved to linear aggregate, Zn-(*R,R*)-**3** evolved to cyclic discrete tetramer as the band at 431.5 nm indicated. Analyzing the CD data points at 441.0 nm for compound Zn-(*R,R*)-**3** clearly showed a sigmoidal curve with temperature according to an isodesmic process take place in its self-assembly (Figure 51).

Figure 51. Degree of aggregation for Zn-(*R,R*)-**3** versus temperature (filledsquares). The curve is a fit to an isodesmic self-assembly mechanism.

The self-assembly mechanism for this porphyrin following an isodesmic process is in complete agreement with the results observed before, when CD spectra of metalloporphyrin Zn-(*R,R,R*)-**1** at temperatures above 300.5 K was compared with the CD evolution of Zn-(*R,R*)-**3**.

The thermodynamic parameters extracted from equation 2 are shown in table 5.

Isodesmic model				
λ (nm)	Φ_{sat}	$\pm\Phi_0$	T_m (K)	$-\Delta H_m$ (kJ/mol)
441.0	1.01	0.09	312.7	5.4

Table 5. Thermodynamic parameters for the isodesmic self-assembly model of metalloporphyrin Zn-(*R,R*)-**3**.

As observed for metalloporphyrin Zn-(*R,R,R*)-**1** in the isodesmic regime, a small enthalpy value was obtained in the formation of the discrete cyclic aggregate, a process that is most probably driven by entropic effects. Furthermore, the melting temperature obtained $\mathrm{Tm}=312.7\ \mathrm{K}$ in the process is coincident with the melting temperature obtained by porphyrin Zn-(*R,R,R*)-**1**.

The values of the equilibrium constant ($K_e \sim 10^5\ M^{-1}$), as happened with the value of the enthalpy release in the non-covalent interaction in the self-assembly process, are in concordance with an isodesmic process. The average number for the aggregated stack did not achieve four molecules as the cyclic tetramer needed, even though, it could be assumed that this discrete aggregated was form in the self-assembly process (table 6).

Isodesmic model		
T (K)	K_e (10^5 M^{-1})	DP_N
288	18.5	3.1
293	14.2	2.8
298	11.0	2.5
303	6.7	2.0
308	3.6	1.5
310.5	3.1	1.4
313	2.3	1.3
315.5	1.9	1.2
318	1.6	1.1
320.5	1.3	1.1
323	1.1	1.0
325.5	1.0	1.0
328	1.0	1.0
330.5	1.0	1.0
333	0.9	1.0
338	0.8	1.0

Table 6. Thermodynamic parameters for the isodesmic self-assembly model of metalloporphyrin Zn-(R,R)-3.

The lack of data points in the CD spectra for compound Zn-(*R*)-**4** made the assignment of a concrete model difficult. Even though, the data fitting for this Zn (II) porphyrin indicated a linear growth behavior in the self-assembly in the range of working temperature (Figure 52).

Figure 52. Degree of aggregation for Zn-(*R*)-**4** versus temperature (filledsquares). The curve is a fit to a cooperative self-assembly mechanism.

The value of the enthalpy (h_e=-28.9 kJ/mol) found by the self-assembly of metalloporphyrin Zn-(*R*)-**4** is relative small, take into account that for an elongation process the enthalpy is larger in absolute value ($h_e \geq$-60 kJ/mol) .

Cooperative model			
λ (nm)	**Φ_{sat}**	**T_e (K)**	**- h_e (kJ/mol)**
438.0	1.14	337.9	28.9

Table 7. Thermodynamic parameters for cooperative self-assembly model of metalloporphyrin Zn-(*R*)-**4**.

The small value for this process could be explained by the involving of hydrogen-bonds in the self-assembly.

Even though the aggregation is driven by the coordination of pyridyl group with the zinc (II) metal ion of another porphyrin, hydrogen-bonds between the amide groups also could play a role in the formation of a larger aggregate, which is why the enthalpy found for metalloporphyrin Zn-(*R,R,R*)-**1** is larger than the enthalpy for Zn-(*R,R*)-**2** and for Zn-(*R*)-**4** the value of the enthalpy becomes smaller due to the lack of amide groups in the structure.

2.7. Study of the self-assembly of metalloporphyrins on surface.

2.7.1. General aspects of atomic force microscopy (AFM).

The AFM provides structural information of non-conducting samples unreachable for by other microscopic techniques. The AFM affords images with nanometre scale resolution that is reliable in

the direction perpendicular to the surface plane, and accurate detail can be derived in the plane of the surface.[86] As Figure 53 shows, the AFM equipment is formed by a sharp tip located at the edge of a cantilever that scans the roughness of the sample in the x-y direction. A laser is reflected from the top of the cantilever to a detector photodiode that sends the information to a feedback mechanism which is responsible for maintaining one of the parameters (depending of the operation mode) constant, controlled by a z-piezoelectric.

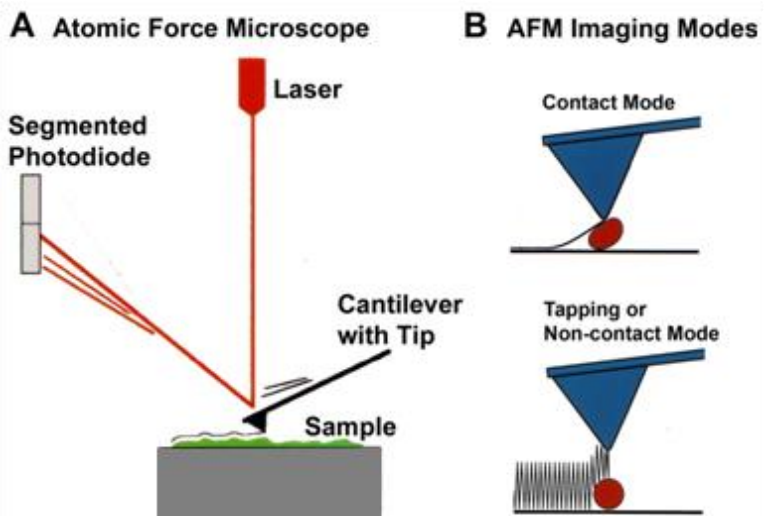

Figure 53. (A) AFM instrumentation ; (B) AFM operation modes.

The AFM can work in three main and generic operation modes : contact, tapping and non contact mode (Figure 53). Tapping mode is the ideal one to work with soft samples, in this case porphyrins, because a lower force is applied compared with contact mode and the lateral forces are suppressed avoiding the distortion of the image, moreover most of the samples present high lateral resolution. On the contrary the scan rate is lower than for the contact mode.

In tapping mode the cantilever is driven up and down near the resonance tip frequency with amplitude between 100 to 200 nm that it keeps constant during the measurement controlled by the feedback mechanism, the fact that the interactions between sample and tip keep constant too and a topographic image is generated.

2.7.2. Study of the hierarchy organization on surface by AFM.

The metalloporphyrins Zn-(*R,R,R*)-**1**, Zn-(*R,R*)-**2**, Zn-(*R,R*)-**3** and Zn-(*R*)-**4** studied in methylcyclohexane/3 % $CHCl_3$ (5 μM) solutions were deposited on a solid support by casting and the solvent was allowed to evaporate and the material was investigated with tapping mode AFM.

(86) Binning, G.; Quate, C. F.; Gerber. C. *Phys. Rev. Lett.* **1986**, *56*, 930-933.

Different external factors such as concentration or temperature can influence the self-assembly of porphyrins as was observed in solution for metalloporphyrins Zn-(*R,R,R*)-**1**, Zn-(*R,R*)-**2**, Zn-(*R,R*)-**3** and Zn-(*R*)-**4**. The temperature-dependent self-assembly suggested that the organization of the supramolecular architecture of metallocompounds on the surface also can be affected by this external factor. Moreover, other parameters can play an important role in the transfer process of the self-assemble molecules from solution to a solid support such as molecule-molecule or molecule-surface interactions. The nature of the surface is an important factor to take into account to successfully adsorb the aggregates in a controlled way.[87,88,89] The metallocompounds under observation here have a long alkyl chains in the side positions that can help the adsorption of the aggregates due to the van der Waals interaction with hydrophobic surfaces.[90]

Three drops of Zn-(*R,R,R*)-**1** methylcyclohexane/3% $CHCl_3$ 5 μM solution were drop casted onto high oriented pyrolytic graphite (HOPG) at room temperature and different areas of the surface were scanned (Figure 54). As the AFM images of the resulting material show, the entire surface was covered by different layers of metalloporphyrin after solvent evaporation. No single objects were observed under these conditions. The reason for this effect could be that different strength interactions between molecule-surface as well as molecule-molecule take place at the different levels from the graphite support the fact that we cannot determine correctly the influence of the surface over the aggregates.

(87) Jonkheijm, P.; Hoeben, F. J. M.; Kleppinger, R.; Van Herrikhuyzen, J.; Schenning, A. P. H. J.; Meijer, E. W. *J. Am. Chem. Soc.* **2003**, *125*, 15941-15949.
(88) Koepf, M.; Wytko, J. A.; Bucher, J-P.; Weiss, J. *J. Am. Chem. Soc.* **2008**, *130*, 9994-10001.
(89) Rauch, V.; Wytako, J. A.; Takahashi, M.; Kikkawa, Y.; Kanesato, M.; Weiss, J. *Org. Lett.* **2012**, *14*, 1998-2001.
(90) Iavicoli, P.; Simón-Sorbed, M.; Amabilino, D. B. *New. J. Chem.* **2009**, *33*, 358-365

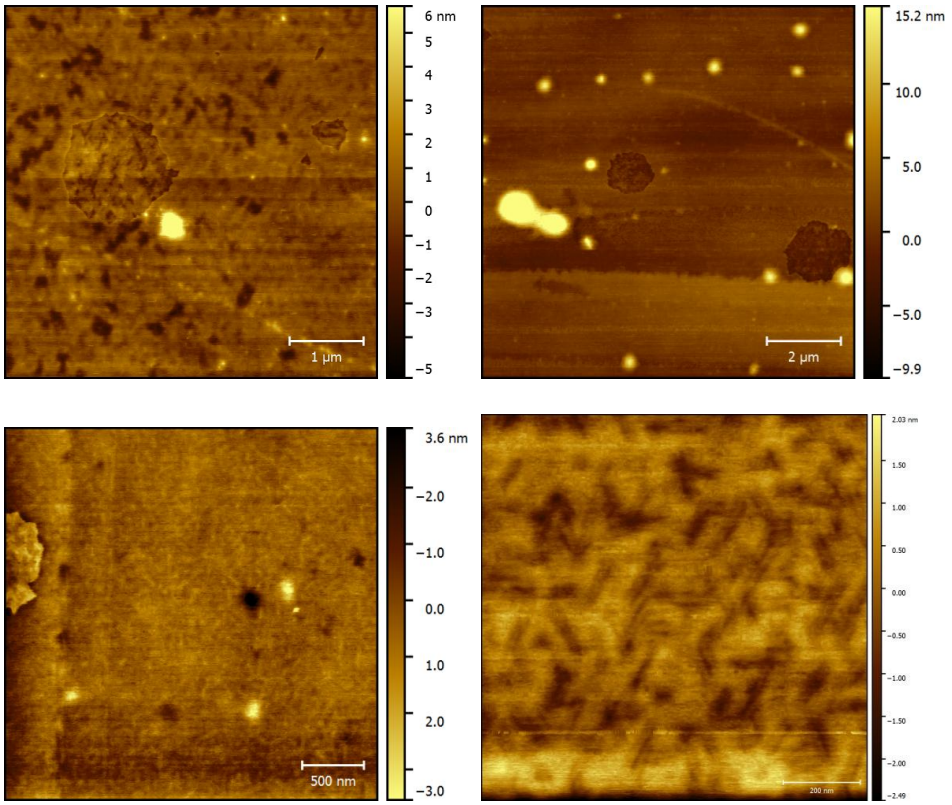

Figure 54. Tapping mode AFM images of three drops of Zn-(*R,R,R*)-**1** (5 µM) on freshly cleaved HOPG.

When three drops of metalloporphyrin Zn-(*R,R*)-**2** were drop cast on HOPG surface from a methylcyclohexane/3% $CHCl_3$ 5 µM solution at room temperature, as was observed for metalloporphyrin Zn-(*R,R,R*)-**1** different layers of compound were appreciated in the topographic images (Figure 55).

Nevertheless, a cross-linked fibrilar organization was observed in the top layer of the topographic images, suggesting that the aggregates formed in solution were transferred on the surface and the surface did not interfere in their organization because they were far from it. Furthermore, in each intersection of fibres as a nucleus point was formed maybe due to in the evaporation process of the solvent the relative concentration of the molecule is increase and a packing of the molecules were observed.

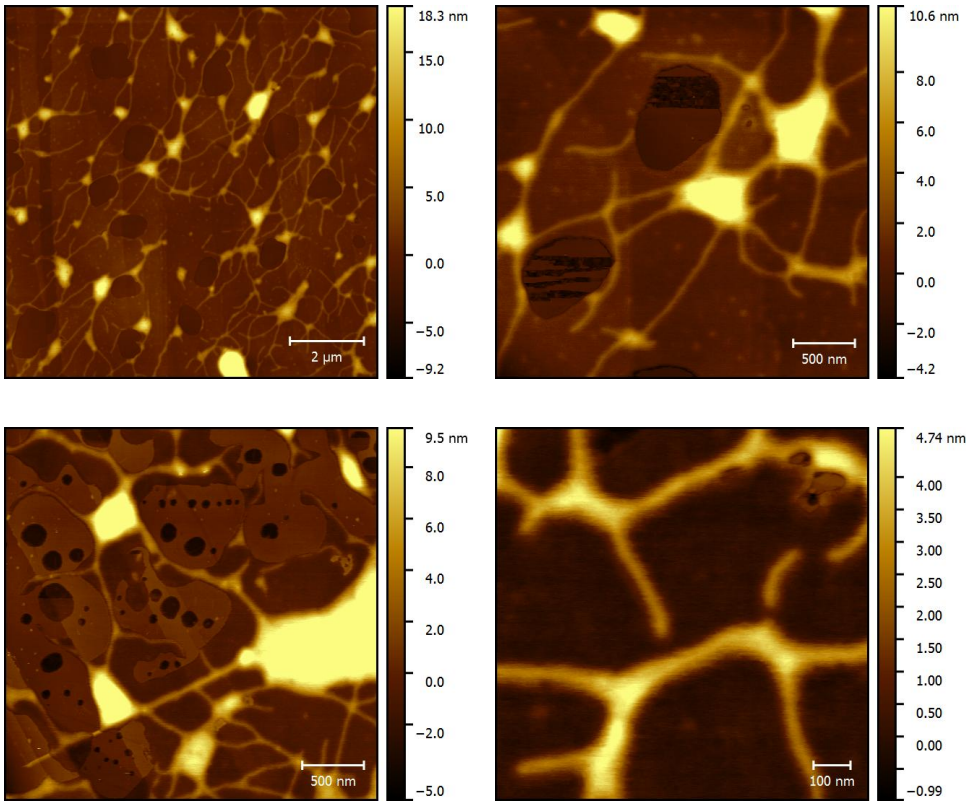

Figure 55. Tapping mode AFM images of three drops of Zn-(*R,R*)-**2** (5 µM) on freshly cleaved HOPG.

Taking into account the results observed for these two metalloporphyrins when three drops of methylcyclohexane/3% $CHCl_3$ solution were transferred to a solid support, the AFM analysis were repeated casting only one drop of metalloporphyrin solutions on the surface and allowing the solvent evaporate to ensure the observation of single objects.

Topographic images of Zn-(*R,R,R*)-**1** showed a distinct organization at different regions of the HOPG surface (Figure 56). Images (a) and (b) show non-organized molecules on the surface due to the dewetting process, while in topographic image (c) a well distributed spherical particles were observed. These results might suggest that, at room temperature, as observed in the solution studies, equilibria between monomeric specie and cyclic tetramer aggregate took place, being the isolated metalloporphyrin responsible for the non-organized molecules on the surface. The concentration of the material is also high in this area that might lead to non-specific aggregation. Image (c) corresponds to the tetramer aggregates, suggesting that molecule-molecule interactions are stronger than molecule-surface. Moreover, in image (c) the graphite steps are observed, indicating that there is not any layer bellow the particles.

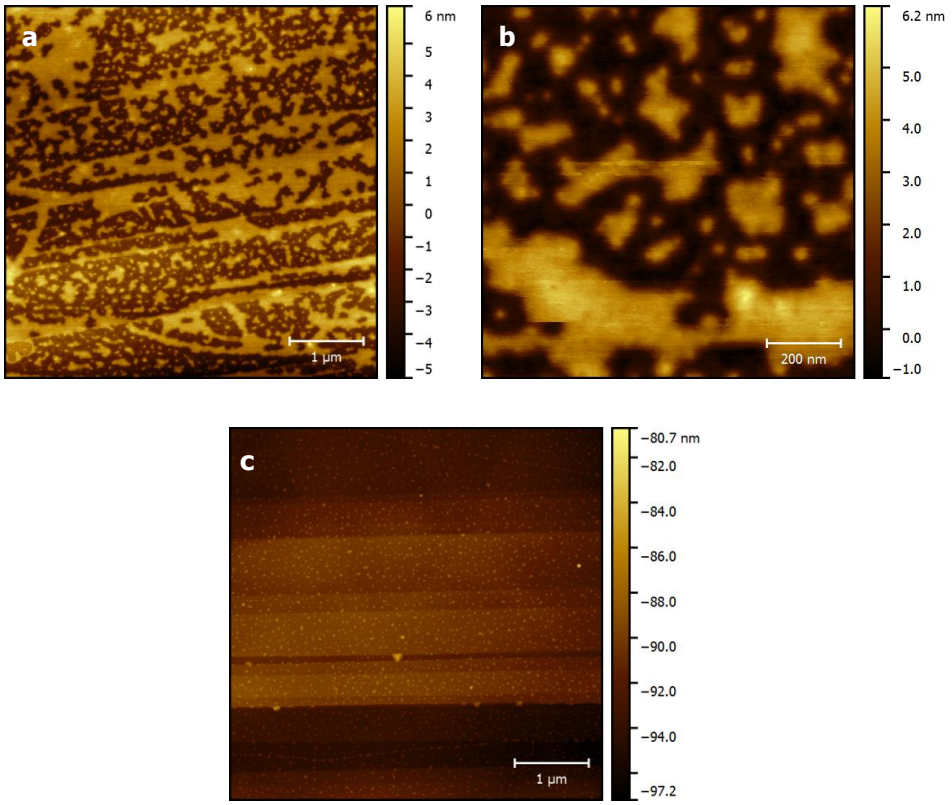

Figure 56. Tapping mode AFM images of one drop of Zn-(*R*,*R*,*R*)-**1** (5 µM) on freshly cleaved HOPG.

The measured heights of the disc figures were found to be around 2.5nm as the topographic profile showed, that could correspond to a standing up porphyrin coordinated through pyridyl group with a flat porphyrin on the surface (Figure 57).

As mentioned above, the long alkyl chains in the side positions of the porphyrin ring stabilize the structure through van der Waals interactions with the graphite support, allowing one molecule to be almost flat on the surface.

These results were in agreement with the observation in solution where tetrameric structures were formed up to 300.5 K for this compound.

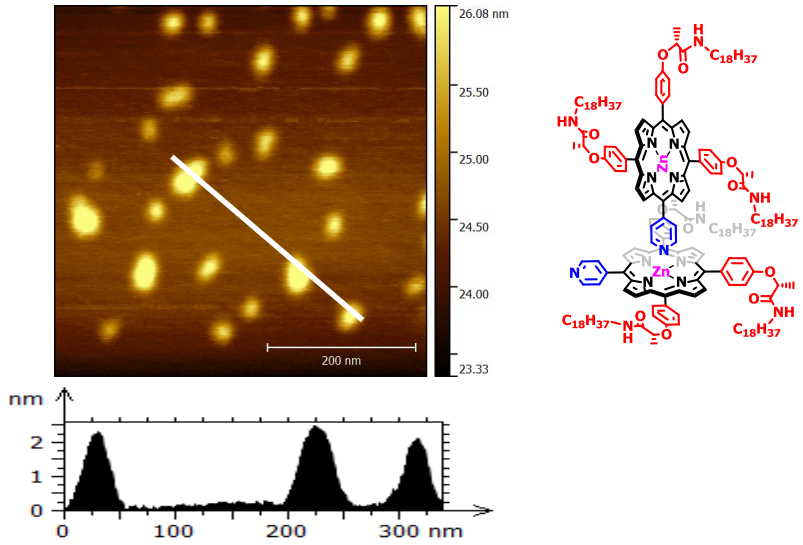

Figure 57. Tapping mode AFM images of cast Zn-(*R,R,R*)-**1** on freshly cleaved HOPG.

Figure 58 shows a statistic study of the dimensions of the globular stacks of metalloporphyrin Zn-(*R,R,R*)-**1** on graphite where one can appreciate that most of the particles present diameter between 20 to 30 nm (from 100 particles). This behaviour could be attributed to different numbers of tetramers tending to be close one to each other because hydrogen-bonding between amide groups of different tetramer aggregates, but is also possibly an effect of tip convolution.

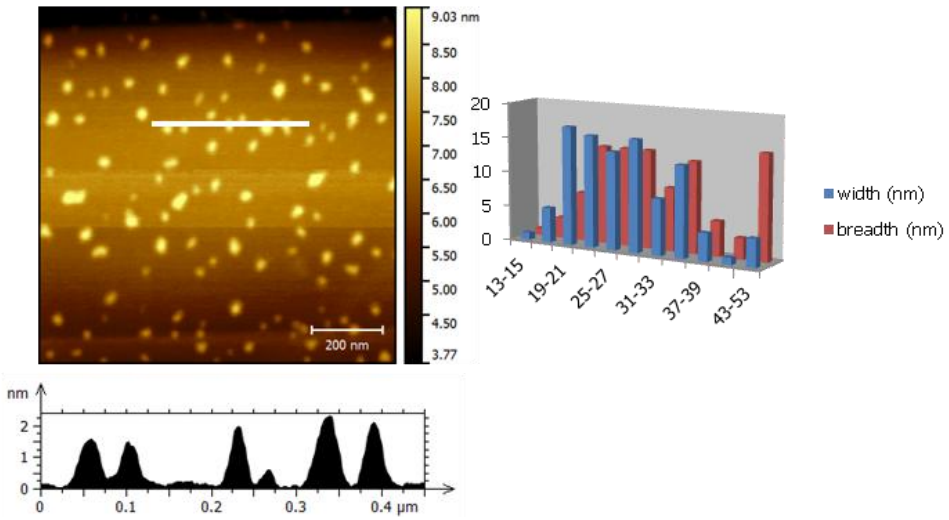

Figure 58. Tapping mode AFM images of Zn-(*R,R,R*)-**1** on freshly cleaved HOPG and statistical graph of particle dimensions.

However, in a soft tapping mode the height of the structures is more accurate measure than the diameter size of the objects.

In order to corroborate that aggregates formed in solution were deposited to the surface suffering a minimum effect of the adsorption, the metalloporphyrin solution in methylcyclohexane/3% $CHCl_3$ was cold down at 0ºC and then drop-casted onto graphite because at this temperature the tetramer aggregate was evolved to a secondary structure driven by hydrogen-bonding (Figure 59).

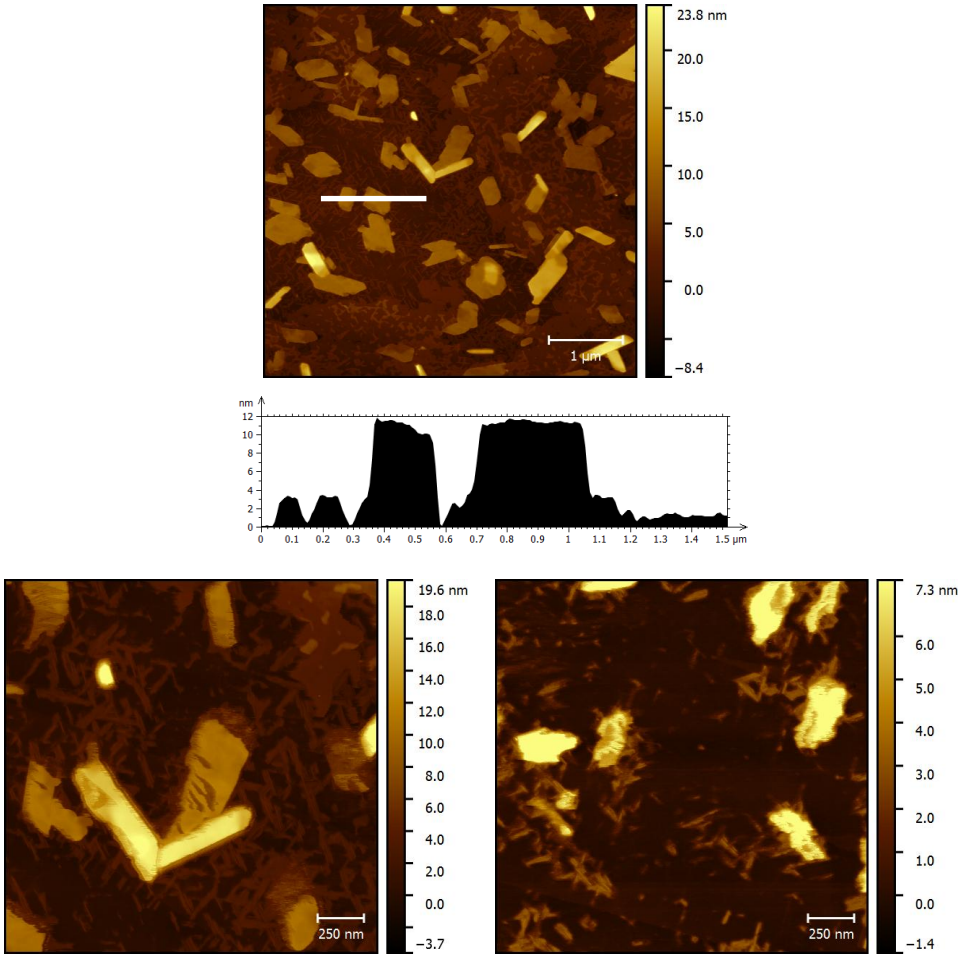

Figure 59. Tapping mode AFM images of Zn-(*R*,*R*,*R*)-**1** on freshly cleaved HOPG at 0ºC.

The topographic images show two different structures present in the surface. In one hand, needle like structures 3 nm thick and approximately 60-200 nm in length, suggesting that at this temperature stronger interactions between molecules were present. On the other hand, planar blocks as nanosheet structures were present on the surface with a height of around 12 nm were

apparent in the profile. The formation of these planar structures could be related to the folded organization of the superstructures due to the low working temperature.[91]

However, in another region of the surface another organization of the molecules was observed when the metalloporphyrin solution was cooled down at 0ºC and drop casted onto the surface (Figure 60).

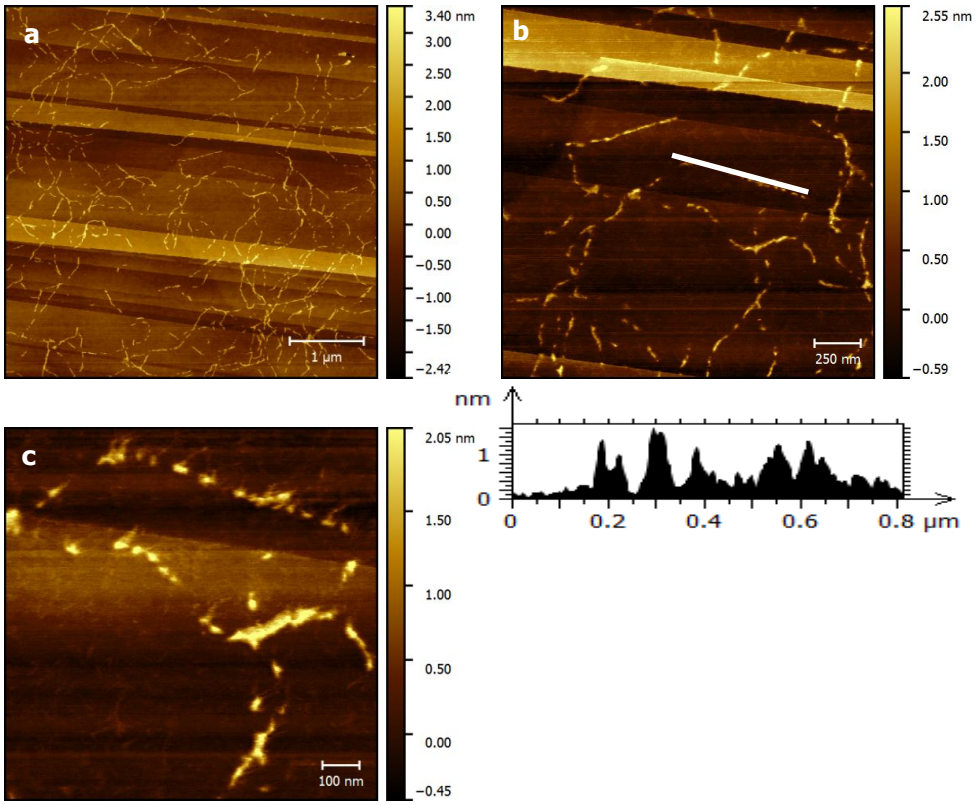

Figure 60. Tapping mode AFM images of Zn-(*R*,*R*,*R*)-**1** on freshly cleaved HOPG at 0ºC.

Topographic image (a) shows a fibrilar organization of the molecules, suggesting that as lowering the temperature of the solution, the tetrameric structure observed at room temperature has evolved to a larger aggregate and this superstructure has not been affected by the interaction with the graphite surface. The steps in the graphite do not appear to influence the structure dramatically, suggesting that the surface-molecule interaction is not too influential and the surface structure is a result of solution-formed aggregates. Despite this suggestion, close-up images were recorded, clearly showing that the fibres were not well formed. Even so, these results corroborate the fact that a secondary structure was formed at low temperatures driven by the hydrogen-bond interactions between amide groups of the cyclic tetrameric architecture. As the profile in the image

(91) Ikeda, T. *Langmuir* **2015**, *31*, 667-673.

(b) shows, the aligned spherical particles present vertical dimensions between 1.5 to 2 nm that could correspond to the porphyrin size.

Topographic images of one drop of Zn-(*R,R*)-**2** methylcyclohexane/3% $CHCl_3$ solution deposited at room temperature showed a mixture of spherical particles and a fibrilar network with heights around 3 nm and 10 nm as the profile in the image (c) shows (Figure 61).

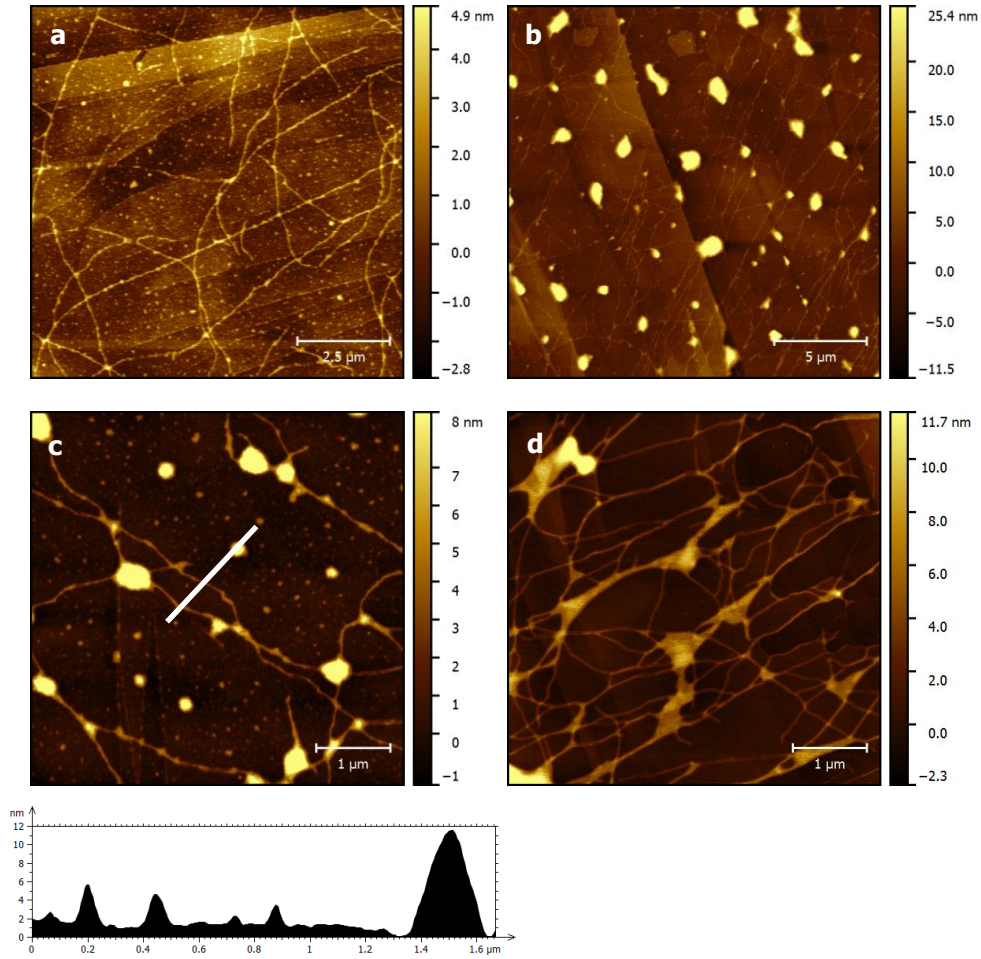

Figure 61. Tapping mode AFM images of one drop of Zn-(*R,R*)-**2** (5 µM) on freshly cleaved HOPG at room temperature.

The heights for the fibres and the small particles were in agreement with the coordination zinc (II)-pyridyl of consecutive porphyrins, as was explained in the case of porphyrin Zn-(*R,R,R*)-**1**. Moreover, topographic image (b) a bigger globular structure could be appreciated with heights between 40 and 60 nm, while image (d) only a network of fibres can be observed.

These results on the surface are a bit surprising if we bear in mind that the studies in solution for this metalloporphyrin did not show a two step self-assembly as happened with

metalloporphyrin Zn-(*R,R,R*)-**1**. However, we could attribute these results to the fact that some of the superstructures are disaggregated as a consequence of the molecule-surface interaction.

When the same solution was cooled down at 0ºC and cast onto graphite (HOPG) by drop-casting a fibre network randomly oriented was observed as a self-assemble architecture and a planar sheets underneath were appreciated in all the graphite surface (Figure 62).

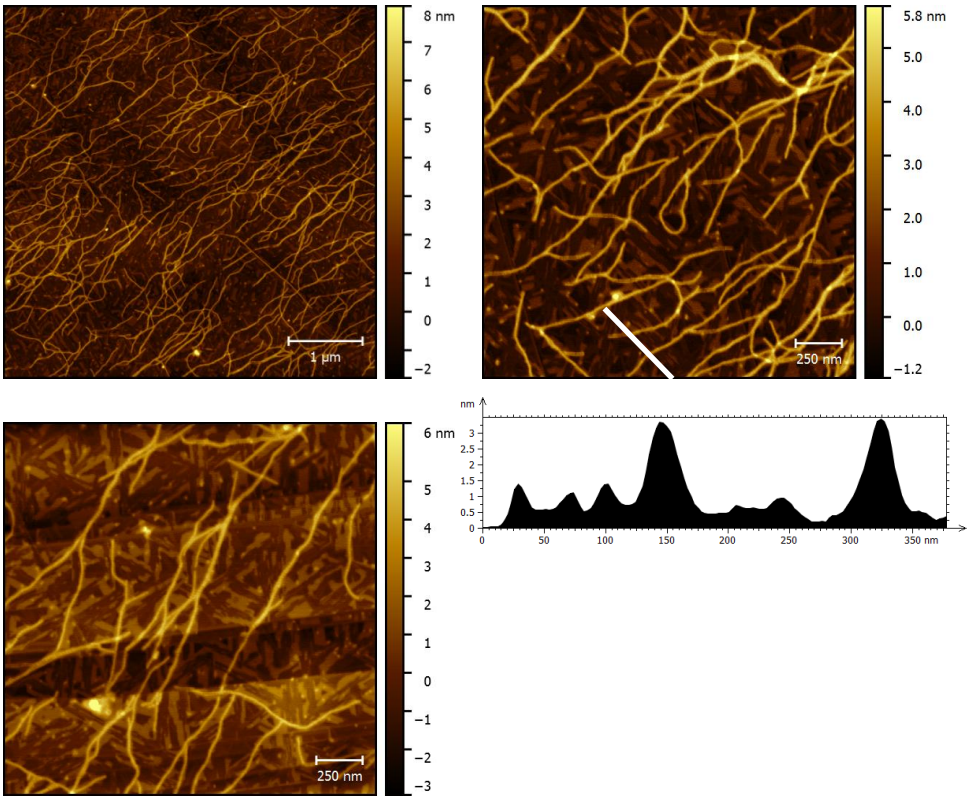

Figure 62. Tapping mode AFM images of Zn-(*R,R*)-**2** deposited at 0ºC on freshly cleaved HOPG.

The profile in Figure 62 shows a 3nm height for the fibres and a 1.5 nm height for the structure underneath, this presumably being non-aggregated metalloporphyrin, as a result that in solution the monomeric specie is always in equilibrium with the aggregate form. It was difficult to determine the length of the fibres due to the crossing between them, even so most of the fibres measures presented length larger than 1 µm.

A close-up image of Zn-(*R,R*)-**2** deposited onto graphite at 0ºC showed right-handed helicity in the fibre formation, clearly observable in the corresponding phase image. This helicity indicates a clear chiral transfer from monomer to aggregate that was observed in the high intensity CD signal. Even so, the helicity was not observable in all the fibres, perhaps because the small pitch length or

because the achiral organization of the long alkyl chains in the periphery of the porphyrin ring (Figure 63).[92,93,94]

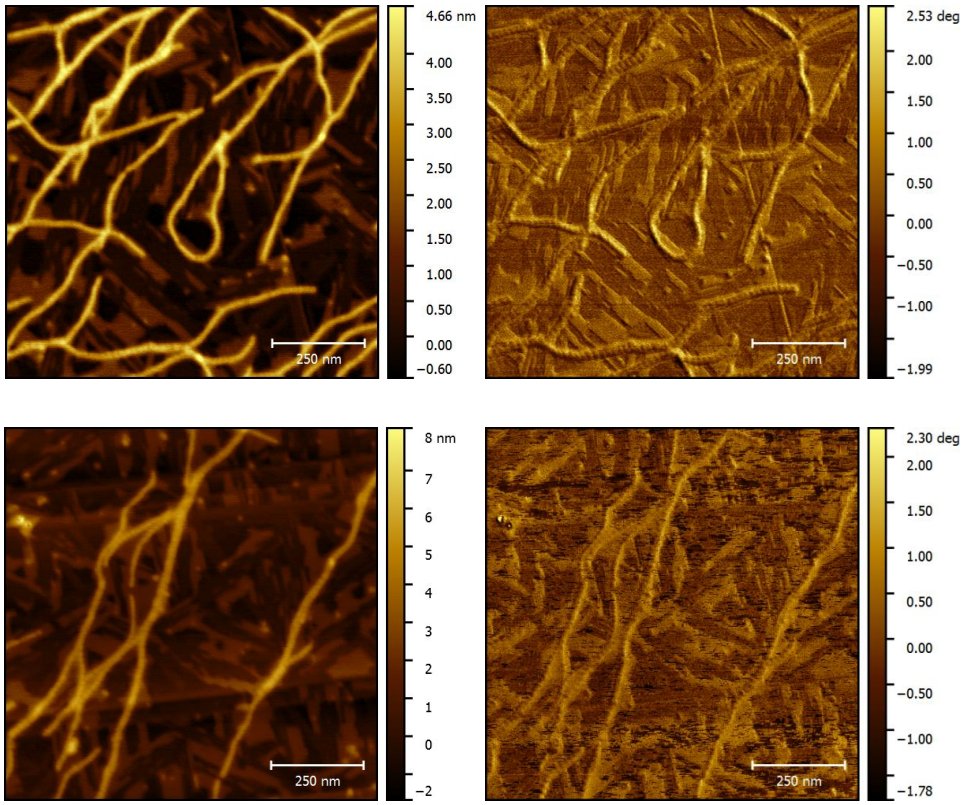

Figure 63. Tapping mode AFM images of of Zn-(*R*,*R*)-**2** at 0ºC on freshly cleaved HOPG. Helicity of the fibres observed in topographic and phase images.

While the results observed in the drop-casted solutions at low temperature were matched perfectly with the results observed in circular dichroism, the room temperature solution transferred onto surface differed from the studies on solution where as far as it could observe only 450.0 nm band attributed to a larger superstructure formation was present. This different behaviour between solution and surface studies could be related to the fast evolution from discrete aggregate to larger aggregate in solution, but when adsorbed on the surface all the species presents in the solution can be trapped, either larger aggregate, or tetramer structure or isolated molecules. As mentioned before, the transfer of aggregates from solution to surface can be affected by different factors such as molecule-surface interaction and the solvent used. The faster

(92) Lohr, A.; Lysetska, M.; Würthner, F. *Angew. Chem. Int. Ed.* **2005**, *44*, 5071-5074.
(93) Frauenrath, H.; Jahnke, E. *Chem. Eur. J.* **2008**, *14*, 2942-2955.
(94) Iwaura, R.; Hoeben, F. J. M.; Masuda, M.; Schenning, A. P. H. J.; Meijer, E. W.; Shimizu, T. *J. Am. Chem. Soc.* **2006**, *128*, 13298-13304.

evaporation of the solvent at room temperature might be allow the observation of the discrete aggregate that was not possible to detected by spectroscopic techniques.

The statistical study at room temperature of Zn-(*R,R*)-**2** in one area where spherical particles predominate as aggregate, showed a narrow dimensions distribution of the particles (Figure 64). The major number of particles presented diameters between 14 to 26 nm as a result of interactions between different tetramers aggregates. Comparing this results with porphyrin Zn-(*R,R,R*)-**1** it appears that this metalloporphyrin tends to form smaller particles maybe due to the fibre formation in solution.

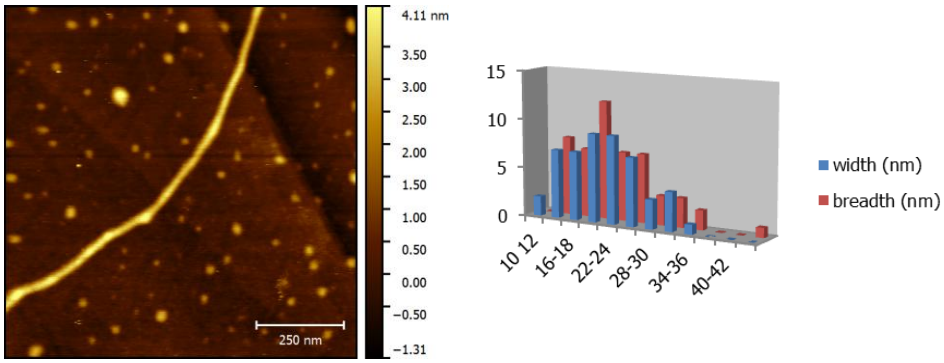

Figure 64. Tapping mode AFM images of Zn-(*R,R*)-**2** on freshly cleaved HOPG and statistical graph of particle dimensions.

Topographic images of Zn-(*R,R*)-**3** drop-casted at room temperature showed globular structure as a main architecture on graphite surface (Figure 65). As is observed in the topographic images, non homogeneous globular aggregates are present on the surface with heights between 3 to 6 nm as the profile in the image (c) shows. The small spherical structure with 3 nm height as was presented in the previous metalloporphyrins above correspond to the discrete tetramer aggregate, while the big ones were a superposition of various of these superstructures. Furthermore, images (a) shows poorly defined spherical big structures with around 20 nm heights that may suggest that some of the tetramer aggregates stick together in the evaporation process of the solvent.

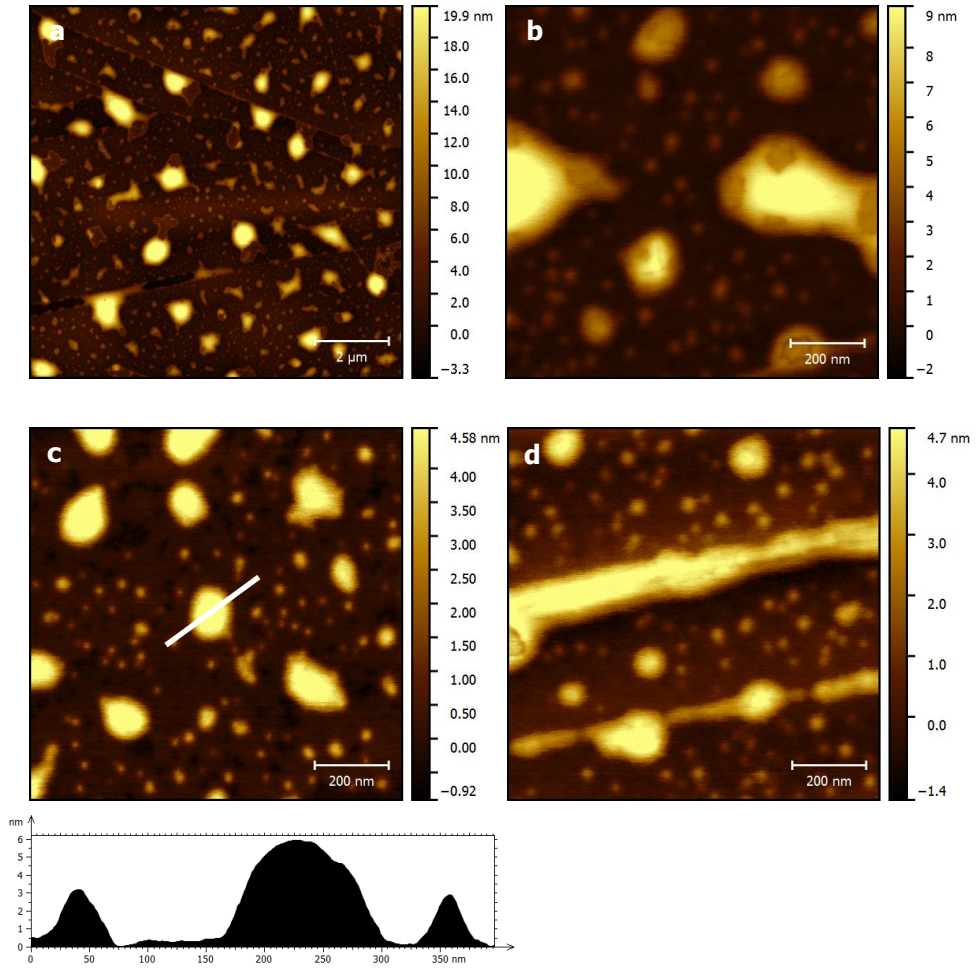

Figure 65. Tapping mode AFM images of Zn-(*R,R*)-**3** deposited at room temperature on freshly cleaved HOPG.

When methylcyclohexane/3% $CHCl_3$ solution (5 µM) of the metalloporphyrin Zn-(*R,R*)-**3** was cooled and successfully deposited onto graphite a higher globular particles were recognized with around 25 nm thickness. Apart from that it could observed that all the surface was covered by poorly organized structures 2nm in height that could be attributed to a monomeric species that remained in solution (Figure 66). Topographic images (b) and (d) clearly show the evaporation effect on the surface for the observation of agglomeration of disordered compound over the graphite support.

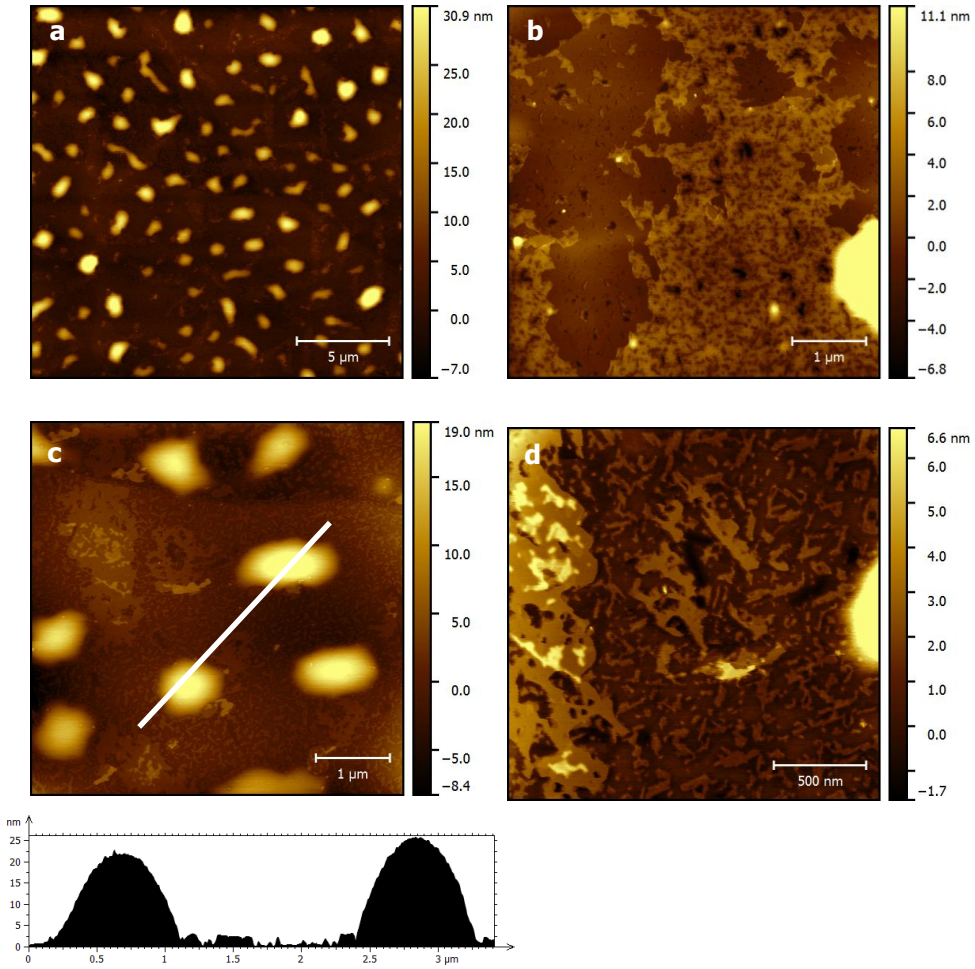

Figure 66. Tapping mode AFM images of Zn-(*R,R*)-**3** deposited on freshly cleaved HOPG at 0ºC.

As expected, only globular structures attributed to a superposition of tetramer aggregates for the big ones were observed on surface, take into account that the self-assembly of this metalloporphyrin in solution did not show a formation of secondary structures as the temperature decreased.

If statistically analysed the dimensions of the small particles in the AFM images at room temperature for metalloporphyrin Zn-(*R,R*)-**3** it was deduced that the major number of these small globular stacks have a diameter between 14 to 20 nm, although they have a great tendency to form a bigger aggregates as could be appreciated in the topographic images shown in Figure 67.

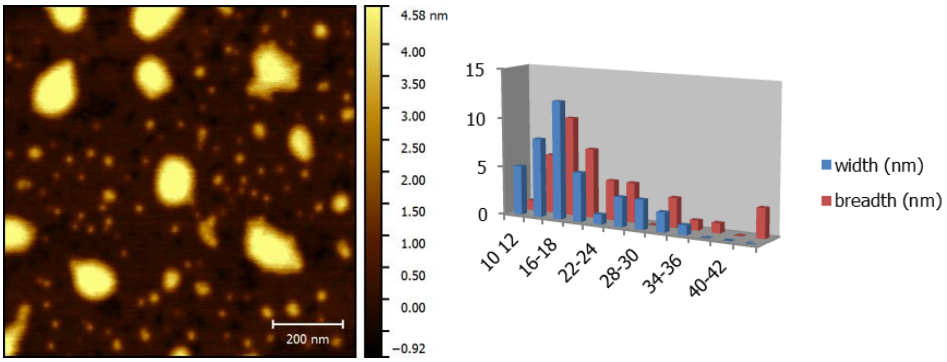

Figure 67. Tapping mode AFM images of Zn-(*R*,*R*)-**3** on freshly cleaved HOPG and statistical graph of particle dimensions.

The last metalloporphyrin studied on the surface, Zn-(*R*)-**4**, showed discotic figures with heights around 2.5 nm in its topographic images after room temperature deposition, as the profile shows, corresponding to a perpendicular porphyrin coordinated to a flat porphyrin on the surface and 1 nm height for smaller spherical structures after drop-cast the methylcyclohexane/ 3% $CHCl_3$ solution. Moreover, underneath a kind of organization on surface with a height lower than 0.5 nm was appreciated (Figure 68). One explanation of the flat structure of this sample could be related to the presence of only one amide group in their structure and the short length from pyridyl to pyridyl in the porphyrin.

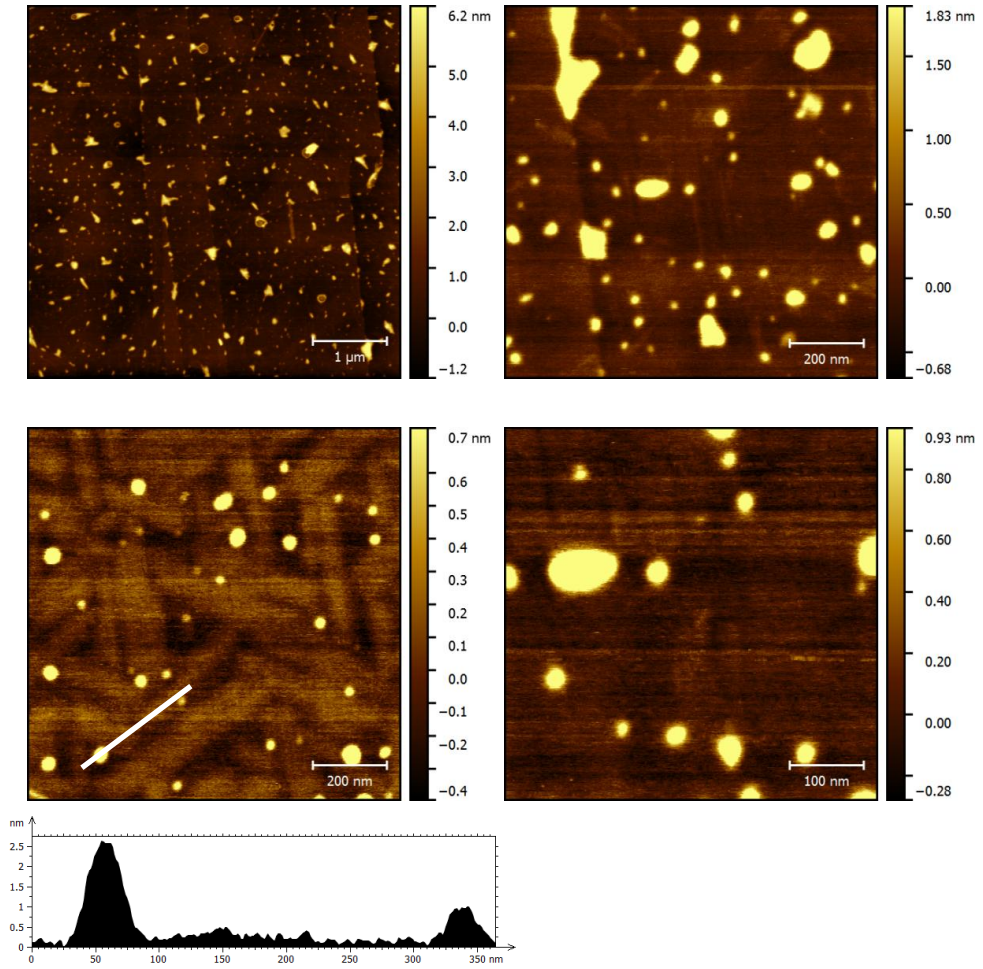

Figure 68. Tapping mode AFM images of Zn-(*R*)-**4** at room temperature on freshly cleaved HOPG.

When another region of the surface was analysed, a part of the discotic figures observed previously, the surface was covered by a layer of a non organized molecules with height around 1.5 nm as the profile suggest (Figure 69).

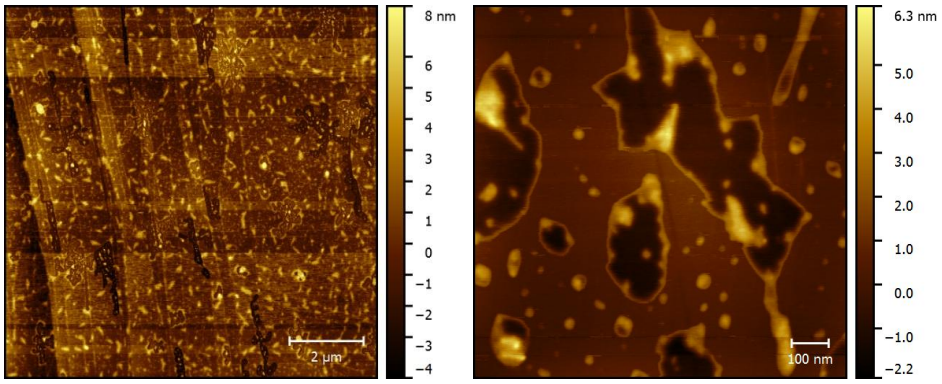

Figure 69. Tapping mode AFM images of Zn-(*R*)-**4** deposited at room temperature on freshly cleaved HOPG.

When the methylcyclohexane/ 3% $CHCl_3$ 5 µM solution of Zn-(*R*)-**4** was cooled down at 0ºC the surface was covered by a flat layer with triangular features, moreover as it can appreciate in the topographic images a height sheet features on top of the first layer were deposited onto the surface (Figure 70). The lower solubility for that metalloporphyrin could influence in the aggregate formation in solution as it was observed in the CD measurements, favouring interactions between alkyl chains. Therefore, the features observed in the AFM analyses also were influenced for that factor, suggesting stronger van der Waals interactions between the porphyrin ring and the graphite surface.[90]

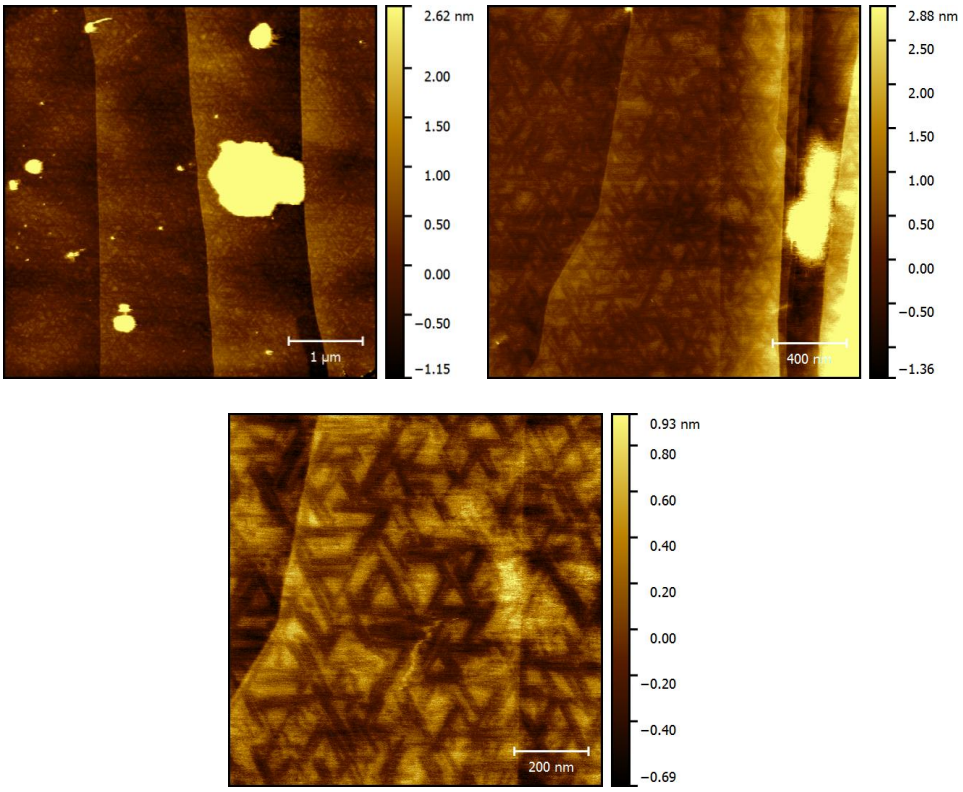

Figure 70. Tapping mode AFM images of Zn-(*R*)-**4** at 0ºC on freshly cleaved HOPG.

Figure 71 shows the statistic dimensions for the spherical particles of Zn-(*R*)-**4** when the solution was drop-cast onto graphite surface at room temperature, showing a diameters around 14 to 20 nm. Comparing the size of the particles of Zn-(*R*)-**4** with metalloporphyrin Zn-(*R,R,R*)-**1** these are smaller, that suggest that the size is influenced by the number of amide groups with the long alkyl chain in the structure.

These results on surface could explain why even presenting a 450 nm band in absorption spectroscopy, the circular dichroism was so different compared with Zn-(*R,R*)-**2**.

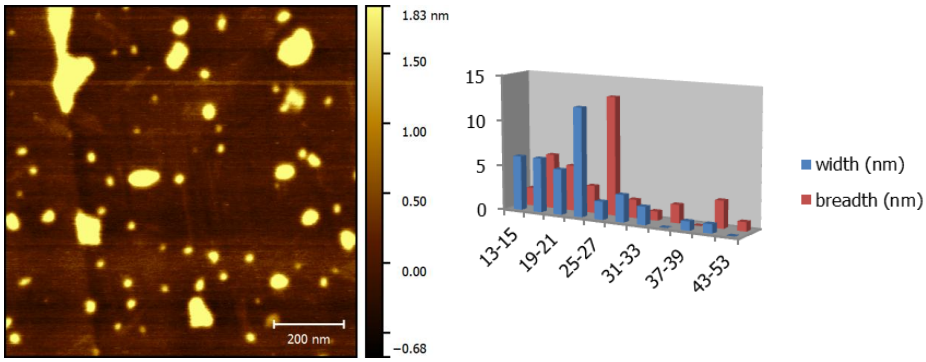

Figure 71. Tapping mode AFM images of Zn-(*R*)-**4** on freshly cleaved HOPG and statistical graph of particle dimensions.

2.8. Study of the self-assembly of free-base porphyrins and metalloporphyrins on the solid state.

2.8.1. General aspects of infrared spectroscopy (IR).

Infrared spectroscopy is based on the vibration mode of the bonds in a molecule that depends on the mass of the atoms involve in the bond, the strength and their geometry. IR is a good technique to help us to identify the structure of the molecules due to the position, intensity and shape of the bands observed in the spectra, although the complete identification becomes complicated because the combination of the bands and the low intensity for some of them. Nevertheless, the identification of the finger print of the molecule and the presence or absence of bands associated to a specific group might possible the assignment of the spectra (Figure 72).

The infrared spectroscopy studies of porphyrins allowed identifying which vibrational modes were constants and which varies depending of the substitution of the porhyrinic ring.[95] Tetraphenyl porphyrin derivatives present in their spectra a constant bending vibration bands associated to the H_β-pyrrole at lower frequencies region (772-805 cm^{-1}) and the band attributed to the in-plane N-H bending appear at around 960-990 cm^{-1} while the out-of-plane N-H bending can be found at 690-710 cm^{-1} region. Moreover, bands associated to the porphyrin ring vibration and vibration of the aromatic rings can be observed at 1100-1250 and 1350-1600 cm^{-1}, respectively.

(95) Alben J. O.; Choi, S. S.; Adler, A. D.; Caughey, W. S. *Ann. N. Y. Acad. Sci.* **1973**, *206*, 278-295.

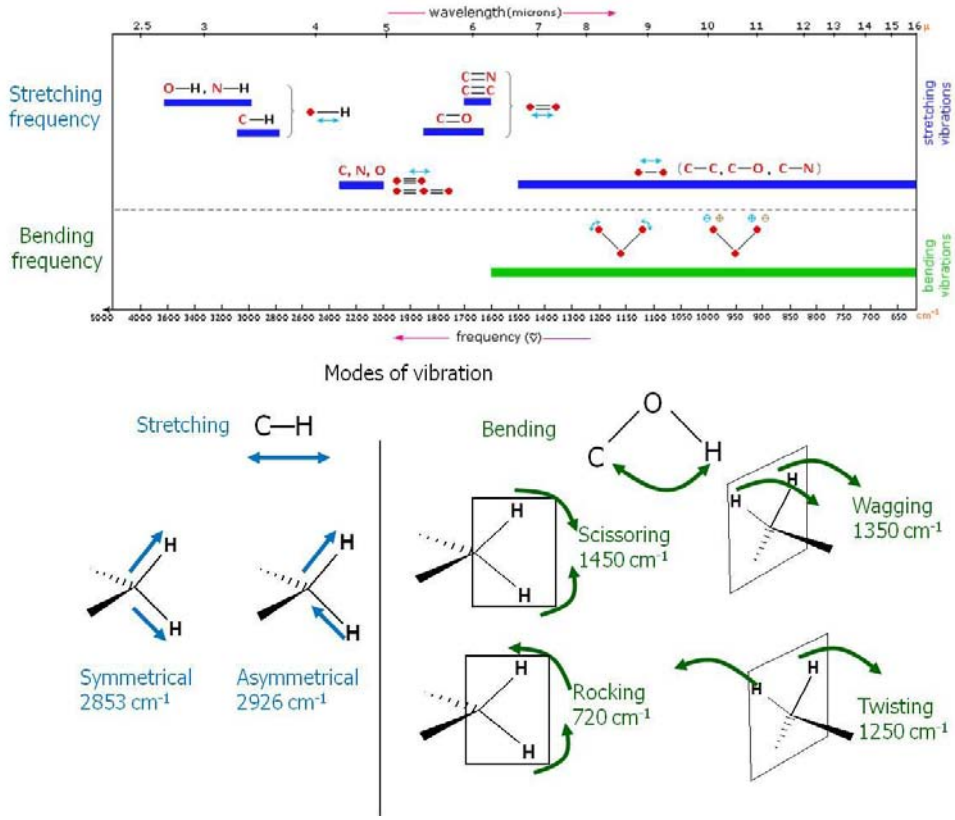

Figure 72. Vibration frequencies of the specific groups and vibration modes.

2.8.2. Study of the self-assembly by FT-IR.

2.8.2.1. Precedents.

IR studies of the self-organization of the free-base porphyrins and metalloporphyrins in the solid state recovered after evaporation in a non-controlled precipitated way helped us to understand the structure of the aggregates and which groups are involved in the packing of within them.

The porphyrins studied here contain amide groups as hydrogen-bonding units and pyridine as a coordinating ligand. It was observed that self-assembly in solution was driven mainly by the pyridyl-Zn (II) coordination, but different non-covalent interactions could participate in the organization of the molecules in the solid state beyond the first level of the supramolecular structure.

Commonly, amide groups present two peaks for the carbonyl group in different regions of the IR spectra, one located at around 1660 cm^{-1} associated to the C=O stretching (amide I) and the second band corresponding to the N-H bending appears at 1580 cm^{-1} (amide II).[96]

A previous work in our group reveled that different metal ions coordinated in the core of the porphyrin gave distinct self-assembly either in solution or in gel state presenting differences in the IR pattern (Figure 73).[41]

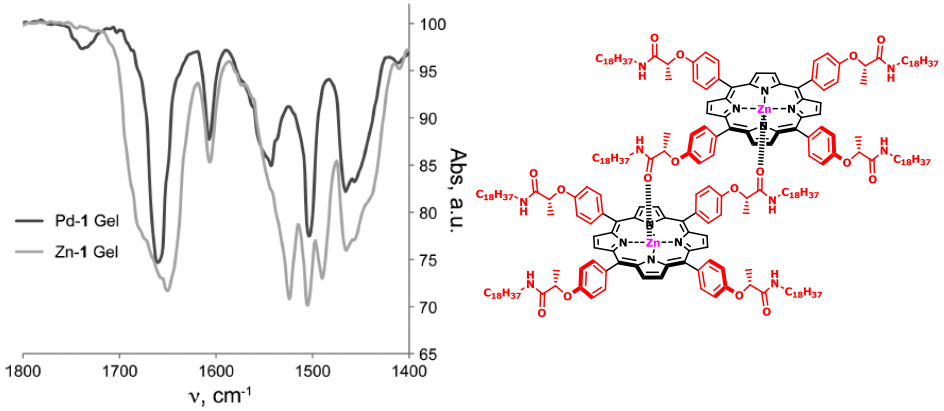

Figure 73. IR-ATR spectra of the Pd-**1** and Zn-**1**. Dimer structure for Zn-**1**.

The IR spectra of the chiral metalloporphyrins Pd-**1** and Zn-**1** show the different bands in the IR due to the differences in the self-assembly. While the Pd-porphyrin showed two different bands for the amide I as well as for the amide II, the Zn (II)-porphyrin showed a broad band for amide I and three different peaks associated to amide II at lower frequencies. These differences observed in the spectra indicated the different environment for the amide groups took place. The two bands for amide I and II in the Pd-porphyrin suggested that some of the amide groups in the structure were involved in the self-assembly by hydrogen-bonding (1662 cm^{-1}) and the weak peak at 1730 cm^{-1} was attributed to the non-aggregated amides. On the other hand, the broadening of the peak associated to the amide I in the Zn-porphyrin could be indicative of a coordination of the amide with the metal ion, whereas the splitting for the amide II suggested a complex network of the hydrogen-bonding over the whole aggregate. This precedent shows how the complexity of hydrogen-bonding in aggregates can be revealed, and especially that the amide carbonyl group can in principle coordinate the zinc (II) ion in the porphyrin.

2.8.2.2. Self-organization of free-base porphyrins.

Figure 74 shows an overview of the IR spectra of the free-base porphyrins (*R,R,R*)-**1**, (*R,R*)-**2**, (*R,R*)-**3** and (*R*)-**4**. All compounds present a peak at around 3300 cm^{-1} corresponding to N-H

(96) Shirakawa, M.; Kawano, S.; Fujita, N.; Sada, K.; Shinkai, S. *J. Org. Chem.* **2003**, *68*, 5037-5044.

stretching of the amide groups, moreover a second peak at around 3050 cm^{-1} attributed to the N-H (pyrrole) was observed for all porphyrins, most clearly in the spectrum of porphyrin (*R*)-**4** due to the decreased relative intensity of the N-H (amide).

Figure 74. IR-ATR spectra of the free-base porphyrins (*R,R,R*)-**1**, (*R,R*)-**2**, (*R,R*)-**3** and (*R*)-**4**.

In the lower energies region of the spectra a sharp peak at around 1230 cm^{-1} corresponding to C-O stretch of the phenyl group was observed, and the relative intensity of this peak decreased with the number of chiral amides in the structure.

If we zoomed the IR spectra of the free-base porphyrins, we could observe that they present the same pattern, but some peaks become more intense than the others depending of the substitution of the porphyrin ring (Figure 75).

The finger print region of the chromophores clearly showed a change in the relative intensity of the peaks related to amide and pyridyl groups. Furthermore, clearly two bands of the amide II were observed, while for the amide I peaks this behavior was not so obvious.

Figure 75. Zoom IR-ATR spectra of free-base porphyrins (*R,R,R*)-**1**, (*R,R*)-**2**, (*R,R*)-**3** and (*R*)-**4**.

In the spectra of porphyrins (*R,R,R*)-**1** and (*R,R*)-**3** two peaks at around 1681, 1651 cm^{-1} and 1676, 1659 cm^{-1} respectively were observed for the amide I suggesting that in the solid state these free-base porphyrins self-assemble through hydrogen-bonding but some of the amides did not participate in the organization of the supramolecular architectures. In general, hydrogen-bonding lowers the frequency of the amide I around 20 cm^{-1} indicating that 1651 and 1659 cm^{-1} for porphyrins (*R,R,R*)-**1** and (*R,R*)-**3** respectively correspond to the aggregated amide group, while 1681 and 1676 cm^{-1} are attributed to the non-aggregated amide that are shift to higher frequencies.[97] For porphyrins (*R,R*)-**2** and (*R*)-**4** a single broad peak centered at 1655 cm^{-1} was appreciated. The porphyrins also present two peaks related to amide II, a broad one at around 1535 cm^{-1} and a second peak sharper and more intense band at 1503 cm^{-1} corresponding to the aggregated and non-aggregated amide groups, respectively. Clearly one can appreciate two different peaks located at 1606 cm^{-1} attributed to the phenyl group and another one at 1592 cm^{-1} that are assigned to the pyridyl group. The tendency of these two peaks should be noted. While the peak corresponding to the pyridyl group became sharper and more intense the one from phenyl group became less intense until it is hidden by the pyridyl peak as the number of pyridyl groups increases in the structure.

Moreover, N-H stretching for the amide groups also can be present two different bands when aggregated and non-aggregated amide groups are present in the structure (Figure 76).

(97) Barth, A. *Biochim. Biophys. Acta* **2007**, *1767*, 1073-1101.

Figure 76. Zoom IR-ATR spectra of free-base porphyrins (*R,R,R*)-**1**, (*R,R*)-**2**, (*R,R*)-**3** and (*R*)-**4**.

As mentioned before, the N-H stretching for the amide groups appeared at around 3300 cm^{-1} but also we could observed a small band at around 3435 cm^{-1} that corroborate a different environment for the amide groups took place in the self-assembly, being at higher frequencies the peak related to the non-aggregated amide.[98]

Nevertheless, in order to understand well the organization of porphyrins in the superstructure, one has to pay attention to the peaks related to the amide group, that in principle are the ones involved in the self-assembly of the chromophore in the solid state. The splitting of the bands was indicative that some of the amide groups are involving in the aggregation by hydrogen-bonding whereas others were as non-aggregated amides. It should be appreciated that the solids on which the IR spectroscopy are performed are almost certainly not at the thermodynamic minimum because of the way the samples were prepared. Therefore, it is to be expected that some of the hydrogen-bonding groups are not seen to be interacting non-covalently. Keeping this information in mind, we could explain why in case of porphyrins (*R,R,R*)-**1** and (*R,R*)-**3** two different bands of the amide I were observed while for (*R,R*)-**2** and (*R*)-**4** a broad band were appreciated instead the two bands.

2.8.2.2.1. Structure propose for free-base porphyrins.

If we assume that as minimum one hydrogen-bonding is needed to self-assemble the superstructure, then it is easy to see that in porphyrin (*R*)-**4** where only one chiral amide is in the

(98) Gellman, S. H.; Dado, G. P.; Liang, G.-B.; Adams, B. R. *J. Am. Chem. Soc.* **1991**, *113*, 1164-1173.

periphery of the molecule, the intermolecular interaction will be the involves in the series. The same happens with porphyrin (*R,R*)-**2**, although this porphyrin contain two amide groups in the *meso* position, these are in "*trans"*-type position one respect to the other, therefore if one is involve in one hydrogen-bond the other strictly will be involve in a second hydrogen-bond only if they organize like a dimers, but if they self-assemble as larger structure some of the porphyrins remained uncoordinated (Figure 77).

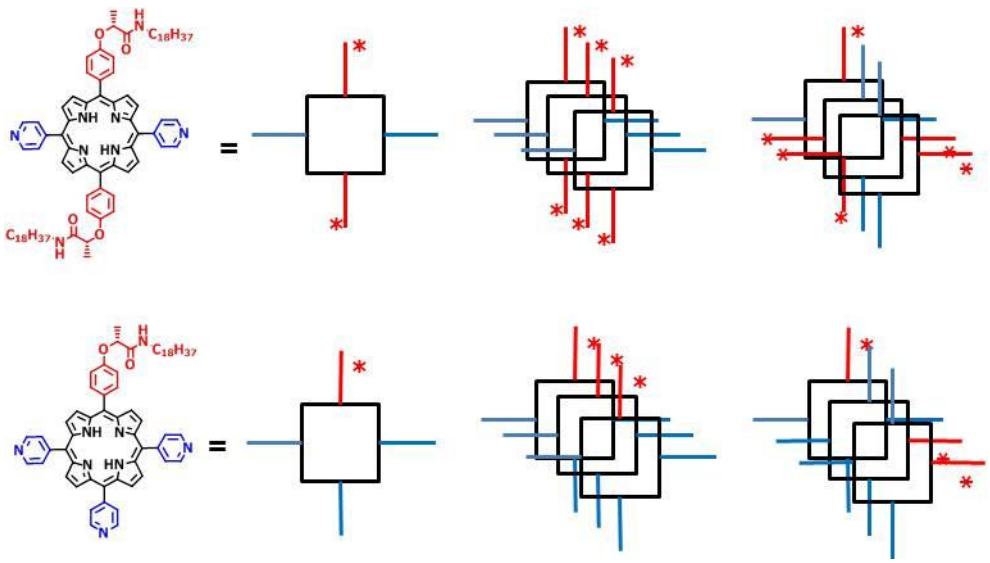

Figure 77. Structure proposed for porphyrins (*R,R*)-**2** and (*R*)-**4**.

The observation of different bands for the amide II in the IR spectra was due to the presence of hydrogen-bonds in the aggregate, otherwise only one peak will be observed and this will correspond to a non-aggregated amide.

On the contrary, the spectra of porphyrins (*R,R,R*)-**1** and (*R,R*)-**3** showed two separate bands for amide I, even though they are partially overlapped related to the different environment that these groups have in the structure, moreover as it is explained above, two bands for amide II were observed due to the intermolecular non-covalent interactions. If we focus in the peaks related to amide I, the presence of two peaks was an indicative that some of the amide groups were not participating in the self-assembly of the chromophore. Is important to take a look the conformation of these porphyrins, in one hand porphyrin (*R,R,R*)-**1** that contain three amide groups in the structure, on the other hand (*R,R*)-**3** that only two amide groups form part of the porphyrinic ring, but the important thing in here is that both of them have amide groups in 5, 10 position, a fact that leads to different conformations of the aggregate. In the idyllic situation, where all porphyrins are packing symmetrically and the second option, one porphyrin would be on top of another and rotated 90º because molecules tend to organize to achieve a thermodynamic

minimum, although the solids were not prepared under thermodynamic control. In the first case, in the symmetrical organization all the amides are hydrogen-bonded as it was the case of porphyrins (*R,R*)-**2** and (*R*)-**4** as most probable situation. In the second case, some of the amide groups are not participating in the packing of the aggregate and the read out will be the two bands observed of the amide I (Figure 78).

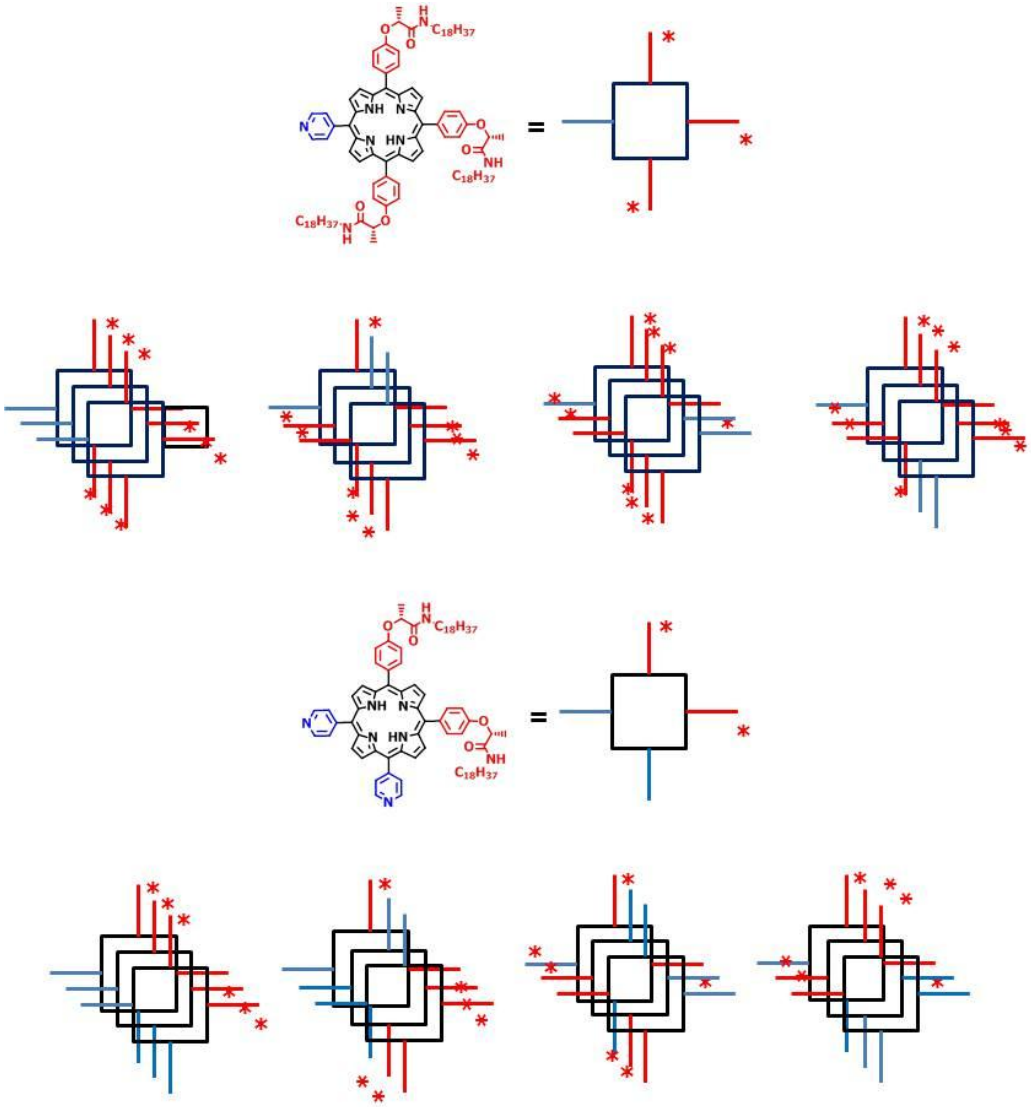

Figure 78. Structure proposed for porphyrins (*R,R,R*)-**1** and (*R,R*)-**3**.

2.8.2.3. Self-organization of the metalloporphyrins.

Figure 79 shows the IR spectra of the metalloporphyrins Zn-(*R,R,R*)-**1**, Zn-(*R,R*)-**2**, Zn-(*R,R*)-**3** and Zn-(*R*)-**4**, where the change in relative intensity of some peaks depending on the side groups in the porphyrin ring is observed as it was for the free-base compounds.

Figure 79. IR-ATR spectra of metalloporphyrins Zn-(*R,R,R*)-**1**, Zn-(*R,R*)-**2**, Zn-(*R,R*)-**3** and Zn-(*R*)-**4**.

Metalloporphyrins only presented a broad weak peak at around 3300 cm^{-1} corresponding to the N-H (amide) that decreases in intensity while the number of amide groups in the structure decreases, becoming nearly inappreciable in the case of metalloporphyrin Zn-(*R*)-**4**. Furthermore, a really small peak can be observed at around 3435 cm^{-1} that could suggest the formation of hydrogen-bonds as a secondary structure in the self-assembly of metalloporphyrins. On the contrary, the peak at around 3050 cm^{-1} from the pyrrole N-H completely disappears due to the coordination of Zn (II) metal ion in the core of the porphyrin ring (Figure 80).

Figure 80. Zoom IR-ATR spectra of metalloporphyrins Zn-(*R,R,R*)-**1**, Zn-(*R,R*)-**2**, Zn-(*R,R*)-**3** and Zn-(*R*)-**4**.

In case of zinc (II) metalloporphyrins, the effect of non-aggregated, aggregated amide groups is more evident, considering that the shift from the free amide group is observed around 1730 cm^{-1}. Comparing the spectra of the metalloporphyrins with the free-base porphyrins, one could suggest that the constitution in these metalloporphyrins does not play an important role because all of them present a very similar IR pattern, independently of the number and position of the amide groups, but if we carefully observe each spectra, some important information can be extracted (Figure 81).

As mentioned before, all the metalloporphyrins follow a similar pattern, presenting three peaks in the region of the amide II, situated at around 1525, 1505 and 1488 cm^{-1} and their relative intensities change with the number of amides in the structure as was expected. The presence of three peaks in this region suggested that hydrogen-bonding is present in the solid but these interactions did not follow a long range of order and several environments are present in the complex structure.

Nevertheless, the main differences were observed in amide I. While the peak associated to the hydrogen-bonded amide at 1662, 1673, 1667 and 1676 cm^{-1} respectively for compounds Zn-(*R,R,R*)-**1**, Zn-(*R,R*)-**2**, Zn-(*R,R*)-**3** and Zn-(*R*)-**4** was decreasing with the increasing of pyridyl groups in the structure, the relative intensity of the free-amide at around 1730 cm^{-1} was increasing with the number of pyridyl groups attached to the porphyrin ring.

Figure 81. Zoom of the IR-ATR spectra of metalloporphyrins Zn-(*R,R,R*)-**1**, Zn-(*R,R*)-**2**, Zn-(*R,R*)-**3** and Zn-(*R*)-**4**.

This behavior suggests that the arrangement of the main structure somehow prevents the presence of hydrogen-bond, and this effect was more evident as the number of the amides decreased on the porphyrin ring.

2.8.2.3.1. Structures propose for the metalloporphyrins.

Supposing that the main aggregate for the metalloporphyrins is a cyclic tetramer driven by coordination of the metal ion with the pyridyl group, we could suggest that secondary structures can be form driven by hydrogen-bonds as the IR spectra suggested.[99]

Figure 82 shows the structure propose by metalloporphyrins Zn-(*R,R,R*)-**1** and Zn-(*R*)-**4** as a representative self-assemble superstructures in the solid state for all the metalloporphyrins studied in here.

As it could observed in the structure proposed for the metalloporphyrins, as the number of amides raise the probability to form hydrogen-bonding between them increase and the amides that are not bonded must be because they were sterically hindered due to the whole aggregate structure. In the case of metalloporphyrin Zn-(*R*)-**4** which only contain one chiral amide at the periphery of the porphyrin ring, the number of bonded non-bonded amide groups become more similar, a fact that in the IR spectrum the band associated to the free amide and the amide involved in the hydrogen-bond having a similar intensity.

(99) Ganim, Z.; Chung, S. H.; Smith, A. W.; Deflores, L. P.; Jones, K. C.; Tokmakoff, A. *Acc. Chem. Res.* **2008**, *41*, 432-441.

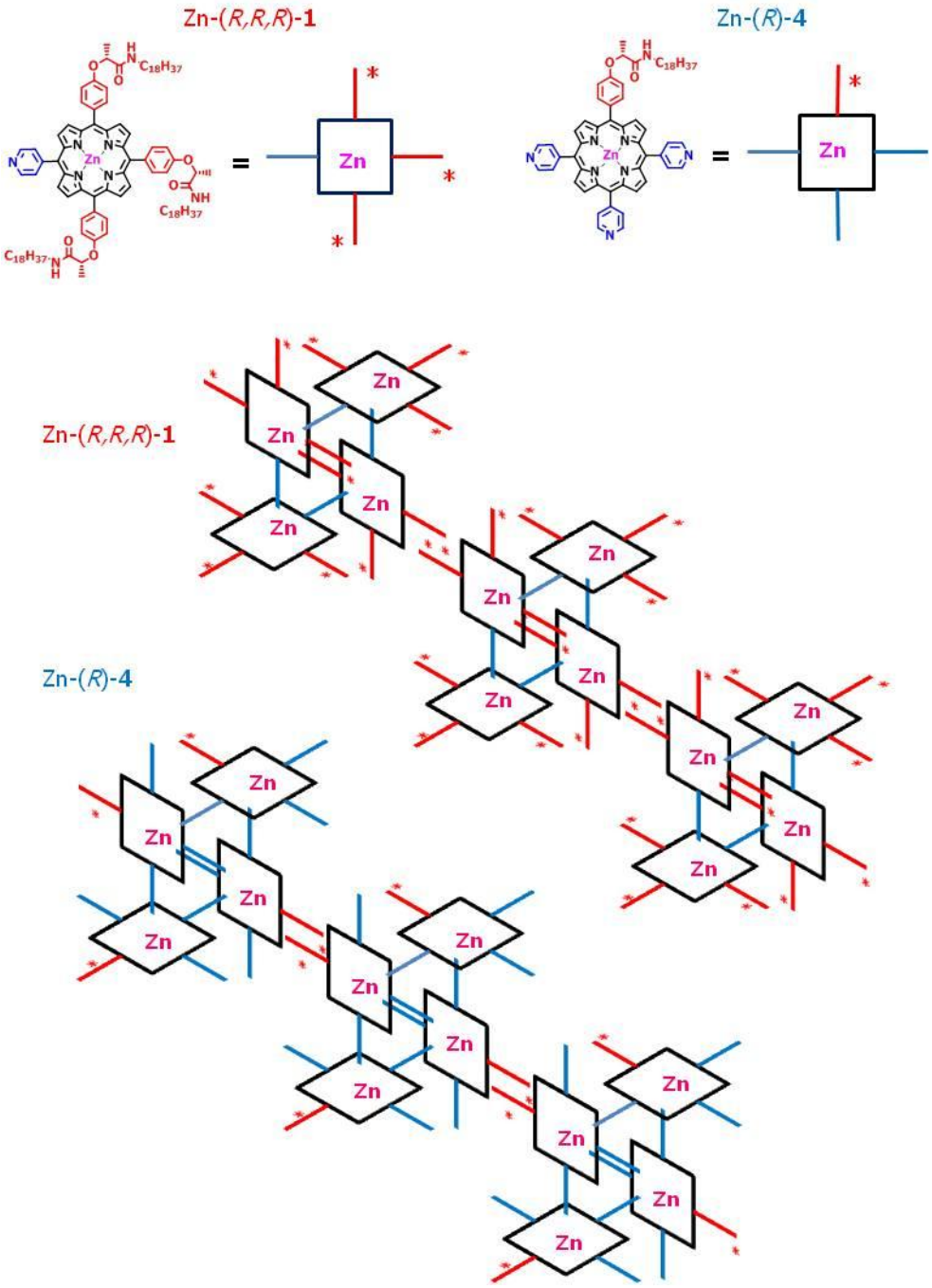

Figure 82. Structure proposed for metalloporphyrin Zn-(*R,R,R*)-**1** and Zn-(*R*)-**4**.

2.8.2.4. Other non-covalent interactions that can drive the organization of the free-base porphyrins and metalloporphyrins.

All the discussion was based in the self-assembly by hydrogen-bonding between amide groups in the case of free-base porphyrins and for metalloporphyrins as a secondary non-covalent interactions. However we have to keep in mind that pyridyl group can also be hydrogen-bond acceptor moiety involved in the self-assembly of free-base porphyrins (Figure 83).[100]

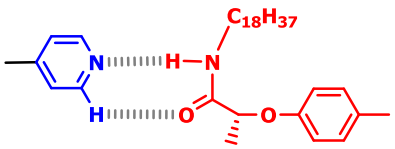

Figure 83. Hydrogen-bond between amide and pyridyl group.

One could expect that if pyridyl groups are involved in the organization of the molecule in the solid state, a shift could be noted in the IR spectra of porphyrins for the pyridyl group, but when the IR spectra of the free-base porphyrins and metalloporphyrins were compared no significant difference were observed (Figure 84).

Figure 84. Zoom IR-ATR spectra of free-base porphyrins (*R,R,R*)-**1**, (*R,R*)-**2**, (*R,R*)-**3** and (*R*)-**4** and metalloporphyrins Zn-(*R,R,R*)-**1**, Zn-(*R,R*)-**2**, Zn-(*R,R*)-**3** and Zn-(*R*)-**4**.

As the spectra show at around 1606 cm^{-1} the peak corresponding to the phenyl group is observed for porphyrins and metalloporphyrins while at around 1592 and 1594 cm^{-1} for porphyrins and metalloporphyrins respectively, the peak from pyridyl group is appeared, suggesting that pyridyl group does not suffer any significant change in the IR position depending of it environment. Even thought, it is clear in the spectra that the relative intensities between the two

(100) Steiner, T. *Angew. Chem. Int. Ed.* **2002**, *41*, 48-76.

groups, phenyl and pyridyl group is completely different when porphyrins and metalloporphyrins are compared.

Whereas in the free-base porphyrins the relative intensity of pyridyl group is higher than the phenyl group in all the compounds, for metalloporphyrins the behavior is in the other way around, being practically inexistent the pyridyl peak in metallocompound Zn-(*R*,*R*,*R*)-**1**. This behavior suggests that even the peak position does not change, the intensity could indicate that in metalloporphyrins the pyridyl group is coordinated with the metal ion of the core of the neighbor porphyrin.

2.8.3. General aspects of scanning electron microscope (SEM).

In the SEM, an electron beam is used to create a topographic image. The electrons interact with atoms of the sample, producing various signals such as secondary electrons (SE), back-scattering electrons (BSE) or X-rays that can be used to obtain information about the topography and composition of the sample under study. The most common mode is the detection of the secondary electrons produced after be excited by the electron beam (Figure 85).

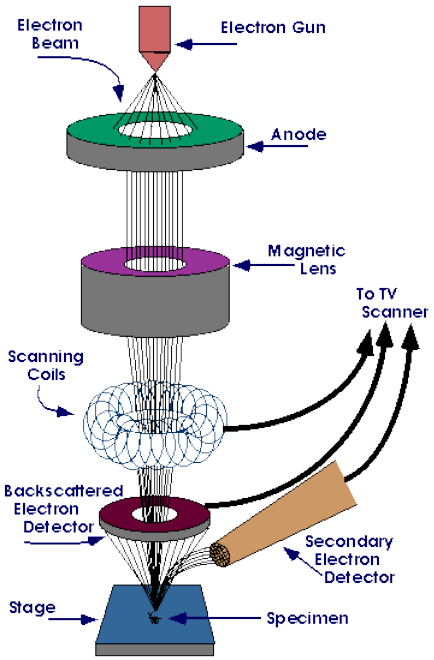

Figure 85. Scanning electron microscope (SEM).

This technique can achieve high resolution images (between 1-20 nm) depending of the sample and the work parameters that allow the creation of 3D images of the sample, moreover the study of conductive and non conductive samples can be performed. For a non conductive

samples such as biological entities, usually need to be covered by a metal (the most common is gold) to transfer a conductive behavior to the sample and create the image.

2.8.3.1. Morphology studies of the free-base porphyrins.

At a yet larger scale, the solid morphology of free-base porphyrins were analyzed after precipitation in far from equilibrium conditions from $CHCl_3$/EtOH solution. All the samples studied in here were analyzed without gold coating in low vaccum conditions because they were not conductive enough and to avoid overcharging the sample from the electron beam, higher pressures and lower potentials were used.

As observed in solution studies, free-base porphyrins (*R,R,R*)-**1**, (*R,R*)-**2**, (*R,R*)-**3** and (*R*)-**4** did not show any kind of aggregate, but under precipitation, they present a kind of fibrilar organization drive by the hydrogen-bonding between amide groups as the IR suggested.

Figure 86 shows the SEM images of the free-base porphyrin (*R,R,R*)-**1**. In images (a) and (c) a big particles of (*R,R,R*)-**1** are observed with a roughness texture but with any special organization, but when the precipitate was observed a higher magnification, the images revealed a clear fibrilar organization (Figure 86b and d). As is observed in image (b), a crosslink of thin fibers formed the whole structure driven by the hydrogen-bond between amide groups, but as the IR spectrum revealed, not all the amide groups are participating in the organization of the porphyrins.

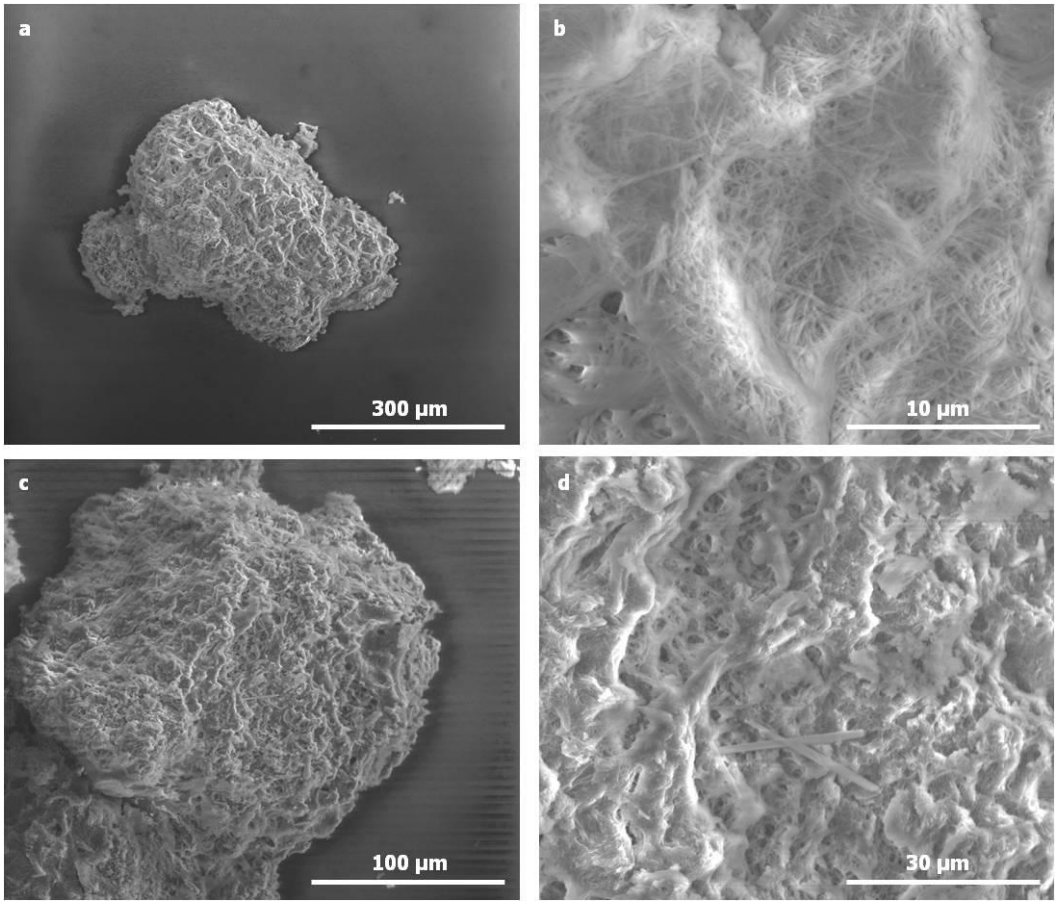

Figure 86. SEM images of free-base porphyrin (*R,R,R*)-**1** obtained from precipitation in $CHCl_3$/EtOH and deposited on a carbon tape.

As it was observed for porphyrin (*R,R,R*)-**1**, the free-base porphyrin (*R,R*)-**2** shows in its SEM images a fibrilar organization driven by the hydrogen-bonding of amide groups of consecutive porphyrins (Figure 87).

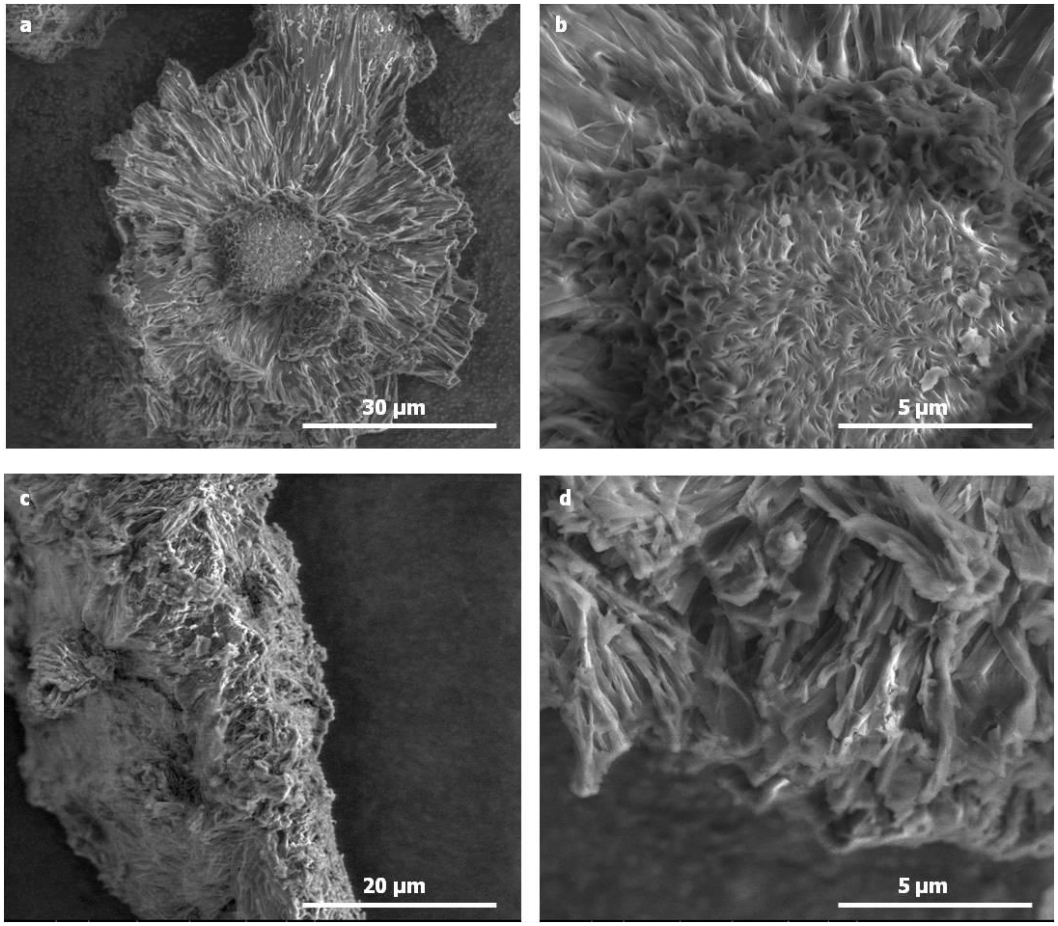

Figure 87. SEM images of free-base porphyrin (*R,R*)-**2** obtained from precipitation in $CHCl_3$/EtOH and deposited on a carbon tape.

If images (b) and (d) are compared, even both images present a fibrilar organization, they looked slight difference in its morphology. Figure 87b shows a short round fibers in the core of the image whereas in image (d) a long align more planar fibers are observed. These differences might come from by the non controlled way of precipitation or by the different state of aggregation of the porphyrin in different regions of the solid sample.

When porphyrin (*R,R*)-**3** was analyzed in SEM, different morphology of the solid after precipitation in $CHCl_3$/EtOH out-of-equilibrium was observed (Figure 88).

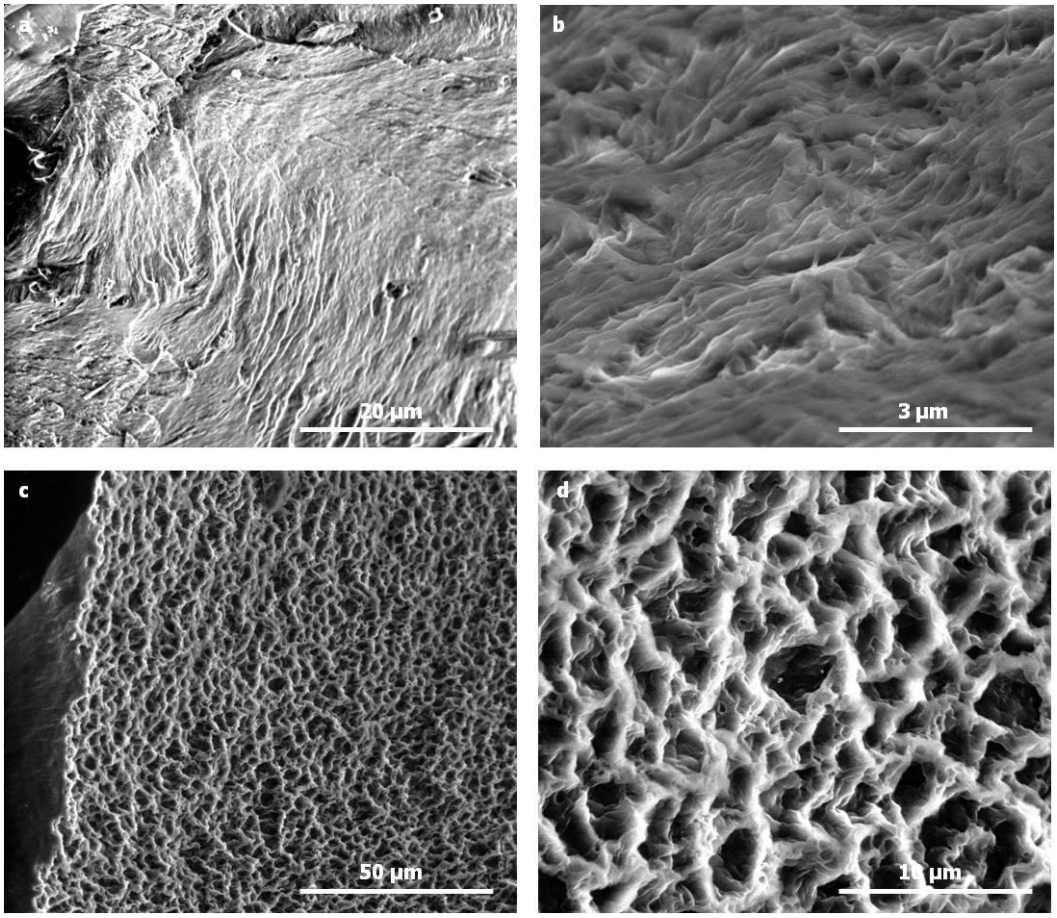

Figure 88. SEM images of free-base porphyrin (*R,R*)-**3** obtained from precipitation in $CHCl_3$/EtOH and deposited on a carbon tape.

While in the images (c) and (d) a kind of fibrilar morphology is observed on the top of the solid surface, images (a) and (b) present a more compact solid with a non specific organization.

However, porphyrins (*R,R*)-**2** and (*R,R*)-**3**, both of them with two chiral amide and two pyridyl groups connected in the *meso* position of the ring showed a different morphology that is an indicative that the constitution of the chromophore ring related to the position of the groups has a direct effect in the way of precipitation, and this is not only attributed to the aggregation in solution.

The free-base porphyrin (*R*)-**4** revealed in its SEM images a more compact solid as a main structure when is precipitated out-of-equilibrium conditions (Figure 89).

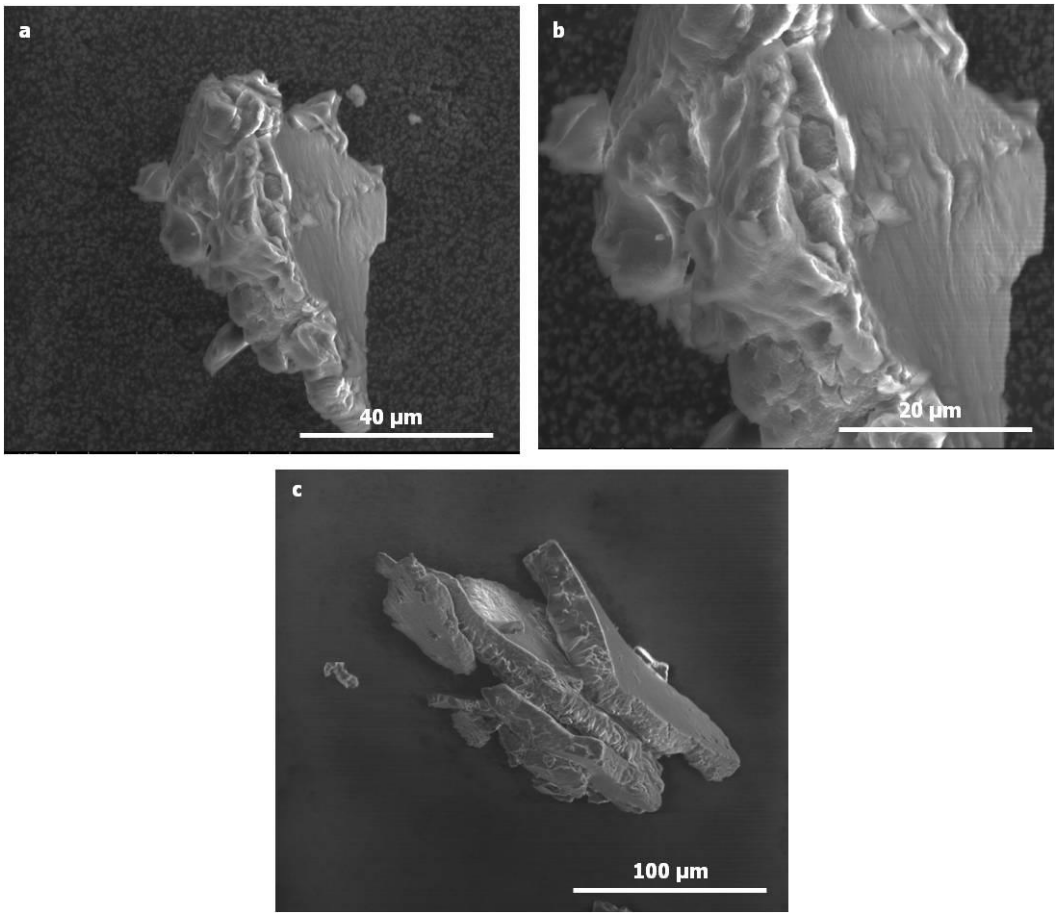

Figure 89. SEM images of free-base porphyrin (*R*)-**4** obtained from precipitation in $CHCl_3$/EtOH and deposited on a carbon tape.

As image (c) shows a planar blocks are the precipitate formed for porphyrin (*R*)-**4**. Even though, image (a) and more clearly appreciable in image (b), the porphyrin has the tendency to form a fibrilar organization driven by the hydrogen-bonding between amide groups. Nevertheless, this morphology is coherent if we take into account that only one amide group is in the porphyrin ring, and the lack of this groups with long alkyl chains might be directly affect in its morphology.

2.8.3.2. Morphology studies of metalloporphyrins.

The solid morphology of metalloporphyrins was analyzed after precipitation in far from equilibrium conditions from $CHCl_3$/EtOH solution. The metalloporphyrins under study were analyzed in the same working conditions as the free-base porphyrins in order to avoid the overcharging of the samples.

The solid hierarchy organization for metalloporphyrins observed in the SEM images revealed how Zn-(*R,R,R*)-**1** and Zn-(*R,R*)-**2** precipitated in a fibrilar manner, whereas Zn-(*R,R*)-**3** and Zn-(*R*)-**4** a more chaotic solid was observed after precipitation.

Figure 90 shows the hierarchy organization of Zn-(*R,R,R*)-**1** when the precipitate was deposit onto the carbon tape. As it can observe in the SEM images, the solid morphology is based in a thick fiber organization of the metalloporphyrin. As is explained in the solution studies, the main force to self-assemble the metalloporphyrins is the coordination between the pyridyl group and the zinc (II) metal ion in the core of the consecutive metalloporphyrin forming as a primary structure a cyclic tetramer. Furthermore, as in the case of free-base porphyrins, when metalloporphyrins are studied in solid state, hydrogen-bond between amide groups are involved in the organization of the samples. In the case of metalloporphyrin Zn-(*R,R,R*)-**1** was observed an evolution from the tetramer structure to a secondary superstructure based on this non-covalent interaction. The hierarchy propagation from the smallest unit and strongest interaction up to the solid where hydrogen-bonds and van der Waals forces must dominate give thicker fibers compare with the free-base porphyrin (*R,R,R*)-**1**. Moreover, if it takes a look to the images (d), (e) and (f) the fibers formed revealed a kind of helicity coming from the chirality transfer of the porphyrin unit to the larger aggregate.

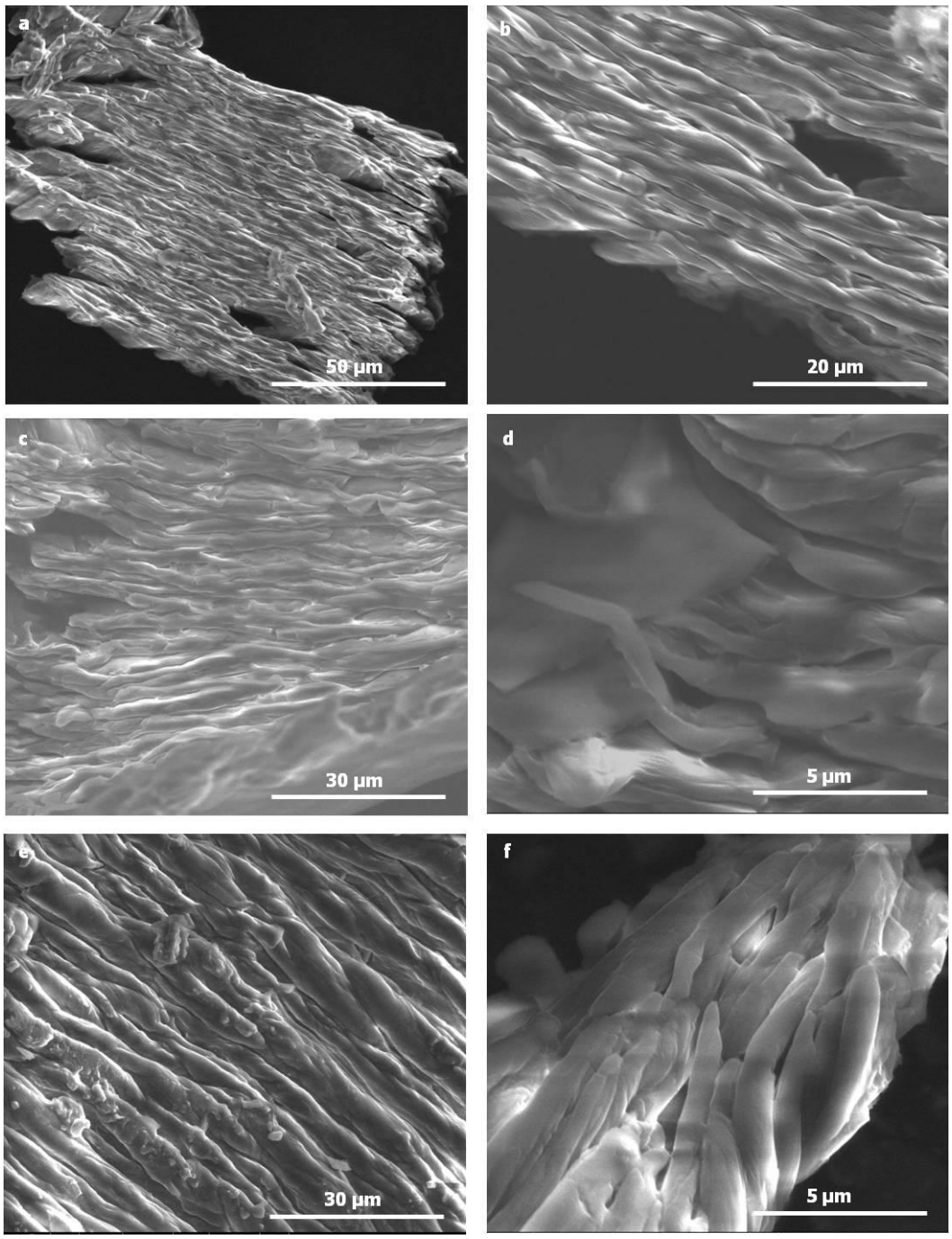

Figure 90. SEM images of metalloporphyrin Zn-(*R,R,R*)-**1** obtained from precipitation in $CHCl_3$/EtOH and deposited on a carbon tape.

Metalloporphyrin Zn-(*R,R*)-**2** showed in its SEM images two different solid morphologies when precipitated. Nevertheless, fibrilar organization is observed as a major hierarchy organization (Figure 91).

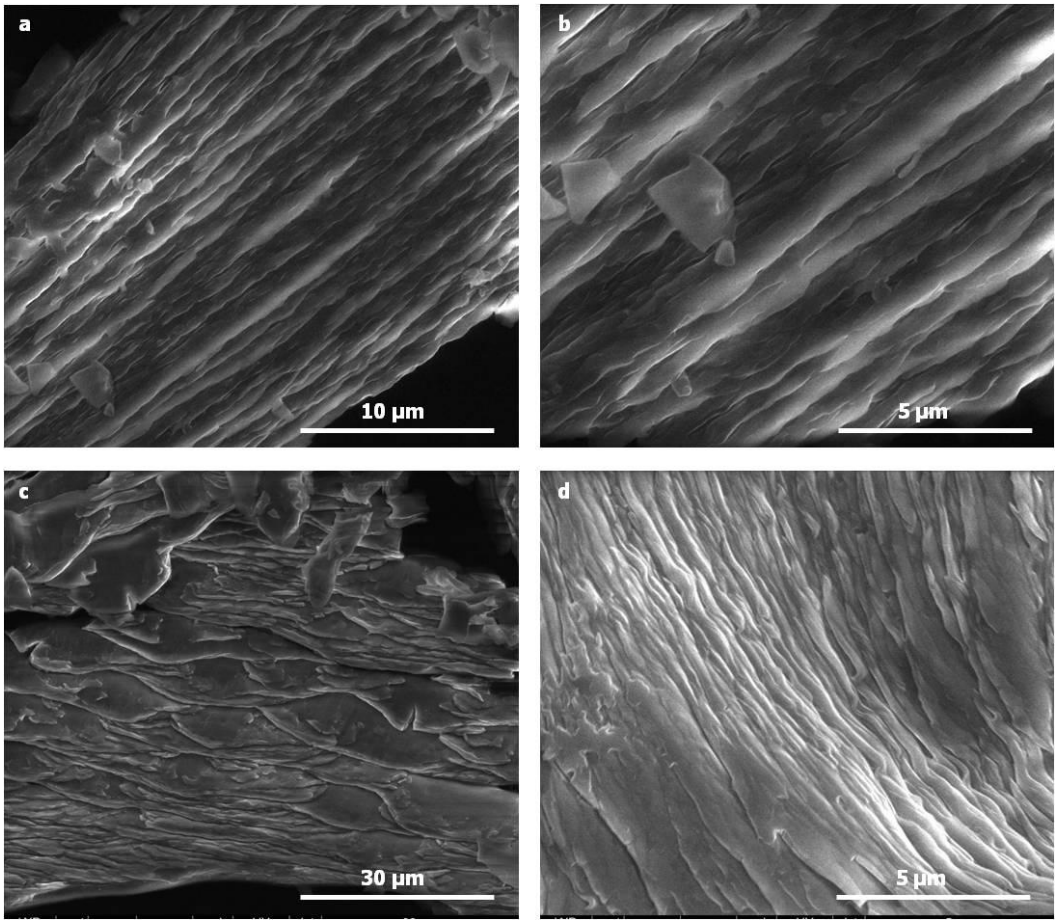

Figure 91. SEM images of metalloporphyrin Zn-(*R,R*)-**2** obtained from precipitation in $CHCl_3$/EtOH and deposited on a carbon tape.

While in images (a) and (b) a clear hierarchy fiber organization is observed, image (c) suggested a layer organization of the metalloporphyrin. Even though, image (d) that is a high magnification of image (c), a kind of fibrilar organization can be distinguish.

As observed in the AFM topographic image at 0ºC for metalloporphyrin Zn-(*R,R*)-**2**, helical fiber was transfer from solution to the solid support.

This behavior clearly suggests the chirality transfer effect from the monomeric units to the superstructure both in solution and in solid state.

When metalloporphyrin Zn-(*R,R*)-**3** was precipitate far from the equilibrium and deposited onto carbon tape, its SEM images revealed a more compact solid without any special organization instead the fibrilar organization observed for metalloporphyrins Zn-(*R,R,R*)-**1** and Zn-(*R,R*)-**2** (Figure 92).

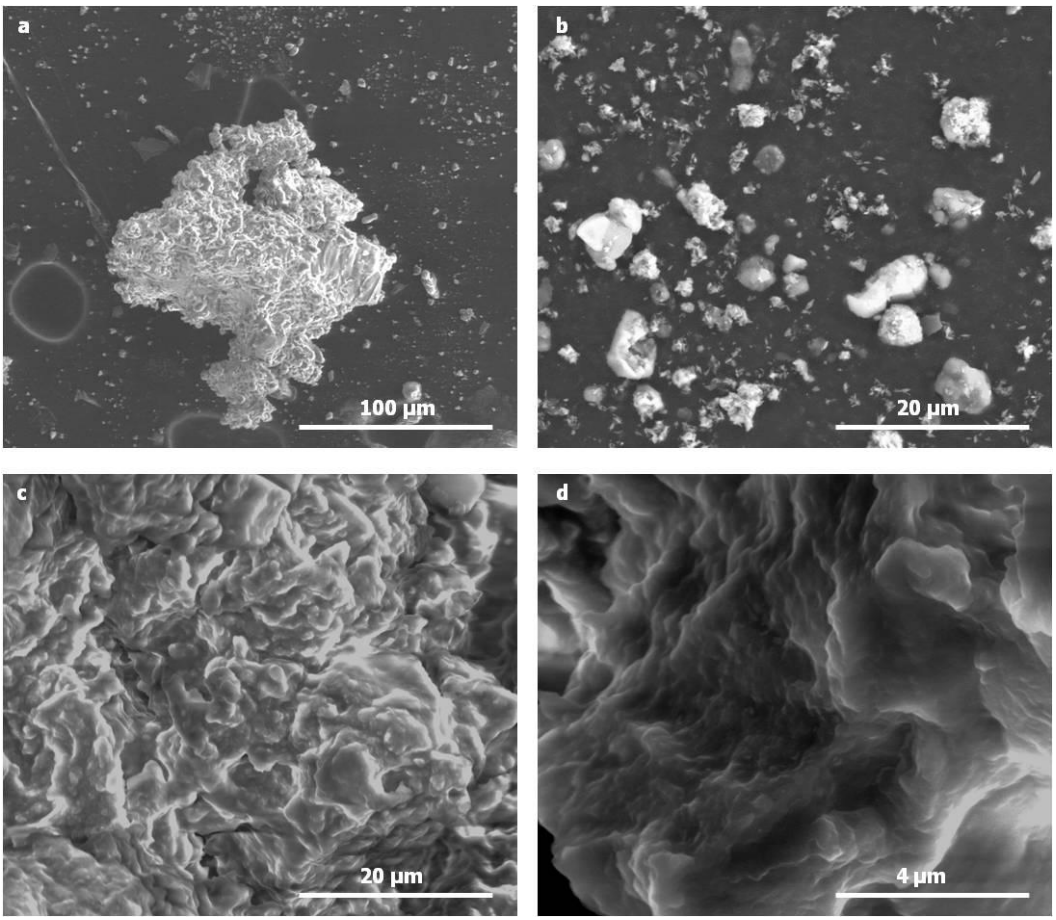

Figure 92. SEM images of metalloporphyrin Zn-(*R,R*)-**3** obtained from precipitation in $CHCl_3$/EtOH and deposited on a carbon tape.

Images (c) and (d) clearly show the non organize solid for the metalloporphyrin after precipitation, while in image (b) small solids are present on the carbon tape, that suggest that the big structure is formed by the combination of the small pieces.

As explained for the free-base porphyrins and also corroborate by the solution studies, the constitution and position of the chiral amide groups and pyridyl groups in the porphyrin structure directly affect in the hierarchy organization.

This is the case also of the metalloporphyrin Zn-(*R*)-**4** that with only one chiral amide group (as a hydrogen-bonding unit) with the long alkyl chain capable to interact by van der Waals with another chain of a neighbor porphyrin, formed a non-fibrilar solid when precipitated (Figure 93).

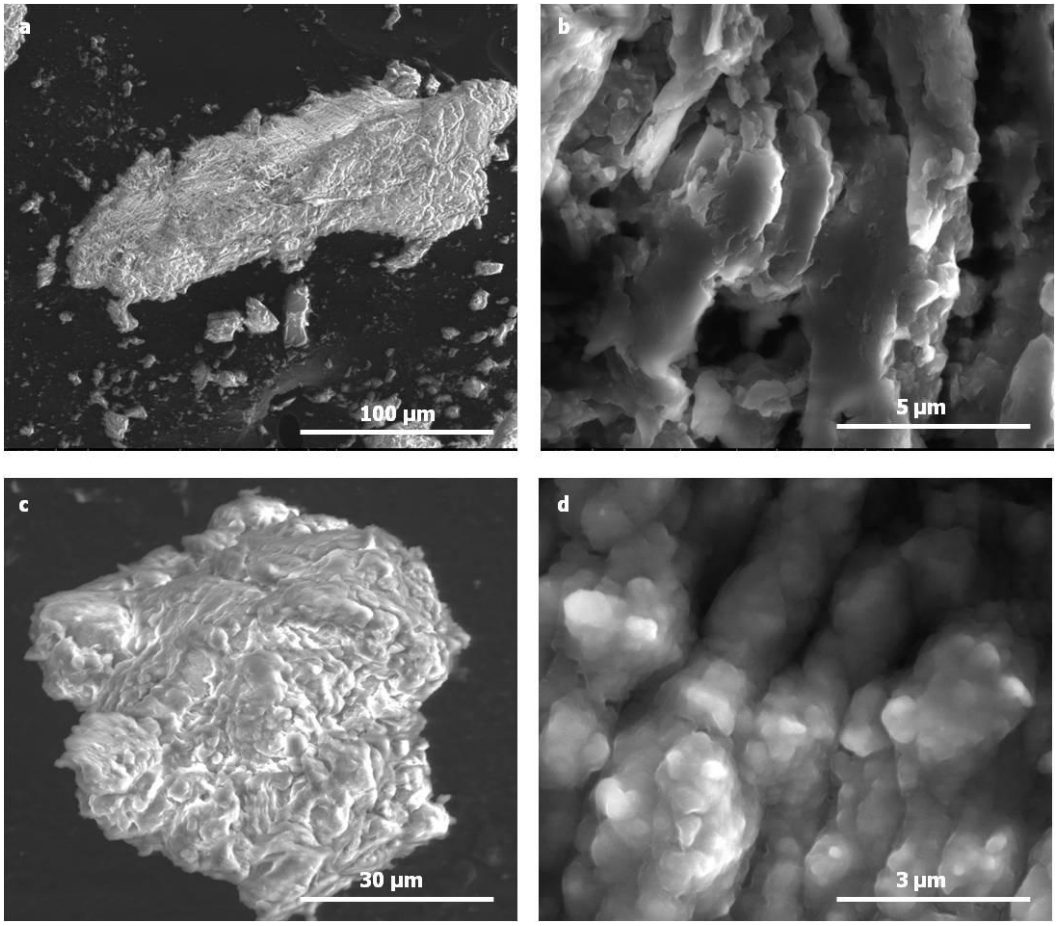

Figure 93. SEM images of metalloporphyrin Zn-(*R*)-**4** obtained from precipitation in $CHCl_3$/EtOH and deposited on a carbon tape.

As image (a) show, a kind of fibrilar organization, when the solid is observed closely in image (b), really the precipitate is not like a fiber, its organization is more like a planar layers. However, image (d) also suggest organization layer by layer, but in this image a globular protuberances form each layer instead a planar surface.

This difference might come from for the way of precipitation because as pointed out before, all the sample were precipitated out-of-equilibrium and then transfer to the carbon tape.

2.9. Conclusions.

It has been shown that a family of free-base porphyrins does not show self-assembly in solutions, whereas the chiral zinc (II) metalloporphyrins of the same family can exhibit hierarchical self-assembly with a complicated combination of supramolecular environments that give rise to high optical activity over a wide range of wavelength - from 400 to 475 nm - from a single chromophoric unit. The zinc (II) interaction with pyridyl moieties is the dominant interaction, but hydrogen-bonding and van der Waals interactions are responsible for the massive increase in optical activity that is observed.

The compound incorporating two pyridyl groups at the 12 and 6 o'clock positions of the porphyrin core (Zn-(*R,R*)-**2**) is the system that aggregates most strongly, and the optical activity of the aggregate indicates that inter-porphyrin stacking through weak interactions is very important as it is in the compound with one pyridyl group (Zn-(*R,R,R*)-**1**). The assembly is extremely sensitive to molecular constitution.

Importantly, the deposition of these aggregates onto graphite reflects the state of assembly in solution. When the compound incorporating one pyridyl ring was deposited at room temperature only small closed aggregates were observed, while a lower temperature deposition from solution larger scale fibrous structures were seen by AFM.

The effect of constitution on assembly in solid state is carried through to higher level aggregates formed under far from equilibrium conditions. The morphology of the materials varies contains fibers and lamellae with features that are unique in each case, and very different from those of the corresponding free-base porphyrin. This result emphasizes the potential of hierarchical assembly approaches not only because strong interactions facilitate aggregation, but also enhance the weaker interactions.

2.10. Experimental section.

NMR spectra : The nuclear magnetic resonance spectra were recorded in the *Servei de Ressonància Magnètica* of the *Universitat Autònoma de Barcelona*. The ^{1}H-NMR experiments were performed on Bruker DXP 250 spectrometer and Bruker ADVANCE 360 spectrometer at 298 K. Temperature studies and 2D NMR spectra were performed on Bruker AVANCE^{II} 600 spectrometer.

LDI-TOF : Mass spectroscopy performed with an Ultraflex (TOF/TOF) spectrometer.

FT-IR measurements : All FTIR measurements were recorded in Perkin Elmer (Spectrum one). The samples were of solid porphyrins (recovered after evaporation of solvent in a non-controlled precipitated way) and were performed in attenuated total reflection (ATR) mode. Porphyrins were measured on the plate of universal ATR (UATR).

SEM observations : Porphyrins and metalloporphyrins precipitated from 3:1 ratio $CHCl_3$/EtOH mixture solution were deposited onto a carbon tape. The accelerating voltage of SEM was 10 KV. The images were performed in a QUANTA FEI 200 FEG-ESEM microscope.

Atomic Force Microscopy (AFM) : Topographic AFM images were acquired in the dynamic tapping mode using a FORT Si tip in the *Servei de AFM of the ICMAB* in a Agilent 5100 microscope. Methylcyclohexane/3% $CHCl_3$ solutions of zinc porphyrins were drop-casted onto HOPG surface and measurements were performed at ambient conditions. Methylcyclohexane/3% $CHCl_3$ solutions of zinc (II) porphyrins were cold down at 0ºC in a bath ice and drop-casted onto HOPG surface. A nitrogen flow was used to evaporate the solvent. The color code in all the images shown is such that dark are lower and bright are higher values of the height.

CD measurements : A Jasco J-275 spectropolarimeter was used for CD spectra measurements. A Peltier-temperature programmer for thermosettting the samples was used to cool the solutions. The solution in methylcyclohexane with 3% of $CHCl_3$ were prepared by diluting a solid sample of the porphyrins and metalloporphyrins in the corresponding amount of the mixture solvents and the solution was heated until all the porphyrin had dissolved to obtain a 5 μM as final concentration. The sample was transferred to a quartz cuvette of 1 cm length to be analyzed. When the measure temperature was reached and stabilized, spectra were recorded.

UV-Visible absorption measurements : UV-Visible absorption measurements were performed using a UV-Vis-NIR Varian, model Cary 5 instrument using a 1 cm length quartz cells. All the samples were prepared, diluting a solid sample of the porphyrins and metalloporphyrins in the corresponding amount of the methylcyclohexane with 3% of $CHCl_3$ solution. The solution was heated until all the porphyrin had dissolved to obtain a 5 μM as final concentration.

Materials : Compound (*R*)-**6** was prepared as described previously.[36]

2.10.1. Synthesis of (R)-Methyl 2-(4-formylphenoxy)propanoate (R)-6.

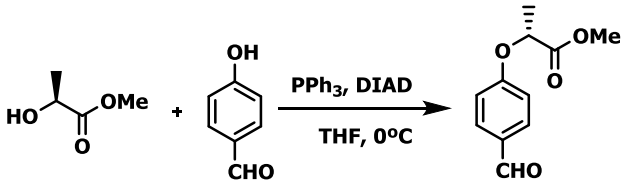

(*R*)-6

4-hydroxy-benzaldehyde (10.0 g, 81.9 mmol), *S*-(-)-methyl lactate (9.40 ml, 98.3 mmol) and triphenylphosphine (25.8 g, 98.3 mmol) were dissolved in anhydrous THF (300 ml). The mixture was stirred vigorously at 0ºC and under Ar atmosphere for 10 minutes. A second solution of diisopropyl azodicarboxylate (19.4 ml, 98.3 mmol) in anhydrous THF (100 ml) was added dropwise over 30 minutes. The resulting solution was stirred overnight at room temperature. H_2O was added in order to quench the reaction and then the solvent was removed under pressure. The aqueous solution was extracted with CH_2Cl_2 (3x20 ml) and the organic phase was dried over $MgSO_4$ anhydrous. Finally, the organic solvent was filtered through cotton wool and evaporated to give yellow oil. The crude compound was purified by silica gel column chromatography (hexane/EtOAc, 8:2) to obtain 14.2 g (83.1%) of the desired compound (*R*)-**6**. **M.F. :** $C_{11}H_{12}O_4$; **M.W. :** 208.22 g/mol: **^{1}H-NMR** (250 MHz, *d*-chloroform) δ 9.80 (s, 1H; CHO), 7.74 (d, *J* = 8.6 Hz, 2H; ArH), 6.90 (d, *J* = 8.8 Hz, 2H; ArH), 4.82 (q, *J* = 6.8 Hz, 1H; O<u>CH</u>(CH_3)), 3.69 (s, 3H; $COOCH_3$), 1.59 (d, *J* = 6.8 Hz, 3H; OCH(<u>CH_3</u>)) : **$[\alpha]_{546literature}$ =** +46 deg·cm^2/mg,[36] **$[\alpha]_{546observed}$ =** +43 deg·cm^2/mg (c=0.19 M; CH_2Cl_2).

2.10.2. Synthesis of ester functionalized chiral porphyrin derivatives 7-12.

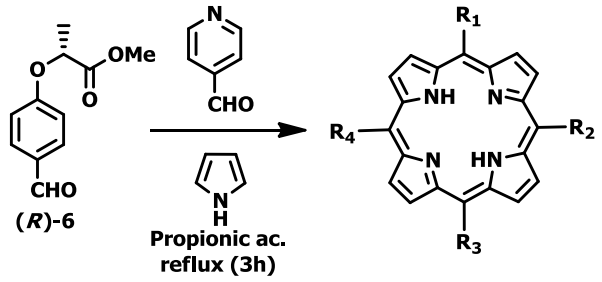

(*R*)-Methyl 2-(4-formylphenoxy)propanoate (*R*)-6 (1.00 g, 4.80 mmol) was dissolved in propionic acid (40 ml, 0.12 M), pyridine-4-aldehyde (0.45 ml, 4.80 mmol) was added, and the resulting mixture was refluxed with vigorous stirring for 30 minutes in air. Pyrrole (0.33 ml, 4.80 mmol) freshly filtered through neutral alumina was added drop by drop at 150ºC and then the

mixture was allowed to reflux for about 3 hours. Propionic acid was distilled under reduced pressure. The dark crude product was subjected to column chromatography on silica gel for purification (CH_2Cl_2/1.0% MeOH) and five different impure fractions were obtained. Each fraction was then purified by silica gel chromatography (CH_2Cl_2/1.5% MeOH) to obtain (*R,R,R*)-**8** (63.0 mg, 1.4%), (*R,R*)-**9** (21.0 mg, 0.5%), (*R,R*)-**10** (61.0 mg, 1.5%), (*R*)-**11** (93.0 mg, 2.7%), **12** (60.0 mg, 2.0%).

5,10,15-[4-(*R*)-Methyl-2-phenoxypropionate]-20-[4-pyridyl] porphyrin (*R,R,R*)-8 : M.F. : $C_{55}H_{47}N_5O_9$; **M.W. :** 921.77 g/mol ; **Found LDI-Tof [M^+] :** 923.8 ; **^{1}H-NMR** (250 MHz, *d*-Chloroform) δ 9.05 (d, *J* = 5.0 Hz, 2H; ArH), 9.01-8.86 (m, 6H; 2 pyrrole CH, 4 pyridyl), 8.84 (d, *J* = 4.6 Hz, 2H; pyrrole CH), 8.22 (d, *J* = 5.3 Hz, 2H; pyrrole CH), 8.17 (dd, *J* = 8.5, 2.1 Hz, 6H; ArH), 7.31 (d, *J* = 8.3 Hz, 6H; ArH), 5.20-5.05 (m, 3H; O<u>CH</u>(CH_3)), 3.97 (s, 9H; $COOCH_3$), 1.88 (d, *J* = 6.7 Hz, 9H; OCH(<u>CH_3</u>)) -2.71 (s, 2H; pyrrole NH).

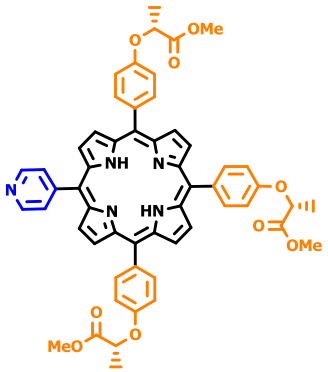

5,15-[4-(*R*)-Methyl-2-phenoxypropionate]-10,20-[4-pyridyl] porphyrin (*R,R*)-9 : M.F. : $C_{50}H_{40}N_6O_6$; **M.W. :** 820.66 g/mol ; **Found LDI-Tof [M^+] :** 823.4 ; **^{1}H-NMR** (360 MHz, *d*-Chloroform) δ 9.05 (s, 2H; pyridyl) 8.92 (d, *J* = 4.9 Hz, 4H; pyrrole CH), 8.80 (d, *J* = 4.8 Hz, 4H; pyrrole CH), 8.17 (s, 2H; pyridyl), 8.10 (d, *J* = 8.4 Hz, 4H; Pyridyl), 7.24 (s, 4H; ArH), 7.17 (dd, *J* = 7.8, 2.4 Hz, 4H; ArH), 5.09 (q, *J* = 6.8 Hz, 2H; O<u>CH</u>(CH_3)), 3.93 (s, 6H; $COOCH_3$), 1.84 (d, *J* = 6.7 Hz, 6H; OCH(<u>CH_3</u>)) -2.85 (s, 2H; pyrrole NH).

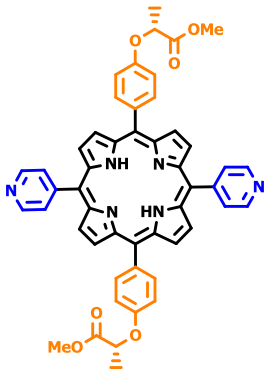

5,10-[4-(*R*)-Methyl-2-phenoxypropionate]-15,20-[4-pyridyl] porphyrin (*R*,*R*)-10 : M.F. : $C_{50}H_{31}N_6O_6$; **M.W. :** 820.66 g/mol ; **Found LDI-Tof [M^+] :** 823.4 ; **^{1}H-NMR** (360 MHz, *d*-Chloroform) δ 9.11-9.03 (m, 4H; pyridyl), 8.99-8.89 (m, 4H; pyrrole CH), 8.89-8.77 (m, 4H; pyrrole CH), 8.23-8.16 (m, 4H; pyridyl), 8.16-8.08 (m, 4H; ArH), 7.34-7.28 (m, 4H; ArH), 5.11 (q, *J* = 6.8 Hz, 2H; O<u>CH</u>(CH_3)), 3.95 (s, 6H; $COOCH_3$), 1.86 (d, *J* = 6.9 Hz, 6H; OCH(<u>CH_3</u>)), -2.81 (s, 2H; pyrrole NH).

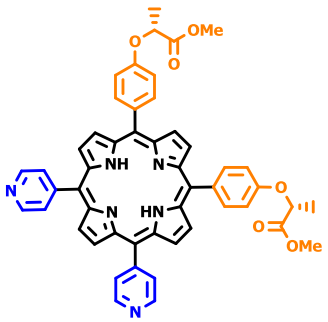

5-[4-(*R*)-Methyl-2-phenoxypropionate]-10,15,20-[4-pyridyl] porphyrin (*R*)-11 : M.F. : $C_{45}H_{33}N_7O_3$; **M.W. :** 719.56 g/mol ; **Found LDI-Tof [M^+] :** 723.7 ; **^{1}H-NMR** (360 MHz, *d*-Chloroform) δ 9.05 (d, *J* = 5.2 Hz, 6H; pyridyl), 8.97 (d, *J* = 4.7 Hz, 2H; pyrrole CH), 8.87 (s, 4H; pyrrole CH), 8.84 (d, *J* = 4.8 Hz, 2H; pyrrole CH), 8.17 (d, *J* = 5.2 Hz, 6H; pyridyl), 8.13 (d, *J* = 8.4 Hz, 2H; ArH), 7.29 (d, *J* = 8.4 Hz, 2H; ArH), 5.11 (q, *J* = 6.7 Hz, 1H; O<u>CH</u>(CH_3)), 3.95 (s, 3H; $COOCH_3$), 1.86 (d, *J* = 6.8 Hz, 3H; OCH(<u>CH_3</u>)), -2.84 (s, 2H; pyrrole NH).

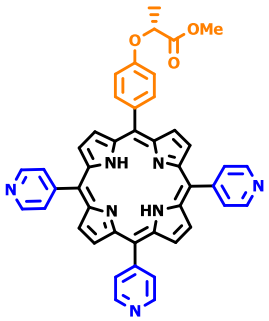

5,10,15,20-[4-pyridyl] porphyrin 12 : M.F. : $C_{40}H_{26}N_8$; **M.W. :** 618.45 g/mol ; **Found LDI-Tof [M^+] :** 621.4 ; **^{1}H-NMR** (250 MHz, *d*-Chloroform) δ 9.07 (d, *J* = 5.9 Hz, 8H; pyridyl), 8.87 (s, 8H; pyrrole CH), 8.16 (d, *J* = 5.9 Hz, 8H; pyridyl), -2.91 (s, 2H; pyrrole NH).[101]

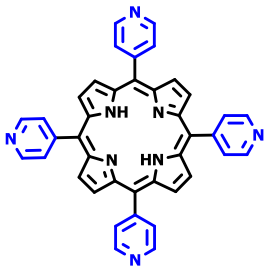

2.10.3. General procedure for the synthesis of free-base porphyrin derivatives 1-4.

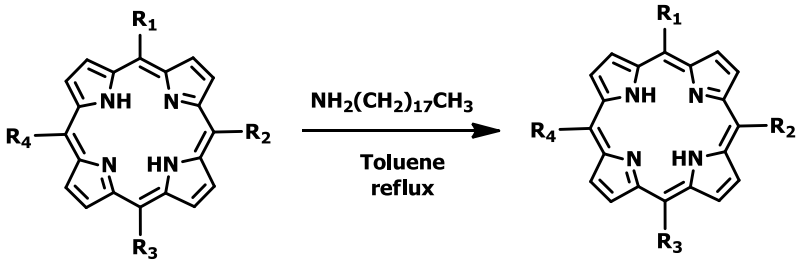

In separate reactions, each porphyrin (*R,R,R*)-**8**, (*R,R*)-**9**, (*R,R*)-**10**, (*R*)-**11** were dissolved in toluene under stirring and argon atmosphere. An excess of octadecylamine was added, and the resulting mixture was refluxed under inert atmosphere overnight. The mixture was cooled to give a dark red residue. The product was purified from the excess of octadecylamine by a short column silica gel chromatography (EtOAc) before a longer silica gel column chromatography (CH_2Cl_2/1% MeOH) was done and exclusion size chromatography (Bio-Beads) for the complete removal of free amine.

(101) Carlucci, L.; Ciani, G.; Proserpio, D. M.; Porta, F. *Angew. Chem.* **2003**, *115*, 331-336.

5,10,15-[4-(*R*)-2-*N*-octadecylamidoethyloxyphenyl]-20-[4-pyridyl] porphyrin (*R,R,R*)-1 : M.F. : $C_{106}H_{152}N_8O_6$; **M.W. :** 1632.01 g/mol ; **Found LDI-Tof [M^+] :** 1636.8 ; **^{1}H-NMR** (250 MHz, *d*-Chloroform) δ 9.12-9.01 (m, 4H; ArH), 8.98-8.89 (m, 4H; pyrrole CH), 8.89-8.75 (m, 4H; pyrrole CH), 8.20 (s, 4H; Pyridyl), 8.17 (d, *J* = 2.3 Hz, 4H; Pyridyl), 7.36 (d, *J* = 8.5 Hz, 4H; ArH), 6.76 (t, *J* = 6.0 Hz, 3H; CONH), 5.05 (q, *J* = 6.6 Hz, 3H; O<u>CH</u>(CH_3)), 3.59-3.33 (m, *J* = 6.6 Hz, 6H; CONH<u>CH_2</u>CH_2(CH_2)$_{15}$$CH_3$), 1.86 (d, *J* = 6.7 Hz, 9H; OCH(<u>CH_3</u>)), 1.74 (m, 6H; CONHCH$_2$<u>CH_2</u>(CH_2)$_{15}$$CH_3$), 1.51-1.10 (m, 90H; CONHCH$_2$CH$_2$(<u>CH_2</u>)$_{15}$$CH_3$), 0.91 (q, *J* = 6.9, 6.4 Hz, 9H; CONHCH$_2$CH$_2$(CH_2)$_{15}$<u>CH_3</u>), -2.77 (s, 2H; pyrrole NH) ; **IR-ATR** (cm^{-1}) : 3309 (m, NH), 2922 (s, CH_2), 2848 (s, CH_2), 1681 (m), 1651 (s, CONH), 1604 (m, Phenyl), 1593 (s, pyridyl), 1536 (m), 1502 (m, Phenyl), 1467 (m), 1229 (m), 1235 (s), 1175 (m), 1056 (m), 801 (m) ; **UV-Vis** (MCH) λ_{max}/nm (ε M^{-1} cm^{-1}) : 419 (497040), 515 (20180), 549 (10504), 593 (5186), 651 (3326).

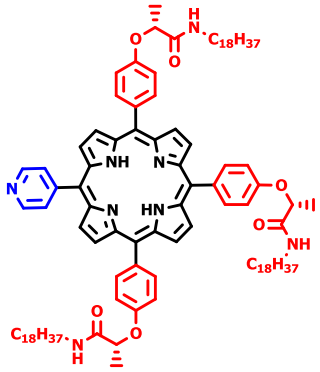

5,15-[4-(*R*)-2-*N*-octadecylamidoethyloxyphenyl]-10,20-[4-pyridyl] porphyrin (*R,R*)-2 : M.F. : $C_{84}H_{110}N_8O_4$; **M.W. :** 1294.16 g/mol ; **Found LDI-Tof [M^+] :** 1296.0 ; **^{1}H NMR** (360 MHz, *d*-Chloroform) δ 9.05 (d, *J* = 4.9 Hz, 4H; pyridyl), 8.87 (dd, *J* = 36.0, 4.8 Hz, 8H; pyrrole CH), 8.17 (m, 8H; 4H ArH, 4H pyridyl), 7.33 (d, *J* = 8.3 Hz, 4H; ArH), 6.73 (t, *J* = 5.9 Hz, 2H; CONH), 5.03 (q, *J* = 6.7 Hz, 2H; O<u>CH</u>(CH_3)), 3.43 (m, 4H; CONH<u>CH_2</u>CH_2(CH_2)$_{15}$$CH_3$), 1.83 (d, *J* = 6.7 Hz, 6H; OCH(<u>CH_3</u>)), 1.75-1.54 (m, 4H; CONHCH$_2$<u>CH_2</u>(CH_2)$_{15}$$CH_3$), 1.48-1.05 (m, 60H; CONHCH$_2$CH$_2$(<u>CH_2</u>)$_{15}$$CH_3$), 0.88 (q, *J* = 7.2, 5.3 Hz, 6H; CONHCH$_2$CH$_2$(CH_2)$_{15}$<u>CH_3</u>), -2.84 (s, 2H; pyrrole NH) ; **IR-ATR** (cm^{-1}) : 3320 (m, NH), 2918 (s, CH_2), 2851 (s, CH_2), 1655 (s, CONH), 1606 (m, Phenyl), 1591 (s, pyridyl), 1539 (m), 1502 (m, Phenyl), 1467 (m), 1229 (m), 1233 (s), 1077 (m), 797 (m) ; **UV-Vis** (MCH) λ_{max}/nm (ε M^{-1} cm^{-1}) : 420 (311040), 517 (13324), 551 (6154), 590 (4200), 647 (2642).

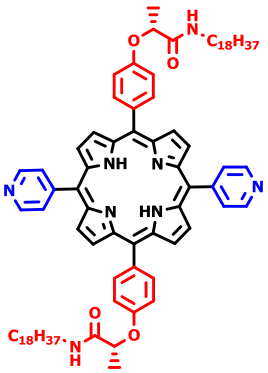

5,10-[4-(*R*)-2-*N*-octadecylamidoethyloxyphenyl]-15,20-[4-pyridyl] porphyrin (*R,R*)-3 : M.F. : $C_{84}H_{110}N_8O_4$; **M.W. :** 1294.16 g/mol ; **Found LDI-Tof [M^+] :** 1296.0 ; **^{1}H NMR** (250 MHz, *d*-Chloroform) δ 9.13-9.02 (m, 4H; pyridyl), 8.94 (d, *J* = 4.9 Hz, 2H; pyrrole CH), 8.92 (s, 2H; pyrrole CH), 8.87 (s, 2H; pyrrole CH), 8.83 (d, *J* = 4.9 Hz, 2H; pyrrole CH), 8.25-8.12 (m, 8H; 4H ArH, 4H pyridyl), 7.35 (d, *J* = 8.4 Hz, 4H; ArH), 6.74 (t, *J* = 5.9 Hz, 2H; CONH), 5.04 (q, *J* = 6.7 Hz, 2H; O<u>CH</u>(CH_3)), 3.47 (m, 4H; CONH<u>CH_2</u>$CH_2(CH_2)_{15}CH_3$), 1.85 (d, *J* = 6.7 Hz, 6H; OCH(<u>CH_3</u>)), 1.67 (m, 4H; CONHCH$_2$<u>CH_2</u>$(CH_2)_{15}CH_3$), 1.53-1.07 (m, 60H; CONHCH$_2$CH$_2$(<u>CH_2</u>)$_{15}CH_3$), 0.89 (t, *J* = 6.6 Hz, 6H; CONHCH$_2$CH$_2$(CH$_2$)$_{15}$<u>CH_3</u>), -2.79 (s, 2H; pyrrole NH) ; **IR-ATR** (cm^{-1}) : 3312 (m, NH), 2922 (s, CH_2), 2851 (s, CH_2), 1675 (s, CONH), 1660 (s, CONH), 1591 (s, pyridyl), 1504 (m, Phenyl), 1467 (m), 1229 (m), 1233 (s), 1177 (m), 1094 (m), 969 (m), 797 (m) ; **UV-Vis** (MCH) λ_{max}/nm (ε M^{-1} cm^{-1}) : 421 (622500), 516 (27580), 551 (12868), 590 (9114), 647 (5614).

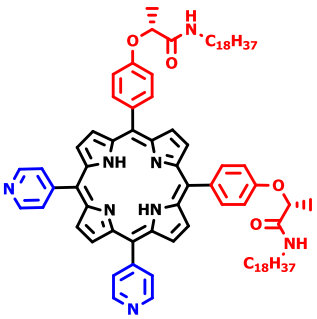

5-[4-(*R*)-2-*N*-octadecylamidoethyloxyphenyl]-10,15,20-[4-pyridyl] porphyrin (*R*)-4 : M.F. : $C_{62}H_{68}N_8O_2$; **M.W. :** 956.55 g/mol ; **Found LDI-Tof [M^+] :** 958.5 ; **^{1}H NMR** (250 MHz, *d*-Chloroform) δ 9.08 (d, *J* = 5.1 Hz, 6H; pyridyl), 8.96 (d, *J* = 4.8 Hz, 2H; pyrrole CH), 8.89 (s, 4H; pyrrole CH), 8.85 (d, *J* = 5.0 Hz, 2H; pyrrole CH), 8.19 (m, 8H; 6H pyridyl, 2H ArH), 7.36 (d, *J* = 8.4 Hz, 2H; ArH), 6.73 (t, *J* = 6.0 Hz, 1H; CONH), 5.04 (q, *J* = 6.7 Hz, 1H; O<u>CH</u>(CH_3)), 3.62-3.34 (m, 2H; CONH<u>CH_2</u>$CH_2(CH_2)_{15}CH_3$), 1.84 (d, *J* = 6.7 Hz, 3H; OCH(<u>CH_3</u>)), 1.68 (m, 2H; CONHCH$_2$<u>CH_2</u>$(CH_2)_{15}CH_3$), 1.52-1.02 (m, 30H; CONHCH$_2$CH$_2$(<u>CH_2</u>)$_{15}CH_3$), 0.89 (t, *J* = 6.6 Hz, 3H; CONHCH$_2$CH$_2$(CH$_2$)$_{15}$<u>CH_3</u>), -2.85 (s, 2H; pyrrole NH) ; **IR-ATR** (cm^{-1}) : 3316 (m, NH), 2918 (s, CH_2), 2848 (s, CH_2), 1658 (s, CONH), 1590 (s, pyridyl), 1538 (m), 1506 (m, Phenyl), 1467 (m),

1404 (m), 1229 (m), 1233 (s), 1175 (m), 1056 (m), 801 (m) ; **UV-Vis** ($CHCl_3$) λ_{max}/nm (ε M^{-1} cm^{-1}) : 417 (414900), 512 (20420), 545 (7868), 590 (6020), 647 (2532).

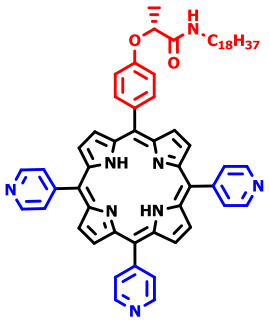

2.10.4. Synthesis of (*R*)-Methyl 2-(4-Formylphenoxy)-*N*-octadecylacetamide (*R*)-13.

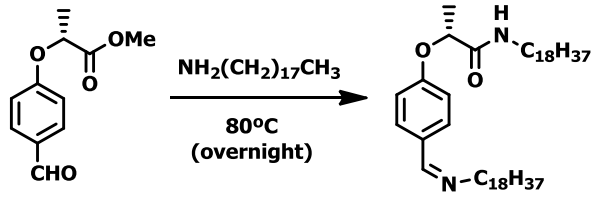

(*R*)-Methyl 2-(4-formylphenoxy)propanoate (*R*)-**6** (2.00 g, 9.60 mmol) was mixed with octadecylamine (5.16 g, 19.2 mmol) and the mixture heat to 80ºC overnight. The reaction mixture was dissolved in CH_2Cl_2/CH_3CN. The pale yellow solid was filtered to obtain 4.42 g (66.2%) of the pure compound. **M.F. :** $C_{45}H_{84}N_2O_2$; **M.W. :** 695.72 g/mol; **Found LDI-Tof [M^+] :** 697.9 ; **^{1}H NMR** (360 MHz, *d*-Chloroform) δ 8.21 (s, 1H; CHN), 7.68 (d, *J* = 8.5 Hz, 2H; ArH), 6.93 (d, *J* = 8.4 Hz, 2H; ArH), 6.34 (t, *J* = 6.2 Hz, 1H; CONH), 4.71 (q, *J* = 6.7 Hz, 1H; O<u>CH</u>(CH_3)), 3.58 (m, 2H; CHN<u>CH_2</u>$CH_2(CH_2)_{15}CH_3$), 3.25 (dq, *J* = 13.1, 6.6 Hz, 2H; NH<u>CH_2</u>$CH_2(CH_2)_{15}CH_3$), 1.69 (m, 2H; CHNCH$_2$<u>CH_2</u>$(CH_2)_{15}CH_3$), 1.60 (d, *J* = 6.7 Hz, 3H; OCH(<u>CH_3</u>)), 1.45 (m, 2H; NHCH$_2$<u>CH_2</u>$(CH_2)_{15}CH_3$), 1.27 (m, 60H ; 30H NHCH$_2$CH$_2$<u>$(CH_2)_{15}$</u>CH_3, 30H NHCH$_2$CH$_2$<u>$(CH_2)_{15}$</u>CH_3), 0.89 (t, *J* = 6.6 Hz, 6H; NHCH$_2$CH$_2$(CH$_2$)$_{15}$<u>CH_3</u>); **IR-ATR** (cm^{-1}) : 3671 (m), 3346 (m, NH), 2916 (s, CH_2), 2849 (s, CH_2), 1656 (s, CONH), 1605 (m, Phenyl), 1528 (s, CONH), 1500 (m, Phenyl), 1470 (m), 1231 (m), 1238 (s).

2.10.5. General procedure for the synthesis of free-bae porphyrin derivatives 1-4.

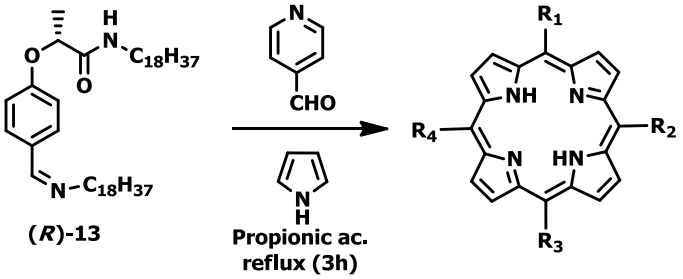

(*R*)-Methyl 2-(4-formylphenoxy)-*N*-octadecylacetamide (*R*)-**13** (2.65 g, 3.81 mmol) was dissolved in propionic acid (30 ml, 0.12 M), pyridine-4-aldehyde (0.36 ml, 3.81 mmol) was added, and the resulting mixture was refluxed with vigorous stirring for 30 minutes in air. Freshly filtered through neutral alumina pyrrole (0.26 ml, 3.81 mmol) was added drop by drop at 150ºC and then the mixture was allowed to reflux for about 3 hours. CH_2Cl_2 was added, and the organic phase was extracted with a saturate solution of Na_2CO_3 and was dried over anhydrous Na_2SO_4. Finally, the organic solvent was filtered through cotton wool and evaporated. The dark crude product was subjected to column chromatography on silica gel for purification (CH_2Cl_2/1.5% MeOH) and four different impure fractions were obtained. Each fraction was then purified by silica gel chromatography (CH_2Cl_2/1.5% MeOH) and bio-beads (toluene/CH_2Cl_2) to obtain (*R,R,R*)-**1** (68.1 mg, 1.1%), (*R,R*)-**2** (30.0 mg, 0.6%), (*R,R*)-**3** (92.6 mg, 1.9%), (*R*)-**4** (31.9 mg, 0.88%).

The characterization of the compounds was done as for the other route.

2.10.6. Synthesis of metalloporphyrin derivatives Zn-(1-4).

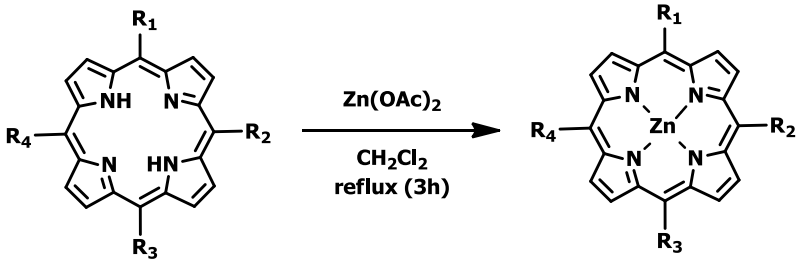

In separate reactions, each porphyrin (*R,R,R*)-**1** (40.0 mg, 0.024 mmol), (*R,R*)-**2** (14.0 mg, 0.011 mmol), (*R,R*)-**3** (30.0 mg, 0.023 mmol), (*R*)-**4** (20.6 mg, 0.022 mmol) were dissolved in CH_2Cl_2 ($7.5 \cdot 10^{-3}$ M) under stirring and argon atmosphere. Zinc acetate dissolved in 1:1 mixture of CH_2Cl_2/MeOH (0.052 M) was added drop wise with syringe over 5 minutes. The reaction mixture was refluxed further three hours. Dichloromethane was added and the organic layer was washed with a saturated aqueous solution of sodium bicarbonate, brine and was dried over anhydrous

Na_2SO_4 and concentrated *in vacuum*. The residue was purified by silica gel chromatography (CH_2Cl_2/1.5% MeOH) giving the desired metalloporphyrins as a purple metallic powder.

[5,10,15-[4-(*R*)-2-*N*-octadecylamidoethyloxyphenyl]-20-[4-pyridyl] porphyrin] zinc (II) Zn-(*R,R,R*)-1 : M.F. : $C_{106}H_{152}N_8O_6Zn$; **M.W. :** 1695.10 g/mol ; **Found LDI-Tof [M^+] :** 1697.9 ; **^{1}H NMR** (600 MHz (228K), *d*-Chloroform) δ 8.90 (d, *J* = 25.0 Hz, 4H; pyrrole CH), 8.56 (d, *J* = 15.5 Hz, 2H; pyrrole CH), 8.15 (ddd, *J* = 40.4, 29.7, 8.7 Hz, 4H; ArH), 7.94 (d, *J* = 16.2 Hz, 2H; ArH), 7.47 (s, 2H; pyrrole CH), 7.35 (s, 1H; ArH), 7.22 (d, *J* = 19.9 Hz, 5H; ArH), 6.97 (s, 2H; CONH), 6.78 (s, 1H; CONH), 6.32 (s, 1H; pyridyl), 6.07 (s, 1H; pyridyl), 5.04 (s, 2H; O<u>CH</u>(CH_3)), 4.96 (s, 1H; O<u>CH</u>(CH_3)), 3.62 – 3.27 (m, 6H; CONH<u>CH_2</u>$CH_2(CH_2)_{15}CH_3$), 2.58 (s, 1H; pyridyl), 1.97 (s, 1H; pyridyl), 1.88 (s, 6H; OCH(<u>CH_3</u>)), 1.77 (s, 3H; OCH(<u>CH_3</u>)), 1.61 (d, *J* = 54.4 Hz, 6H; CONHCH$_2$<u>CH_2</u>$(CH_2)_{15}CH_3$), 1.21 (m, 90H; CONHCH$_2$CH$_2$<u>$(CH_2)_{15}$</u>CH_3), 0.96 – 0.72 (m, 9H; CONHCH$_2$CH$_2$$(CH_2)_{15}$<u>$CH_3$</u>) ; **IR-ATR** ($cm^{-1}$) : 3297 (m, NH), 2922 (s, CH_2), 2851 (s, CH_2), 1725 (s, CONH), 1664 (s, CONH), 1606 (m, phenyl), 1521 (m), 1504 (m), 1460 (m), 1229 (m) ; **UV-Vis** ($CHCl_3$) λ_{max}/nm (ε M^{-1} cm^{-1}) : 422 (479840), 549 (19586), 588 (3846).

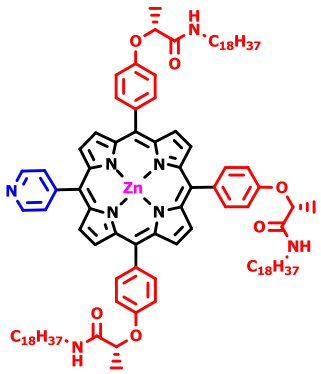

[5,15-[4-(*R*)-2-*N*-octadecylamidoethyloxyphenyl]-10,20-[4-pyridyl] porphyrin] zinc (II) Zn-(*R,R*)-2 : M.F. : $C_{84}H_{108}N_8O_4Zn$; **M.W. :** 1357.55 g/mol ; **Found LDI-Tof [M^+] :** 1358.0 ; **^{1}H NMR** (250 MHz, *d*-Chloroform) δ 8.89, 8.75, 8.08-8.05, 7.23 (pyrrole, pyridyl, phenyl), 6.76-6.73 (t, 1H; CONH), 5.01-4.84 (q, 2H; O<u>CH</u>(CH_3)), 3.45-3.38 (m, 4H; CONH<u>CH_2</u>$CH_2(CH_2)_{15}CH_3$), 1.80-1.77 (d, 6H; OCH(<u>CH_3</u>)), 1.36-1.33 (m, 4H; CONHCH$_2$<u>CH_2</u>$(CH_2)_{15}CH_3$), 1.26-1.13 (m, 60H; CONHCH$_2$CH$_2$<u>$(CH_2)_{15}$</u>CH_3), 0.88-0.81 (m, 6H; CONHCH$_2$CH$_2$$(CH_2)_{15}$<u>$CH_3$</u>) ; **IR-ATR** ($cm^{-1}$) : 3342 (m, NH), 2918 (s, CH_2), 2848 (s, CH_2), 1733 (s, CONH), 1669 (s, CONH), 1604 (m, phenyl), 1595 (pyridyl),1525 (m), 1504 (m), 1461 (m), 1229 (m), 1176 (m), 1072 (m), 994 (m), 793 (m) ; **UV-Vis** ($CHCl_3$) λ_{max}/nm (ε M^{-1} cm^{-1}) : 421 (249340), 548 (10016), 586 (1722).

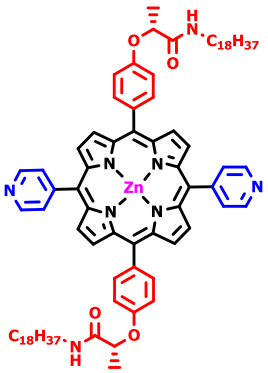

[5,10-[4-(*R*)-2-*N*-octadecylamidoethyloxyphenyl]-15,20-[4-pyridyl] porphyrin] zinc (II) Zn-(*R,R*)-3 : M.F. : $C_{84}H_{108}N_8O_4Zn$; **M.W. :** 1357.55 g/mol ; **Found LDI-Tof [M^+] :** 1358.9 ; **^{1}H NMR** (600 MHz (233K), *d*-Chloroform) δ 9.21-8.79 (m, pyrrole CH), 8.54 (d, pyrrole CH), 8.30-7.88 (m, ArH), 7.76 (pyrrole CH/ArH), 7.60 (pyrrole CH/ArH), 7.49 (ArH), 7.26 (ArH), 6.78 (CONH), 6.37 (pyridyl CH), 6.08 (pyridyl CH), 4.97 (m, 2H; OC<u>H</u>(CH_3)), 3.40 (m, CONH<u>CH_2</u>$CH_2(CH_2)_{15}CH_3$), 2.38 (pyridyl CH), 1.82 (OCH(<u>CH_3</u>)), 1.73-1.51 (CONHCH$_2$<u>CH_2</u>$(CH_2)_{15}CH_3$), 1.46-0.96 (CONHCH$_2$CH$_2$(<u>CH_2</u>)$_{15}CH_3$), 0.86 (CONHCH$_2$CH$_2$(CH$_2$)$_{15}$<u>CH_3</u>) ; **IR-ATR** (cm^{-1}) : 3316 (m, NH), 2918 (s, CH_2), 2855 (s, CH_2), 1733 (s, CONH), 1668 (s, CONH), 1606 (m, phenyl), 1593 (pyridyl), 1525 (m), 1502 (m), 1461 (m), 1231 (m), 1175 (m), 1072 (m), 994 (m), 793 (m) ; **UV-Vis** ($CHCl_3$) λ_{max}/nm (ε M^{-1} cm^{-1}) : 421 (384060), 548 (16350).

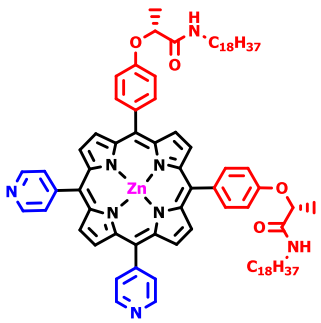

[5-[4-(*R*)-2-*N*-octadecylamidoethyloxyphenyl]-10,15,20-[4-pyridyl] porphyrin] zinc (II) Zn-(*R*)-4 : M.F. : $C_{62}H_{66}N_8O_2Zn$; **M.W. :** 1019.94 g/mol ; **Found LDI-Tof [M^+] :** 1019.6 ; **^{1}H NMR** (360 MHz, *d*-Chloroform) δ 8.82 (s, pyrrole CH), 8.28 (pyrrole CH/ArH), 8.04 (pyrrole CH/ArH), 6.77 (CONH), 4.97 (OC<u>H</u>(CH_3)), 3.52-3.27 (m, CONH<u>CH_2</u>$CH_2(CH_2)_{15}CH_3$), 2.33 (pyridyl CH), 1.79 (d OCH(<u>CH_3</u>)), 1.65 (CONHCH$_2$<u>CH_2</u>$(CH_2)_{15}CH_3$), 1.43-1.04 (m, CONHCH$_2$CH$_2$(<u>CH_2</u>)$_{15}CH_3$), 0.84 (CONHCH$_2$CH$_2$(CH$_2$)$_{15}$<u>CH_3</u>) ; **IR-ATR** (cm^{-1}) : 2922 (s, CH_2), 2851 (s, CH_2), 1738 (s, CONH), 1678 (s, CONH), 1595 (m, pyridyl), 1460 (m), 1229 (m), 994 (m) ; **UV-Vis** ($CHCl_3$) λ_{max}/nm (ε M^{-1} cm^{-1}) : 420 (327300), 548 (13856), 604 (3342).

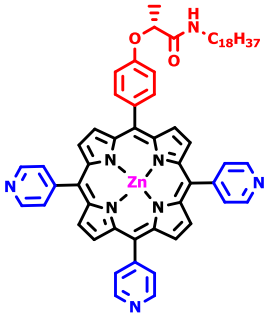
H
N
C18H37
O
O
N
N
N
N
Zn
N
N
N